國立臺灣大學理學院物理學系

碩士論文

Department of Physics

College of Science

National Taiwan University

Master Thesis

在緊湊渺子線圈實驗中尋找磁單極

Search for magnetic monopole at CMS Experiment

石琳

Lin Shih

指導教授: 陳凱風 教授

Advisor: Prof. Kai-Feng Chen

中華民國 111 年 11 月

November, 2022

doi:10.6342/NTU202300054

國立臺灣大學碩士學位論文
口試委員會審定書

在緊湊渺子線圈內尋找磁單極

Search for magnetic monopole at CMS experiment

本論文係石琳君（R09222007）在國立臺灣大學物理學所完成之碩士學位論文，於民國 111 年 11 月 8 日承下列考試委員審查通過及口試及格，特此證明

口試委員：陳凱風（簽名）

（指導教授）

張寶棣　　郭家銘

韋宇廷　　易聲祥

非田・辛 永心廷

doi:10.6342/NTU202300054

Acknowledgements

能夠參與台大高能實驗室並完成碩士學位，首先要感謝我的指導教授陳凱風，在一開始便讓我選擇在 CMS 實驗中尋找磁單極，讓我有機會參與這份工作，並提供我在學術研究上的指導，偶爾也和我吃飯聊天，成為亦師亦友的存在；也感謝 CMS 的磁單極小組一起推動這個題目的前進，以及謝謝呂榮祥教授、裴思達教授不吝嗇提供的協助。此外，也很感謝黃宇廷教授，讓我參與磁單極理論的書報討論，也提供我物理上許多充分的指導和協助，讓我對理論物理有更多理解和認識！

除了在 CMS 尋找磁單極以外，我在碩士最後半年也參與了氪氣與地震相關性的研究，這要感謝裴思達教授願意給我機會參與這個分析，對於地震科學也相當有興趣的我來說，能參與此分析是非常榮幸的事情，同時也非常感謝給我莫大幫助的學長 – 李侑穎 (大師)，帶領我著手整個分析、校正等工作，以及提供磁單極研究上的各種意見。雖然未能參與氪與地震的完整分析，但仍希冀此分析能夠為地震預測有所貢獻！

當然，高能實驗室的成員們也都是碩士生涯中重要的夥伴，高裕維、吳桐、陳奕安、林子路、蔡連勝、陳溥生、努比 (粟心輔)、李家豪、陳政綱、吳新業、Judy (陳柔安)、景澤、郭晉嘉、沈昀臻等人，不只是在研究上提供了許多幫助，還一起在 306 喝咖啡和茶，討論哲學、時事議題、薩爾達曠野之息、居合道、打球等，讓我的碩士生活多采多姿，有各種歡笑，還有在大學時期即認識，給予我許多研究生涯方向等的學長姐，Page (余佩容)、陳柏勳、林杰、陳孟呈、陳世軒等人。

最後感謝父母、朋友們，以及男友，在我無助時鼓勵我、安慰我、支持我，讓我能安心地從事研究、完成學業！

doi:10.6342/NTU202300054

doi:10.6342/NTU202300054

摘要

本論文分為兩部分：第一到八章為在 CMS 實驗中尋找磁單極，以及第九章之對地震與異常氡氣釋放的相關性研究。

第一部分：自從保羅狄拉克在一九三一年提出電荷量子化條件之後，尋找磁單極成為物理學家的重要課題之一。本論文描述在緊湊渺子線圈實驗內尋找磁單極，以證明狄拉克電荷量子化條件的理論。本研究使用了僅有磁單極信號的蒙地卡羅樣本模擬磁單極在緊湊渺子線圈實驗內的產生，並用從 2016 年至 2018 年間所收集之對撞質心能量為 13 兆電子伏特的質子-質子對撞事件中，尋找磁單極的訊號。本論文使用的模型為經德雷爾-顏過程產生之自旋 1/2 的磁單極對，並基於磁單極於模擬時出現的特徵做為分析策略。由於磁單極最低的磁荷 ($|g_D| = 1$) 相當於基本電荷量 e 的 68.5 倍，導致其與物質的交互作用非常強烈，因此磁單極被視為一種高度電離粒子。其中一個顯著的特徵即磁單極傾向飽和軌跡追蹤系統裡的矽條帶。另一特徵為磁單極在電磁量能器的少數幾個閃爍晶體中迅速製造出電磁射叢，導致其有如尖端一般的拓撲性質，最後因堆積大部分的能量而停留在電磁量能器中。本研究也提高了信號的效率並提供未來可投入使用的觸發器研究。最後，由於本實驗的信號靈敏度低，因此在 95% 的信心水準之下，可預期磁單極的質量大約為 2320 十億電子伏特。

第二部分：為防範大型地震對人類造成的危害，預測地震一直是地震學家關注的課題之一，其一理論認為放射性氣體-氡氣從地底異常大量之釋放可被視為大地震之前兆。本論文利用台大高能團隊開發出之晶體偵測器，放置在地震頻發的花蓮氣象站，至今已搜集兩年含有氡氣訊號之 γ-ray 光譜，並且從中央氣象局蒐集地震事件及地震波形，以研究大型地震與異常氡氣釋放事件的相關性。然而本論文蒐集之放射性光譜經各種校正嘗試及研究後，證實其受到當地氣溫影響而有失真現象，因此未能提供精準的相關性研究。

關鍵字：磁單極、高度電離粒子、緊湊緲子線圈、氡氣、地震

doi:10.6342/NTU202300054

doi:10.6342/NTU202300054

Abstract

This thesis consists of two parts, one is the search for magnetic monopole in CMS experiment from chapter 1 to 8, the other is sensing the earthquake from anomalous radon emission in chapter 9.

For the first part, since the charge quantization condition was proposed by Paul Dirac in 1931, the search for magnetic monopole comes to a vital topic for physicists. This thesis describes the search for magnetic monopole in the CMS Experiment, in order to prove the idea of the charge quantization condition. The study utilizes the signal MC sample to simulate the monopole production in the CMS experiment and search the signal events collected from the proton-proton collisions at a center-of-mass energy of 13 TeV from 2016 to 2018. The model used in this thesis is the spin-1/2 magnetic monopole pair from the Drell-Yan process. The analysis strategy is based on the monopole's signature in the simulation. Because the monopole is seen as a highly ionized particle where the lowest magnetic charge $|g_D| = 1$ corresponds to 68.5 times the elementary electric charge e, this would lead to a strong interaction with material strongly. Therefore, one significant characteristic is that monopoles tend to saturate the silicon strips in the Tracker. On the other hand, monopoles produce EM shower rapidly in a few ECAL crystals, causing a spike-like topological property, depositing most energy, and stopping in the ECAL eventually. This study also improves signal efficiency and provides the trigger study for future implementation. In the end, because of the low sensitivity to the signal, therefore, the limit on the mass is set to be 2320 GeV at 95% confidence level.

For the second part, to prevent human beings from disasters - big earthquakes, predicting

doi:10.6342/NTU202300054

earthquakes has been one significant issue for seismologists. One theory speculates that the anomalous radioactive radon emitting from the underground can be considered a precursor of big earthquakes. The NTUHEP developed a crystal detector, deployed in the Hualien weather station where earthquakes frequently happen, to collect the γ-ray spectrum that includes radon signal. Plus, the earthquake events and waveform data are also collected, in order to analyze the correlation between anomalous radon emission and earthquakes. However, after the calibration test and study, data quality is proved to be distorted, which is affected by the local temperature. Therefore, an accurate correlation study cannot be provided in the thesis.

Keywords: magnetic monopole, high ionized particle, CMS, radon, earthquake

doi:10.6342/NTU202300054

Contents

doi:10.6342/NTU202300054

doi:10.6342/NTU202300054

doi:10.6342/NTU202300054

doi:10.6342/NTU202300054

List of Figures

doi:10.6342/NTU202300054

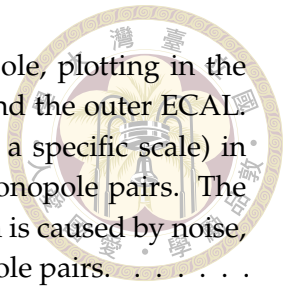

doi:10.6342/NTU202300054

doi:10.6342/NTU202300054

doi:10.6342/NTU202300054

List of Tables

doi:10.6342/NTU202300054

doi:10.6342/NTU202300054

Chapter 1 Introduction

The mysterious nature always attracts humans to excavate the fundamentals of physics. Under numerous physicists' efforts, the puzzle of human understanding of the fundamental particle has gradually been completed over the hundred years. Especially the discovery of the Higgs boson in 2012 makes the framework of fundamental particle physics "Standard Model (SM)" robust. The standard model makes humans discover the beauty of symmetry in the physics world. However, there still some enigma remains for humans to solve. One of them is the lack of magnetic monopole makes Maxwell's equation asymmetry. The first explanation for the existence of monopole is the charge quantization proposed by Paul Dirac in 1931. This chapter will introduce the standard model and review the progress of magnetic monopole theory and experiment briefly.

1.1 Standrad Model

The Standard Model (SM) [12] is a successful model to describe the fundamental particle and provides a precise explanation of three fundamental interaction forces (electromagnetic, weak, and strong). In quantum field theory, it is gauge symmetry under the transformation of the group theory $SU(3) \times SU(2)_L \times U(1)_Y$. The strong interaction, which describes the force between particles that carry the color charge, is gauge invariant under the transformation of $SU(3)$. The $SU(2)_L \times U(1)_Y$ describes the electroweak interaction, which unifies the electromagnetic interaction and weak interaction.

The fundamental particles are divided into two groups, the fermion, and the boson. The fermions are restricted by the Pauli exclusion principle and carry the half-integer spin, while the bosons carry the integer value of spin. In Standard Model, there are twelve kinds of fermions, including three generations of leptons (electron, tau, muon), three generations of neutrinos (electron neutrino, tau neutrino, muon neutrino), and three generations of quarks (up, down, charm, strange, top, bottom). The properties (mass, spin, charge number) of the fermions family are illustrated in figure 1.1. Among the three generations, only the first

doi:10.6342/NTU202300054

generation is the stable matter, other generations decay through weak interaction to the first generation.

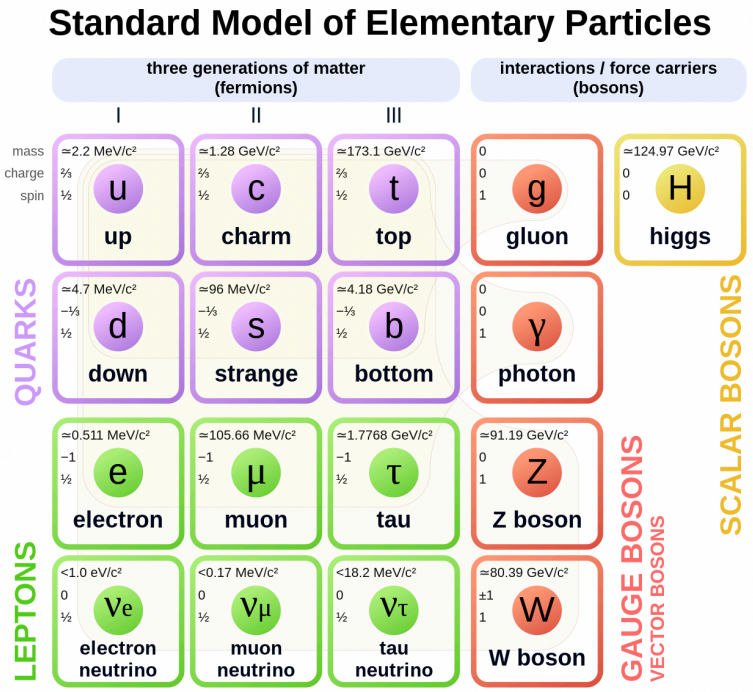

Figure 1.1: Illustration of all fundamental particles under the Standard Model.

On the other hand, the bosons in SM are the force carriers, where spin-1 vector bosons include photon, gluon, $\pm W$ and Zbosons, and spin-0 boson Higgs. According to quantum electrodynamics (QED), the photon as a propagator of electromagnetic interaction, couples to the charged particle such as leptons and quarks. The gluon, due to the description of quantum chromodynamics, involves the strong interaction which confines the color charged quarks in the hadron particle. The $\pm W$ bosons and Z bosons play roles in the weak interaction as well as the electroweak interaction on a higher energy scale. In weak interaction, only the left-hand antiparticle and right-hand particle couple to the propagator massive $\pm W$, and makes the unstable fermions that carry the weak isospin change their flavor into the stable particles. Nevertheless, under the gauge theory, it was also found that a neutral massive boson Z involves in weak interaction but couples to both left-hand and right-hand particles. The Z bosons cannot change the flavor of particles but change the spin, momentum, and energy of the particles. In the GSW model, the weak hypercharge (Y) linearly combines the electromagnetic charge (Q) and weak isospin I_W to predict the relationship between the electromagnetic interaction under $U(1)$ symmetry and the weak interaction under $SU(2)_L$ symmetry. In short, the electroweak model is able to provide a consistent picture of the unification of electromagnetic interaction and weak interaction.

In principle, the gauge symmetry in particle physics results in the massless particle.

doi:10.6342/NTU202300054

However, the massive $\pm W$ and Z bosons break the gauge symmetry in the weak interaction. In 1964, Peter Higgs and five other physicists proposed the Higgs Mechanism, where the concept of spontaneous symmetry breaking interprets the origin of mass and predicts the existence of the scalar boson. For long, physicists believed the Higgs boson was the last puzzle of the complete Standard Model. In 2012, the discovery of the Higgs boson in CMS and ATLAS experiment at CERN, giving around 125 GeV of mass, announced that the last key in the Standard model was found.

1.1.1 Beyond the Standard Model

Although Standard Model provides a basic framework for particle physics, it is still not a complete theory. Numerous theories and experiments called beyond the Standard Model (BSM) attempt to answer unanswered questions, such as dark matter, neutrino mass, matter-antimatter asymmetry, the existence of the magnetic monopole, and so on. Furthermore, the coupling constant of the three forces in SM has similar strengths, which has been shown that at some high-energy scales, the coupling constant tends to be brought together. This implies that the unification of the forces is plausible. Two well-known theory trying to explain the unification of forces has been proposed.

One of them is the Grand Unified Theories (GUT), which is suggested by Georgi and Glashow, showing that the gauge symmetry of the Standard model can be unified in the SU(5) symmetry group or higher dimension gauge symmetry SO(10), and the coupling constant of SM converge at the energy scale of about 10^{15} GeV. It is noteworthy that GUT predicts the existence of magnetic monopole, which will be discussed in the next section.

The other popular theory is supersymmetry (SUSY), which is the extension of SM by adding another type of symmetry in the Lagrangian. It is suggested that the fermionic particles can be exchanged with the bosonic particles under the symmetries. SUSY also predicts the existence of "sparticle" which are the super-partner of particles in the SM. The supersymmetric particles modify the unification of the U(1), SU(2), and SU(3), where three symmetries will converge to one point at some energy scale. SUSY also solves the Hierarchy problem in a natural way. Nevertheless, there is no experimental evidence for SUSY so far, it is expected that more evidence for SUSY will be provided in the future experiment.

doi:10.6342/NTU202300054

1.2 Magnetic Monopole

Since the understanding of electromagnetism had improved in the nineteenth century, people recognized that the magnetic field was created by the electric current, rather than the fluid of the magnetic monopole pole. The well-known Maxwell's equation has been built to explain electromagnetic interaction.

$$\nabla \cdot \mathbf{E} = \frac{\rho_e}{\epsilon_0} \qquad \nabla \cdot \mathbf{B} = 0 \tag{1.1}$$

$$\nabla \times \mathbf{E} = -\frac{\partial \mathbf{B}}{\partial t} \qquad \nabla \times \mathbf{B} = \frac{1}{c^2}\frac{\partial \mathbf{E}}{\partial t} + \mu_0 \mathbf{j}_e \tag{1.2}$$

where E and B represent electric field and magnetic field respectively, ϵ_0 is permittivity of free space, μ_0 is permeability of free space, the speed of light c equals to $1/\sqrt{\epsilon_0 \mu_0}$, and ρ_e and j_e represent electric charge density and electric current respectively.

As the Gauss' law in Maxwell's equation 1.1 shows that the divergence of the electric field results from the distribution of electric charge density, while the divergence of the magnetic field is always zero, which means that the magnetic charge does not exist.

Nevertheless, it is attractive for humans to construct the existence of magnetic charge, or magnetic monopole as an elementary particle, just like the electric charge and electrically charged particle. The first proposal of the existence of a magnetic monopole constructed by means of quantum theory came out in 1931 by physicists Paul Dirac [13]. His **quantization condition** gives a significant conclusion: if any magnetic charge exists, then the electric charge must be quantized. It is known that the electric charge is quantized certainly, meaning that the magnetic charge (magnetic monopole) must exist. Although no experiment observe the existence of monopoles so far, the "quantization condition" gives humans reasons to value the existence of magnetic monopoles. This section will overview some significant theories for the magnetic monopole and review the previous searches for magnetic monopole experiments.

1.2.1 Magnetic monopole in electromagnetism

Maxwell's equation as equation 1.1 and 1.2 explains the relation of electric field and magnetic field associated with the motion of electric charge. However, it is asymmetry due to the lack of magnetic charge density ρ_m and magnetic current density $\mathbf{j}_m$. It is theoretical available to add magnetic charge and current analogously to the electric charge and current

doi:10.6342/NTU202300054

to make Maxwell's equation symmetry:

$$\nabla \cdot \mathbf{E} = \frac{\rho_e}{\epsilon_0} \qquad \nabla \cdot \mathbf{B} = \mu_0 \rho_m \tag{1.3}$$

$$\nabla \times \mathbf{E} = -\frac{\partial \mathbf{B}}{\partial t} - \mu_0 \mathbf{j}_m \qquad \nabla \times \mathbf{B} = \frac{1}{c^2}\frac{\partial \mathbf{E}}{\partial t} + \mu_0 \mathbf{j}_e \tag{1.4}$$

Note that the magnetic charge density ρ_m is arose from the integrated of magnetic monopole, g, with the relation of $\rho_m = g\delta(\mathbf{r})$. The modified Maxwell's equation with magnetic monopole can be transformed into the original form by duality transformation:

$$\begin{pmatrix} \mathbf{E} \\ c\mathbf{B} \end{pmatrix} = \begin{pmatrix} cos\xi & sin\xi \\ -sin\xi & cos\xi \end{pmatrix} \begin{pmatrix} \mathbf{E}' \\ c\mathbf{B}' \end{pmatrix} \qquad \begin{pmatrix} c\rho_e \\ \rho_m \end{pmatrix} = \begin{pmatrix} cos\xi & sin\xi \\ -sin\xi & cos\xi \end{pmatrix} \begin{pmatrix} c\rho'_e \\ \rho'_m \end{pmatrix} \tag{1.5}$$

where the ξ is the transformation parameter. The duality transformation shows that electric charge density and current are symmetric with magnetic charge density and current under the transformation. This raises the question of whether it makes sense to define the electric and magnetic charges individually. If any magnetic monopole is observed in nature, the symmetry of Maxwell's equation would be brought back, causing the fields transform from $\mathbf{E}$ to $\mathbf{B}$, $\mathbf{B}$ to $-\mathbf{E}$, and their sources from $c\rho_e$ to ρ_m, and ρ_m to $-c\rho_e$ for $\xi = \pi/2$. The original Maxwell's equation without magnetic charge can be shown if the ξ is defined as 0 arbitrary.

1.2.2 Dirac Monopole in Quantum Theory

As mentioned at the beginning of the section, Dirac proposed the concept of "quantization condition" in 1931, which pointed out that the condition of the electric charge quantization is that the magnetic monopole must exist. About two decades later, Dirac put his efforts to establish the theory of magnetic monopole [14], giving the famous theory of **Dirac string**. The detail to construct monopole in quantum theory following with Dirac's idea is summarized below.

- **Gauge transformation**

  It is well-known that electromagnetism is invariant under the gauge transformation [15], which means that the equation 1.6 does not change by the transformation form 1.7.

doi:10.6342/NTU202300054

$$\mathbf{E} = -\nabla\phi - \frac{1}{c}\frac{\partial \mathbf{A}}{\partial t} \qquad \mathbf{B} = \nabla \times \mathbf{A} \tag{1.6}$$

$$\mathbf{A}' = \mathbf{A} + \nabla\Lambda, \qquad \phi' = \phi - \frac{\partial \Lambda}{\partial t} \tag{1.7}$$

The vector potential **A** in 1.7 does not correspond to any physical observable, the choice of **A** is always arbitrary and does not influence the physical quantities **E** and **B**. Take an example in classical electromagnetism, consider a charged particle in a uniform magnetic field in the z-direction

$$\mathbf{B} = B\hat{\mathbf{z}} \tag{1.8}$$

where the magnetic field must satisfy the equation 1.6. Because the physical observables such as the trajectory of the charged particle are not affected by the gauge used. It is available to derive magnetic field from

$$A_x = \frac{-By}{2}, \qquad A_y = \frac{Bx}{2}, \qquad A_x = 0 \tag{1.9}$$

or also from

$$A_x = -B_u, \qquad A_y = 0, \qquad A_x = 0 \tag{1.10}$$

It is straightforward to see that first vector potential can be transformed into the second vector potential by using equation 1.7 and choosing $\Lambda = \frac{xy}{2}B$,

$$\begin{pmatrix} -\frac{By}{2} \\ \frac{Bx}{2} \\ 0 \end{pmatrix} = \begin{pmatrix} -By \\ 0 \\ 0 \end{pmatrix} + \begin{pmatrix} \partial_x(\frac{xy}{2}B) \\ \partial_y(\frac{xy}{2}B) \\ \partial_z(\frac{xy}{2}B) \end{pmatrix} \tag{1.11}$$

Thus, it is clear that the arbitrary vector potential **A** does not affect the physical observable such as the magnetic field or the trajectory of the charged particle.

- **Quantum Mechanics**

  In quantum mechanics, the Hamiltonian for charged particle e in an electromagnetic field can be derived as:

$$H = \frac{1}{2m}(\mathbf{p} - \frac{e\mathbf{A}}{c})^2 + e\phi \tag{1.12}$$

where **p** is canonical momentum, which is not gauge invariant. Instead, the real physical observable is kinematical momentum, which is also gauge invariant, denoted

doi:10.6342/NTU202300054

by Π:

$$\Pi \equiv m\frac{d\mathbf{x}}{dt} = \mathbf{p} - \frac{e\mathbf{A}}{c} \tag{1.13}$$

In addition, a wave function $\psi(x,t) = \langle x|\alpha\rangle$ in the electromagnetic background transforms under the gauge transformation, that is, $|\alpha\rangle$ becomes $|\alpha'\rangle$ under gauge transformation by setting an operator Ω;

$$\Omega = \exp(\frac{ie\Lambda}{\hbar c}) \tag{1.14}$$

which the invariance is also guaranteed if

$$\Omega^\dagger \mathbf{x}\Omega = \mathbf{x}, \qquad \Omega^\dagger(\mathbf{p} - \frac{e\mathbf{A}}{c} - \frac{e\nabla\Lambda}{c})\Omega = \mathbf{p} - \frac{e\mathbf{A}}{c}. \tag{1.15}$$

Thus, the wave function ψ can be transformed into $\exp(\frac{ie\Lambda}{\hbar c})\psi$.

- **Magnetic monopole and Dirac String**

  We have shown how gauge transformation works in classical electromagnetism, in which magnetic monopole is not considered in the Maxwell equation. Although quantum mechanics does not predict the existence of the magnetic monopole, it is feasible to assume a magnetic monopole with magnetic charge g, located at the origin, analogous to electric charge in Gaussian units:

$$\mathbf{B} = \frac{g}{r^2}\hat{r}, \tag{1.16}$$

such that,

$$\oint \mathbf{B}\cdot d\mathbf{a} \neq 0 \tag{1.17}$$

Moreover, it is assumed that $\mathbf{B} = \nabla\times\mathbf{A}$ holds true everywhere, then

$$\oint \mathbf{B}\cdot d\mathbf{a} = \int d\mathbf{a}\cdot(\nabla\times\mathbf{A}) = \int dV\nabla\cdot(\nabla\times\mathbf{A}) \neq 0 \tag{1.18}$$

Nevertheless, the $\nabla\cdot(\nabla\times\mathbf{A})$ becomes non-zero as contradicted with the mathematical definition, namely $\nabla\cdot(\nabla\times\mathbf{A})$ must be zero. This contradiction implies that vector potential $\mathbf{A}$ is not well-defined everywhere. A pair of solution of vector potential $\mathbf{A}$ is given by

$$\mathbf{A}_1 = \frac{g(1-\cos\theta)}{r\sin\theta}\hat{\phi}, \quad \theta < \pi - \epsilon \tag{1.19}$$

$$\mathbf{A}_2 = -\frac{g(1+\cos\theta)}{r\sin\theta}\hat{\phi}, \quad \theta > \epsilon \tag{1.20}$$

Both vector potentials $\mathbf{A}_1$ and $\mathbf{A}_2$ are ill-defined as $\epsilon \to 0$, that is $\theta \to \pi$ and $\theta \to 0$ respectively. This set of vector potential within singularity is known as **Dirac String**.

doi:10.6342/NTU202300054

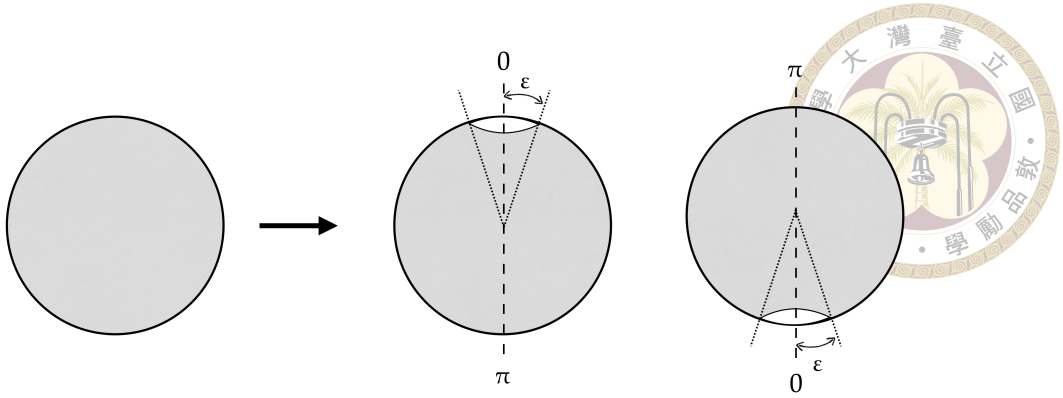

Figure 1.2: Illustration of the validity region of the vector potential. The figure in the left shows the vector potential **A** without the assumption of magnetic charge is acceptable everywhere, while either $\mathbf{A}_1$ or $\mathbf{A}_2$ is valid everywhere except a cone along north pole ($\theta < \epsilon$) in the middle figure or south pole ($\theta > \pi - \epsilon$) in the right figure respectively.

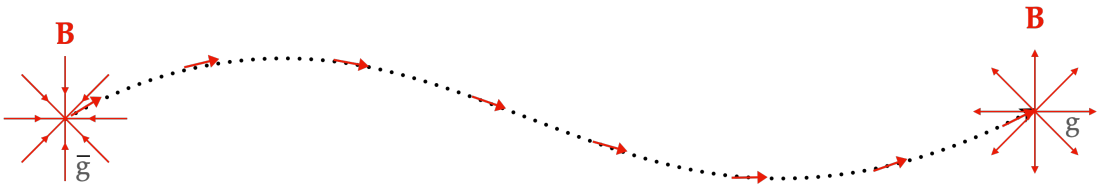

Figure 1.3: Figure of an imagined Dirac string. One pole (singularity) extends to the other at infinity.

The Dirac string can be imagined as any curved line (see figure 1.3), extending from one pole to the other at infinity and carrying an opposite charge, that is, every singularity must be at the end of the string. Besides, this theory does not give physical properties such as mass and spin, so monopole could be either fermion-like or boson-like.

- **Charge Quantization Condition**

  Regardless of the different regions where two vector potentials cover, both vector potentials must be able to gauge transform into each other because they lead to the same physical consequence, magnetic field, i.e.,

$$\mathbf{A}' - \mathbf{A} = \nabla\Lambda = \frac{2g}{r\sin\theta}\hat{\phi} = \frac{1}{r\sin\theta}\frac{\partial\Lambda}{\partial\phi}\hat{\phi} \tag{1.21}$$

  and thus getting the parameter of gauge transformation Λ,

$$\Lambda = 2g\phi \tag{1.22}$$

  Now, consider a wave function of an electric charge particle e subjected to an electromagnetic field, transforms in a particular gauge choosing as shown in equation 1.14,

$$\psi' = \psi\exp(\frac{i2eg\phi}{\hbar c}) \tag{1.23}$$

doi:10.6342/NTU202300054

where ϕ covers the range from 0 to 2π . If one chooses a definite location of θ and a constant radius r, touring the azimuthal from $\phi = 0$ to $\phi = 2\pi$, the wave function either ψ or ψ' must return to the original value despite of experiencing a phase change. This explains what electric charges experience in the Dirac string, electric charges could detect the string when it goes around the string from $\phi = 0$ to $\phi = 2\pi$, but only when multiple of $\phi = 2\pi$ makes the $\psi' = \psi$ exactly, so that the string is undetectable and realize the real monopole. In other words, a real monopole comes out only if

$$\frac{2eg}{\hbar c} = N, \quad N = 0, \pm 1, \pm 2, ... \tag{1.24}$$

The requirement brings out the charge quantization condition, which indicates that the electric charge (e) is quantized when there exists any magnetic charge (g). In nature, the electric charge is observed to be quantized as in units of electron electric charge, (e), while no magnetic charge g is detected so far. One can rewrite the relation of electric charge and magnetic charge in terms of the fine structure constant $\alpha = \frac{e^2}{\hbar c}$, and select N = 1 for a magnetic charge in the lowest case, known as Dirac charge g_D:

$$g = \frac{e}{2\alpha}N \xrightarrow{N=1} g_D = \frac{e}{2\alpha} \xrightarrow{\alpha=\frac{1}{137}} g_D = 68.5e \tag{1.25}$$

With the fine structure constant being $\frac{1}{137}$, therefore, the smallest magnetic charge g_D is 68.5 times elementary electric charge e.

1.2.3 Magnetic monopole coupling to the photon

The strength of coupling between monopole and photon plays a vital role when monopole comes to the other material in the electromagnetic interaction. The coupling between electron and photon is given by the fine structure constant α. Analogously, it is available to substitute the electric charge e with $g = Ng_D = N\frac{e^2/(2\alpha)^2}{\hbar c}$ and set $N = 1$ to obtain coupling between monopole and photon, α_M, as shown in figure 1.4.

$$\alpha = \frac{e^2}{\hbar c} \xrightarrow{e \to g_D = \frac{e^2/(2\alpha)^2}{\hbar c}} \alpha_M = \frac{e^2}{4\alpha^2 \hbar c} \tag{1.26}$$

The equation above shows directly that the coupling strength between monopole with $N = 1$and the photon is $(137/2)^2$ (at least four orders) times stronger than the electron and photon. Such a strong coupling value provides a significant understanding of the production of monopoles and the interaction between monopoles and matters.

doi:10.6342/NTU202300054

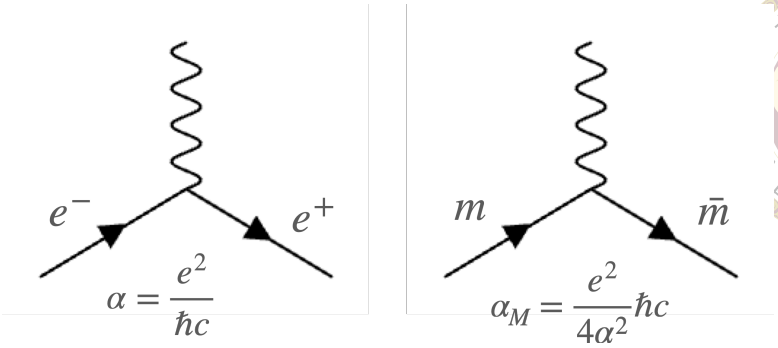

Figure 1.4

1.2.4 Monopole in Grand Unified Theory

Unlike Dirac's monopole, several Grand Unified Theories (GUT) predict the presence of magnetic monopole. Depending on the different grand unification scale M_x, varying ranges of monopole mass are predicted. Take a strong assumption for example, under the "desert hypothesis", where no new interaction or new particle was assumed under the present energy scale (of order 100 GeV), the prediction M_x is of order 10^{14} GeV. This brings about the properties of monopole with charge $g = g_D = 1/2e$ and mass 10^{16} GeV [16]. Although the desert hypothesis might be wrong, the monopole is expected to be an extremely stable heavy elementary particle. However, such a high energy scale is beyond the capable range of search for monopoles in the Large Hadron Collider nowadays.

1.2.5 Electroweak monopole

Although the SM does not predict the existence of monopole, some theories claim that the final test of the SM is the electroweak monopole [17] because the monopole mass is predicted to be of order 4-10 TeV with charge $2g_D$. Therefore, such a low mass scale gives the motivation to search for the monopole in the hadron collider.

1.3 Passage of Monopoles through Matter

Magnetic monopoles interact in the electromagnetic field can be described by the Lorentz force which carrying both magnetic charge g and electric charge q

$$\mathbf{F} = q(\mathbf{E} + \mathbf{v} \times \mathbf{B}) + g(\mathbf{B} - \mathbf{v} \times \frac{\mathbf{E}}{c^2}) \tag{1.27}$$

It is demonstrated in equation 1.25 that the lowest magnetic charge g_D equals $68.5e$.

doi:10.6342/NTU202300054

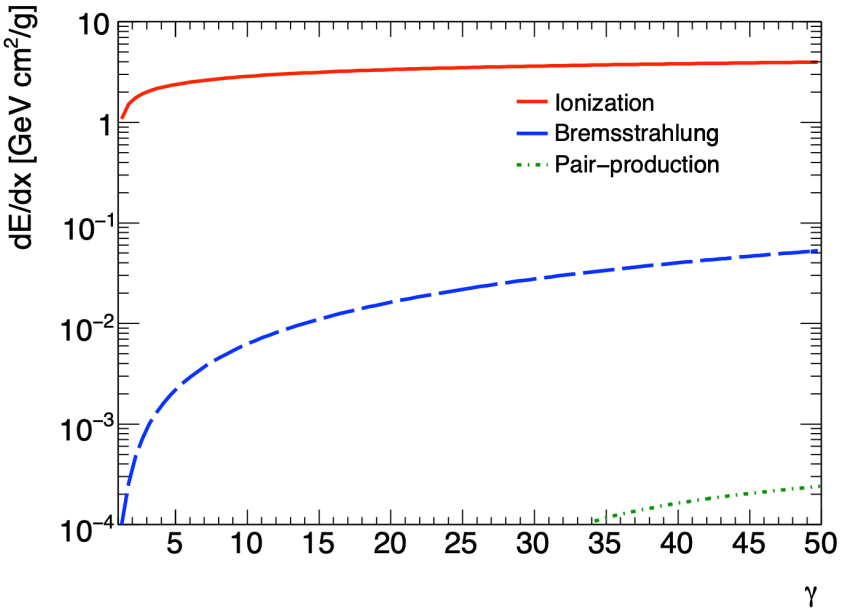

Figure 1.5: The comparison of different process of energy loss dE/dx for magnetic monopole of charge $|g| = 1.0g_D$ and mass 1000 GeV in argon. In the range $\gamma < 10$, which corresponds to the scenarios for production at the Large Hadron Collider, the dominant contribution to energy loss is ionization [1].

Therefore, the force between the magnetic monopole and the electric field is at least one order times stronger than that of an electrically charged particle. Furthermore, the strength of magnetically charged particle coupling to the electromagnetic interaction, which propagates the force by photon, is several thousand times that of the electrically charged particle.

In particle collider physics, the energy loss process for the charged particle can be ionization, bremsstrahlung, and pair production. Bremsstrahlung is a process in which a charged particle travels through the medium, the particle may be decelerated by the nuclei and radiates, leading to energy loss. The radiated photon may then produce a series of electron-positron pairs when encountering the nucleus, known as pair production.

In addition, when the charged particle carries sufficient energy to ionize the atom where the electron is completely separated from the atom and takes away the energy of the charged particle, such a process is called ionization. However, for a monopole mass in a TeV scale and charge $|g| = g_D$, the contribution of energy loss by bremsstrahlung and pair production can be neglected in the range $\gamma < 10$, as shown in graph 1.5. Consequently, the dominant process of energy loss in the medium for monopole is ionization.

doi:10.6342/NTU202300054

symbol	parameter
Z	atomic number
A	atomic mass
I	mean excitation energy of the medium
K	0.307 MeV $g^{-1}cm^2$
m_e	electron mass
γ	$1/\sqrt{1-\beta^2}$
c	speed of light

Table 1.1

1.3.1 Energy loss by Ionization

To begin with, the energy loss of an electrically charged particle $q_e = ze$ travels through a certain material with a velocity $\beta = v/c$ is modeled by the Bethe formula [18]:

$$-\frac{dE}{dx} = K\frac{Z}{A}\frac{z^2}{\beta^2}\left[\ln\frac{2m_e c^2\beta^2\gamma^2}{I} - \beta^2\right] \tag{1.28}$$

where each symbol is listed in table 1.1. For a highly electrically charged particle ($|z| = 68.5$), the relation of the energy loss dE/dx and its velocity is illustrated on the left of the figure 1.6. The lower velocity is a highly electrically charged particle in a certain material, the higher the energy deposit in the material, i.e., the larger the energy loss for the highly electrically charged particle. As mentioned previously, monopole ionizes a large amount of energy due to its strong strength coupling to the electromagnetic field. Subsequently, a substitute of $ze = \beta g$ and slight modification can be done to acquire the energy loss of monopole transversing in materials:

$$-\frac{dE}{dx} = K\frac{Z}{A}g^2\left[\ln\frac{2m_e c^2\beta^2\gamma^2}{I_m} + \frac{K(|g|)}{2} - \frac{1}{2} - B(|g|)\right] \tag{1.29}$$

where the parameter $K|g|$ and $B|g|$ are the corrections from the Kazama, Uang, and Goldhaber cross section correction and the Bloch correction, given by

$$K(|g|) = \begin{cases} 0.406 & |g| = g_D \\ 0.346 & |g| = 2g_D \end{cases} \tag{1.30}$$

doi:10.6342/NTU202300054

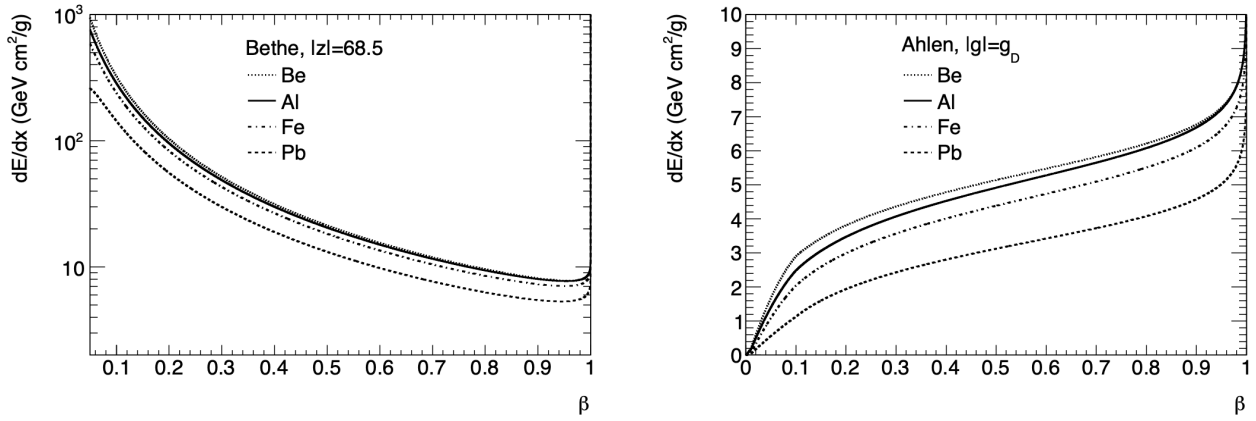

Figure 1.6: Ionization energy loss dE/dx in various materials as a function of velocity β for HIPs carrying electric charge $|z| = 68.5$ in the left (calculated by equation 1.28) and magnetic charge $|g| = g_D$ in the right (calculated by equation1.29.)

$$B(|g|) = \begin{cases} 0.248 & |g| = g_D \\ 0.672 & |g| = 2g_D \\ 1.022 & |g| = 3g_D \\ 1.685 & |g| = 6g_D \end{cases} \tag{1.31}$$

The modified Bethe equation only valid at $\beta \sim 0.1$. For very low velocity, $\beta \leq 0.01$, the energy loss of monopoles dE/dx is approximated to 45 (GeV/cm)$(g/g_D)^2\beta$ for all materials.

The trend of energy loss with different velocity β for a magnetic charge $|g| = g_D$ is presented in the right hand side of the figure 1.6. The energy loss of a magnetically charged particle shows a tendency to increase as the particle has a higher velocity, which is opposite to the trend of the electrically charged particle. When an electrically charged particle with charge $|z| = 68.5$ and a magnetically charged particle with charge $|g| = g_D$ have high velocity $\beta \sim 1$, their energy loss comes to around 10 GeV cm^2/g by coincidence. The critical difference is the behavior in the low velocity. The electrically charged particle is expected to release large energy with decreasing β, depositing a large fraction of energy near its trajectory. In contrast, the energy loss of the magnetically charged particle diminishes with decreasing β.

Furthermore, because of the high coupling of monopoles with materials, monopoles are categorized as highly ionizing particles (HIPs) which are characteristic of high ionized energy at least dozen times greater than the minimum ionizing particles. Such property makes the monopole have a significant signature signal in the CMS detector, which will be described in Chapter 3.

doi:10.6342/NTU202300054

doi:10.6342/NTU202300054

Chapter 2 LHC and CMS experiment

2.1 Large Hadron Collider(LHC)

To uncover the mysterious physics of the inner atom and discover new physics, people have built lots of accelerators to elevate the energy of particles to make particles carry enough energy to split. Along with improving the theory of particle physics and the technology of building particle accelerators, higher central-of-mass energy, higher luminosity, and more stable particle beams are needed.

The Large Hadron Collider (LHC) [19] is the largest and most powerful particle accelerator ever built in the world. It was built by European Organization for Nuclear Research (CERN) from 1998 to 2008. The overall length of the accelerator's ring is about 27 kilometers and as deep as 175 meters beneath the France–Switzerland border near Geneva. After upgrading the LHC in 2015, the central-of-mass energy of the proton-proton collision is as high as 13 TeV, and higher luminosity is achieved. It aims to improve the theory of the Standard Model (SM) and search for new physics beyond the Standard Model, such as the topic of this thesis, searching for the magnetic monopole.

2.1.1 LHC Machine Design and the Injector Chain

The Large Hadron Collider [19] is a two-ring accelerator, which is mainly composed of beam pipes, superconducting dipole electromagnets, and superconducting quadrupole electromagnets, and radiofrequency cavities (RF cavity). Each beam pipe is kept at a vacuum pressure of $10^{-07}Pa$ to avoid any air molecular colliding with the proton beams. In order to make the proton beams circulate stably in the rings, 1232 dipole electromagnets give a strong magnetic field of 8.3 TeV from superconducting coils (cooled down to 1.9 K by superfluid helium) with 11080 amperes, to drive the bending in the ring of LHC. On the other hand, a large number of protons in the beams could repel each other because of the Coulomb force, making the beams dispersive and lowering the rate of collisions. Thus, 392 quadripole

doi:10.6342/NTU202300054

electromagnets focus the beams in the transverse direction either vertically or horizontally to control the size of crossing bunches and raise the higher luminosity. Ahead of the collision points, the quadrupole squeezes the beam size to make two opposite beams colliding in precise positions.

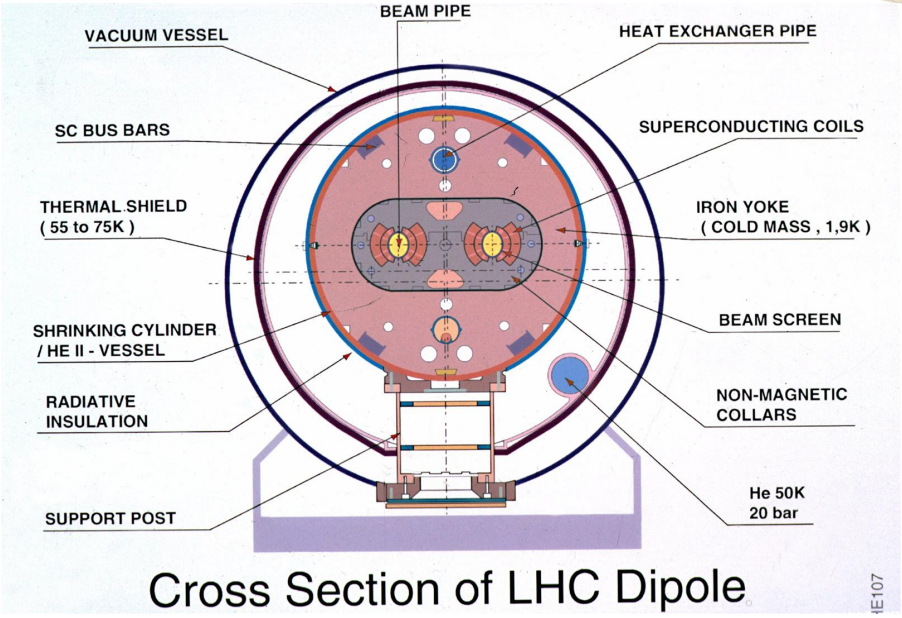

Figure 2.1: Scheme of 15 m long LHC cryodipole.

The LHC is not the only accelerator to boost the energy of protons. The beam of protons is accelerated increasingly by a succession of accelerators before it injects into the LHC. Firstly, the negative hydrogen ions (H-, hydrogen with an additional electron) come from a bottle of hydrogen gas at one end of Linear accelerator 2 (Linac2). The Linac2 uses radiofrequency cavities to accelerate the hydrogen ions up to 160 MeV and gain 5% in mass. Secondly, the hydrogen ions are injected into the next accelerator in the chain, Proton Synchrotron Booster (PSB), and the energy of proton beams is raised to 2 GeV. Meanwhile, the ions are stripped out of two electrons, becoming pure proton beams. Then the proton beams enter into the Proton Synchrotron (PS), which pushes the beam up to 26 GeV. Before sending the beams into the LHC, the Super Proton Synchrotron (SPS) accelerates the beams up to 450 GeV. Finally, the protons beams will be split into two beams and injected into the LHC. One beam circulates clockwise in one beam pipe, while the other beam circulates counterclockwise in the other beam pipe.

The total of 16 RF cavities in two beam pipes in the LHC is responsible for accelerating the beams from 450 GeV to 6.5 TeV in 20 minutes. The oscillating electromagnetic waves (frequency of 400 MHz) in RF cavities are generated by high-power klystron by means of the waveguides. At the same time, to stabilize the beam bending in the rings, the magnetic field increased as the beam energy raised, known as "ramping". Once the energy of beams

doi:10.6342/NTU202300054

arrives at the 6.5 TeV, the beams will be transferred into collision mode. The cross-section of beams is "squeezed" into minimum size ($10\mu m$) to achieve higher luminosity. Besides, the accelerated proton achieving the required energy could be earlier or later, so the protons will be accelerated or decelerated by the RF cavity, focusing the beams in phase and forming the "bunches". Finally, the adjusted bunch crossing collides in the particle detector (CMS, ATLAS, LHCb, and ALICE) and starts the data taking.

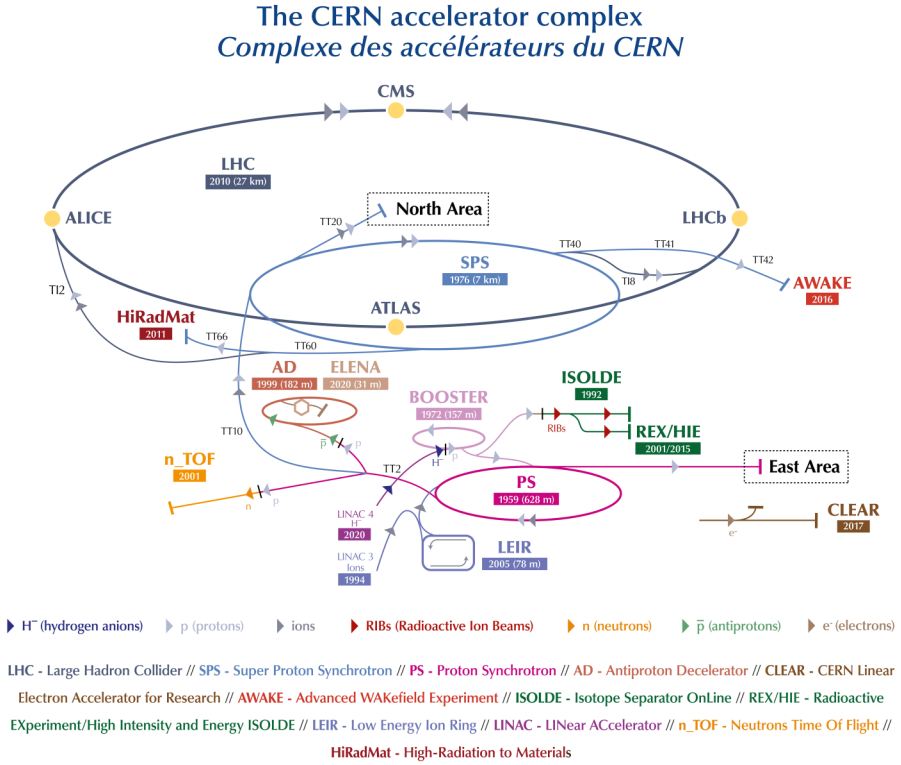

Figure 2.2: The succession of accelerators.

2.1.2 Luminosity and Pileup

Luminosity is one of the important features of an accelerator that reflect the number of proton-proton collisions per unit second. For a given process X, the number of interations is the product of the instantaneous luminosity ($\mathscr{L}_0$) and the cross section of the process $\sigma_{pp\to X}$:

$$N_X = \mathscr{L}_0 \, \sigma_{pp\to X} \tag{2.1}$$

Therefore, to get the observed number of specific process, it is necessary to know its cross section and the instantaneous luminosity integrated over a perid of time of the operation of machine. In addition, if both the proton beams in opposite directions follow the Gaussain

doi:10.6342/NTU202300054

Parameter	2016	2017	2018
Peak luminosity ($10^{34} cm^{-2} s^{-1}$)	1.4	2.1	2.1
Average pile up	25	38	37
Max. no. of bunches	2220	2556/1868	2556
No. of stable beams($10^1$1)	1.0-1.25	1.0-1.25	1.0-1.25
Bunch spacing(ns)	25	25	25

Table 2.1: Parameters of the LHC for 2016, 2017 and 2018 from [11]

distribution and have the equal beam parameters, the simplest instantaneous luminosity is given by

$$\mathscr{L}_0 = f \frac{n_1 n_2}{4\pi\sigma_x\sigma_y} \tag{2.2}$$

where n_1 and n_2 are the numbers of protons in the colliding bunches, and the f represents the frequency of the colliding. σ_x, σ_y are the root-mean-square horizontal and vertical beam sizes.

2.2 Compact Muon Solenoid detector(CMS)

The Compact Muon Solenoid (CMS) detector [20] is one of the main detectors built in the LHC. It has a broad physics mission from studying the Standard Model to searching beyond Standard Model. Although the program is the same as the ATLAS experiment, the design and the technical solution are different from ATLAS. The CMS detector is a cylindrical detector encircled by the coil of superconducting cable that generates a field of 4 Tesla, about 100,000 times the Earth's magnetic field. The complete detector is about 21 meters long, 15 meters wide, and 15 meters high. It consists of several layers of the subdetector, including the inner tracker system, electromagnetic calorimeter (ECAL), Hadron calorimeter (HCAL), and Muon detector. The following sections will introduce the machanism of the subdetectors and the trigger system in the CMS detector.

2.2.1 Coordinate system

The right-handed coordinate system is adopted in the CMS detector. The direction that proton beams move in the counterclockwise of the circle is defined as the z-axis, while the x-axis points to the center of the LHC ring and the y-axis points to the upward of the detector as illustrated in figure 2.4. Conventionally, the transverse plane is defined in the x-y plane,

doi:10.6342/NTU202300054

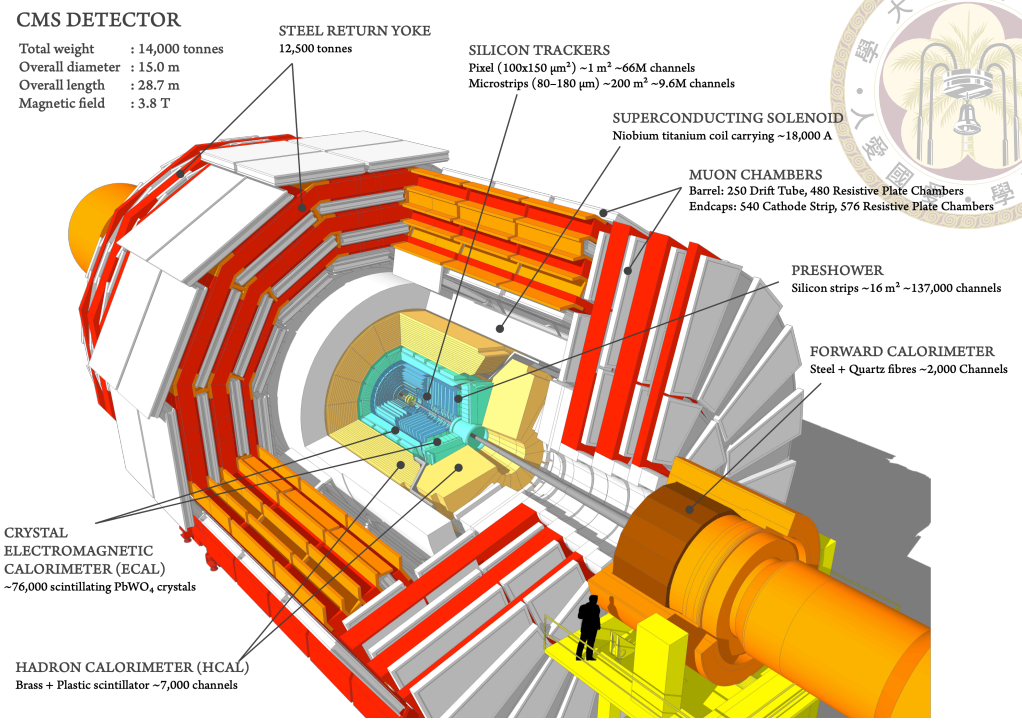

Figure 2.3: Illustration of CMS detector in the cross-section.

and the longitudinal part is defined in the z-axis. Moreover, because of the cylindrical shape of the CMS detector, it is conventional to define the azimuthal angle ϕ as the angle from the x-axis to the y-axis in the transverse plane, and the polor angle θ between the z-axis and $\vec{r}$ vector.

A distinction is drawn between the conventional cylindrical coordinate and the coordinate used in the high energy experiment physics. The polor angle is described by an observable variable "rapidity", defined as:

$$y = \frac{1}{2}\ln(\frac{E + p_z}{E - p_z}) \tag{2.3}$$

where E and p_z are the measured energy and momentum of the final state. Despite the proton-proton colliding in the opposite direction with the same momentum, the fraction of momentum of the parton is unknown. The inequivalent net longitudinal momentum of parton may lead to the final state boosting along the z-direction. The advantage of using rapidity is that the rapidity difference is an invariant quantity under boosts along the beam direction. It can be also expressed in the polar angle θ by neglecting the mass of final state and assuming its momentum $p_z \approx E\cos\theta$, the "pseudorapidity" η defined as:

$$\eta = \frac{1}{2}\ln(\tan\frac{\theta}{2}) \tag{2.4}$$

Besides, transverse momentum $p_T = \sqrt{p_x^2 + p_y^2}$ and azimuthal angle ϕ are invariant under the

doi:10.6342/NTU202300054

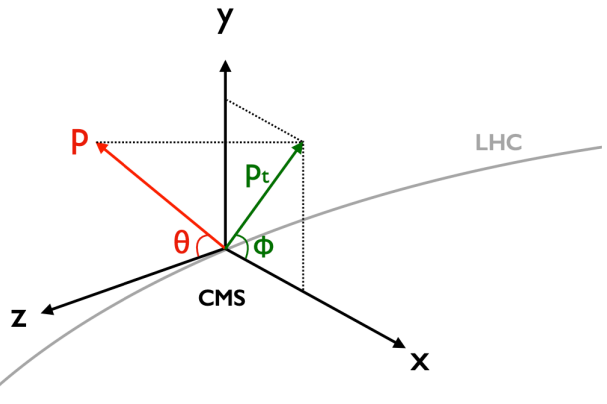

Figure 2.4: Illustration of the coordinate of CMS detector. [2]

longitudinal boost. Following the same reason, it is common to use rapidity and transverse components for other physical observable such as transverse energy $E_T = \sqrt{m^2 + p_T^2}$ and spatial angle $\Delta R = \sqrt{\Delta\eta^2 + \Delta\phi^2}$.

2.2.2 Inner tracker system

To reconstruct the trajectories of particles and measure their momentum, the tracker of CMS contribute to record these property accurately [20]. When particles travel the tracker, the ionization happens in the silicon and create electron-hole pairs. Via collecting charges from electric current, the electric signal has been recorded by 15840 readout chips(ROC) and amplified to be our tracks of particles. The tracker composes of two parts: silicon pixel detector in the inner tracker and silicon strips detector in the outer tracker.

Silicon pixel detector has 3 cylindrical layers (distant to the beam pipe 4, 7, 11cm) and 65 million pixels in total. Every pixel sensor is 100 um by 150 um, about two hairs width. Since it is the closest to the beam pipe, it not only plays an important role on recording the very short-life particles but also handles the highest intensity of particles.

The silicon strips detector is divided into four parts, including inner barrel (TIB) layers, two inner endcaps (TID), the outer barrel (TOB), and two endcaps (TEC), as the figure 2.5 distributed. The total amount of the silicon strip detector is about 10 million detector strips with 72,000 microelectronic readout chips. They cover the range of $\eta < 2.4$, such that the silicon strips detector has a good spatial resolution to the tracks of particles. The principle of detection of silicon strips is almost the same as pixels. Besides, due to the nature of the silicon, the detectors are kept at -20 ∘, minimizing the disorder.

doi:10.6342/NTU202300054

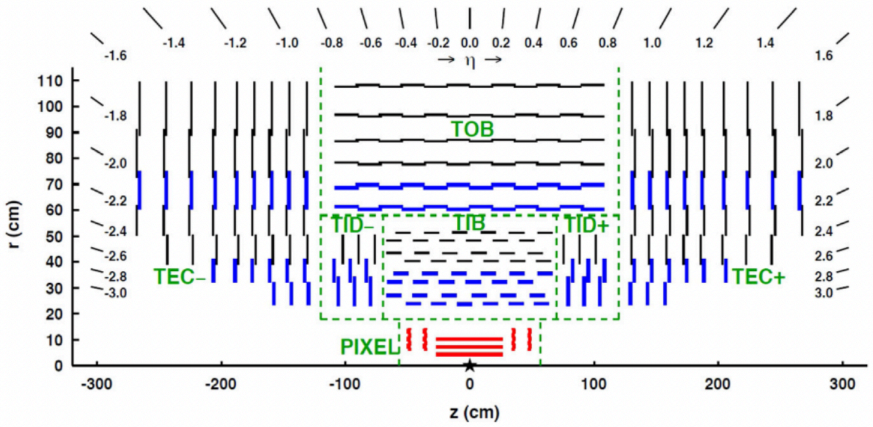

Figure 2.5: The arrangement of the inner tracker system [3].

2.2.3 Electromagnetic calorimeter

Some final states of particle decay in the Standard Model are electrons and photons. To measure the energy of electrons and photons, suitable material to stop the electrons and photons carry with high energy is needed. Moreover, the high energy particle interacting with dense matter is dominated by the bremsstrahlung radiation and electron-positron pair production, which lead to the electromagnetic showers(EM shower). The average distance of the electromagnetic shower that occurs in the specific material is defined by the radiation length(x_0).

The Electromagnetic calorimetry consists of 75848 PbWO4 (lead tungstate) crystals in the Ecal barrel (EB) and Ecal Endcap (EE), covering the barrel up to $\eta = 1.48$ with an inner radius of 129 cm, and Endcap up to $\eta = 1.48$. The PbWO4 has good radiation resistance due to its short radiation length($x_0 = 0.89\ cm$ and its high density(8.28 g/cm^3). Each lead tungstate crystal installed in the Ecal is weight 1.5 kg, and the size of lead tungstate in the barrel is $2.2 \times 2.2 \times 23\ cm$ and for endcaps is $3 \times 3 \times 22\ cm$. The scintillation light produced by the electromagnetic showers is collected by Avalanche Photodiodes (APDs) in the barrel and vacuum photodiodes (VPTs) in the Endcaps. By amplifying the signal of the scintillation light, we can measure the energy of the electrons and photons since the amount of the light is proportional to the total energy of the electron and photon.

The Preshower (PS) is installed in front of the two endcaps, covering the forward region at $1.653 < |\eta| < 2.6$. The thick of the Preshower is about 20cm and is comprised of two layers of silicon strip sensors. They are designed to improve the resolution of the neutral pion (π_0).

doi:10.6342/NTU202300054

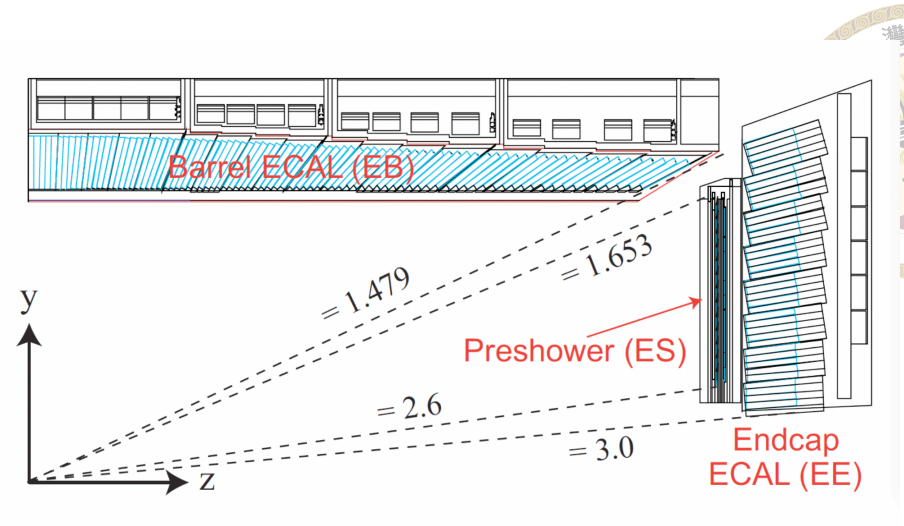

Figure 2.6: Sketch of the cross section of the half of ECAL. The collisions point is at the lower left corner.[4]

2.2.4 Hadron calorimeter

The hadron calorimeter (HCAL) [20] outside the ECAL was designed to reconstruct the physics from hadronization, such as mesons, and baryons which are made up of the quarks and gluons. It also provides the indirect measurement of non-interacting particles, neutrinos, by the missing transverse energy. The HCAL is a hermetic calorimeter to avoid any possible physics from collisions undetected. The dense absorber which aims to produce hadronic showers is composed of flat brass alloy with 70% Cu and 30% Zn, known for a radiation length of 1.49 cm and the interaction length (λ_I) 16.42 cm. The scintillators to produce rapid light pulses when the hadronics shower is produced are made of tiles of plastic.

The HCAL is separated into four parts: a barrel (HB), two endcaps (HE), an outer part (HO), and an additional forward part (HF). The radial range of HB is from the outer extent of the ECAL Barrel (R = 1.77 m) to the inner extent of the superconducting magnets coil (R = 2.95 m) and covers the range $|\eta| < 1.3$. There are 17 layers of active plastic scintillator tiles bolted together with absorbers, giving a granularity of 0.087×0.087 in the HB, which is matched to the ECAL barrel. Within the magnet coils, there is an outer calorimeter (HO) design in order to measure the energy of hadron showers leakage outside the HB efficiently. The HE covers the range $1.3 < |\eta| < 3.0$ and consists of 18 layers of absorbers inserted with the scintillators. The granularity of HE absorbers is 0.087×0.087 for $|\eta| < 1.6$ and 0.17×0.17 for $|\eta| \geq 1.6$. The final part is the HF, which is located 11 m away from the center of the CMS detector, and covers $2.85 < |\eta| < 5.19$. It is made of steel absorbers with a cylindrical structure (inner radius 12.5 cm, outer radius 130 cm, 1.65 m long) and inserted with radiation-hard quartz fibers since HF will experience unprecedented particle fluxes compared to the rest of the calorimeter. The signal is generated from the Cherenkov lights produced by charged

doi:10.6342/NTU202300054

shower particles.

Finally, after the hadronic shower was produced, Hybrid Photodiodes (HPDs), converting the light into electrons by the photoelectric effect, amplified and collected the signal of the hadronic shower.

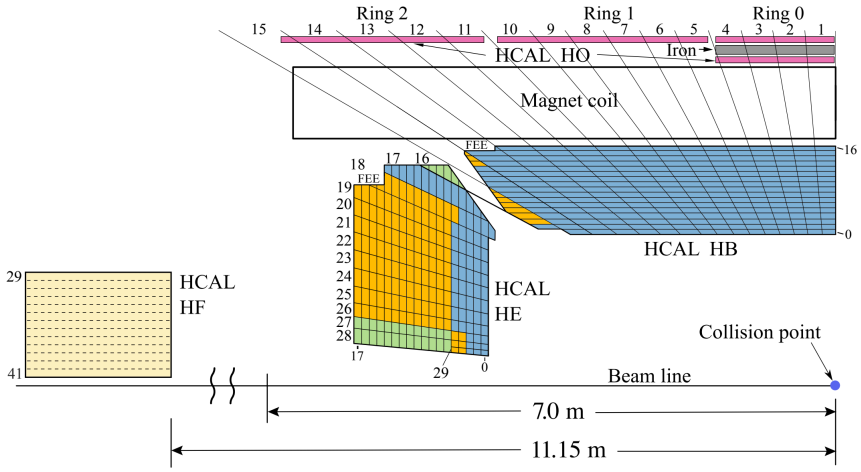

Figure 2.7: Sketch of the cross section of the half of HCAL. The collisions point is at the lower right corner. [5]

2.2.5 Solenoid magnet system

One of the features of CMS is its Superconducting magnet. It is a large solenoid that locates outside the ECAL and HCAL and consists of a compact coil of superconductivity fibers with a current of about 18500 amps. Due to the property of superconductivity, it makes the electricity flow without resistance and leads to a large magnetic field of about 4 Tesla, which quantity is 100,000 times stronger than the magnetic field of the earth. The purpose of the superconducting magnet is to measure the momentum and tracks of the charged particles. The strong magnetic field curves the charged particle so that the particles are able to be distinguished by measuring their momentum accurately. Nevertheless, the return magnet field outside the coils is non-uniform which not only reduces the strength of the magnetic field in the muons detector but also cause the dubious trajectories of the muon. In order to overcome the disadvantages, steel "return yoke" were interleaved in the muons detector. This increases the magnetic field up to 2 Tesla in the muon detector and gives a better resolution of muon measurement. The distribution of the magnetic field is shown in figure 2.8.

doi:10.6342/NTU202300054

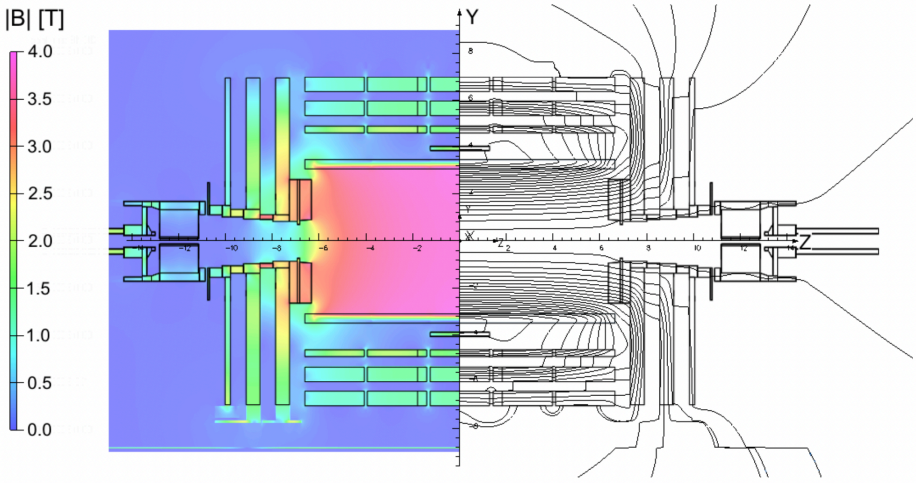

Figure 2.8: The distribution of magnetic field strength in the left half of diagram and the magnetic lines in the right half of diagram.

2.2.6 Muon Detector

The outermost layer of the CMS detector is the powerful muons detector and provides 3 functions: muon identification, momentum measurement, and triggering. Different from most particles, the muon can penetrate the irons for several meters, thus the muons detector must be placed in the last layer detector. The muon detector is shaped the cylindrical, including a barrel section and two endcaps sections, and includes a total of 1400 muon chambers: 250 drift tubes (DTs), 540 cathode strip chambers (CSCs), and 610 resistive plate chambers (RPCs). To begin with, DTs provide the measurement of muon position in the barrel part ($|\eta| < 1.2$). As the muon travels through the DTs, drifting in the gas (85% Ar + 15% CO2) for a drift velocity of 0.055 mm/ns, ionized the gas toward the anode. Secondly, CSCs are located in the endcaps ($0.9 < |\eta| < 2.4$) where the magnetic field is uneven and the rate of particles is high. The gas of CSC comprises CO2 (50%), Ar (40%), and CF4 (10%) gas, which provides good timing and spatial performance. The last chamber is RPCs which are mounted in both barrel and endcaps. When muon ionizes the gas, causing an avalanche, send to the readout to form a signal quickly.

2.2.7 Trigger System

The LHC provides proton-proton collisions and heavy-ion collisions at high rates, with a crossing frequency of 40 MHz. The limit of CPU and disk storage can not store all data from such high rates and the high luminosity in collisions. Therefore, the trigger system is designed to reduce the information that is not physics of interest and save the disk storage.

doi:10.6342/NTU202300054

The first step to reducing events is the Level-1 Trigger (L1), which is customized electronic hardware, that filters the data preliminarily. The second step is the High-Level Trigger (HLT), which is a software system, that selects the data passing a higher threshold of physics conditions [21].

The online L1 trigger has to decide within 5 μs of a collision whether the events should be accepted or rejected. It reduces events from the maximum rate of 40 MHz to 100 kHz. The L1 trigger reconstructs roughly the most interested physics quantity and objects such as the electron, photon, jets, missing transverse energy, etc., through the information from the trigger primitives (TP) of ECAL and HCAL and from the chambers in the muon detector. The process of L1 trigger is shown in 2.9. Once the event satisfies the requirement of the criteria of the L1 trigger, the events are sent into the High Level Trigger (HLT) system.

The HLT system runs under 32000 CPU core. The more complex algorithm built in the software of HLT provides more sophisticated physical object and reconstruction, such as shower shape, isolation, primary vertex, and so on. There are several HLT targeted to different physics analyses so that the analysis is able to employ the dataset that includes specific physics objects.

Besides, since the quantity of data in the CMS experiment is so massive that occupies the storage space and lowers the efficiency of the CPU, triggers are divided into prescaled and unprescaled. A prescaled is to reduce the rate of data taking. The integer prescales are used in the CMS. A prescale trigger with integer value X means only one out of X events will fire the trigger. It is available for different integer values at the L1 trigger and HLT. That is, if the L1 trigger only accepts one out of 100 events, while HLT only accepts one out of 4 events that came from the previous L1 trigger. The prescaled trigger not only enriches the database at CMS but also saves significant CPU time. Whereas unprescaled trigger does not reduce the rate of data taking. It accepts all events if events satisfy the threshold of the trigger.

2.2.8 Data Format and Monte Carlo Production

Before analyzing the data from pp collision, simulation of the event's production plays an important role to understand the physics process in the expectation. The Monte Carlo sample (MC) is used to simulate the events from pp collision, which consists of GEN-SIM-DIGI-HLT-RECO steps.

- **GEN-SIM** The Monte Carlo sample (MC) is produced beginning from the MadGraph5_aMC@NLO (MG5) [22], called GEN step. It is a framework that aims to

doi:10.6342/NTU202300054

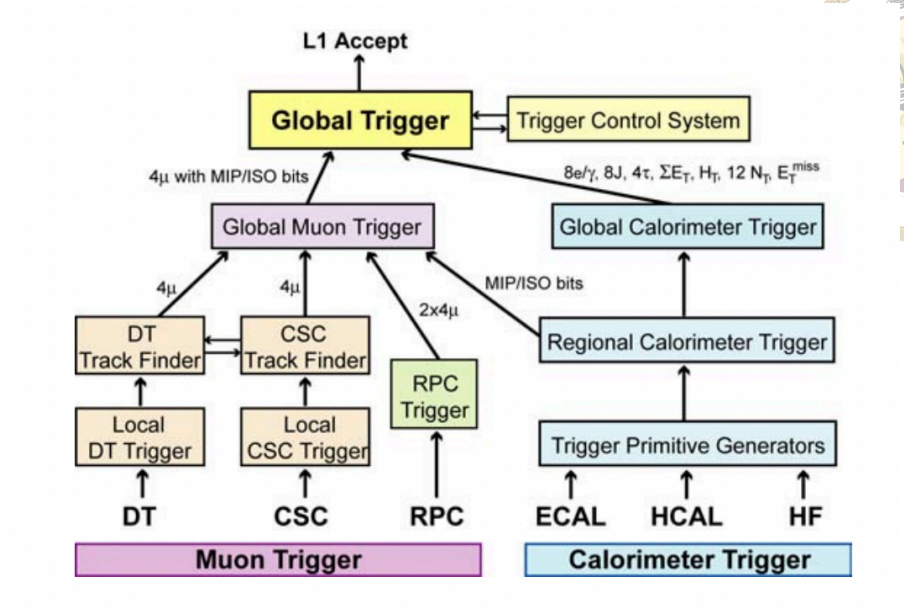

Figure 2.9: The flow diagram of Level 1 Trigger.

generation all the elements for SM and BSM phenomenology, providing the computation of cross-section and the generation of hard events. Given a model and process, the leading order and next leading order can be computed in accuracy for any user-defined Lagrangian. The unweighted events after the simulation are stored in the Les Houches events (LHE) file. The physical parameter for monopole search is described in chapter 3.

While MG5 only gives the target final states without full processes, such as parton shower and hadronization, so the successive process is held by PYTHIA 8 [23]. PYTHIA is a standard tool for the generation of events in high-energy physics. It involves the simulation of the hard process for the initial and final state parton shower.

In the final step of the simulation, GEANT4, which is software installed in the CMS software (CMSSW) that contains the detector' s geometry with sensitive layers to detect the particles, provides the simulation of particles interacting with the CMS detector. The simulation above is called "SIM" step.

- **DIGI-HLT-RECO**

  Once the SIM step is finished, the digitization process ("DIGI" step) takes place, which provides the hits information in the active layers of the detector as the real detector readout. Afterwards, the digitization information are reconstructed to the physical event ("RECO" step) and distributed according to the HLT trigger ("HLT step"). A large amount of algorithms to reconstruct particles have been built in the CMSSW, giving a variety of method to identify the particles we are interesting. Finally, the output ROOT file will be converted into our analysis object.

doi:10.6342/NTU202300054

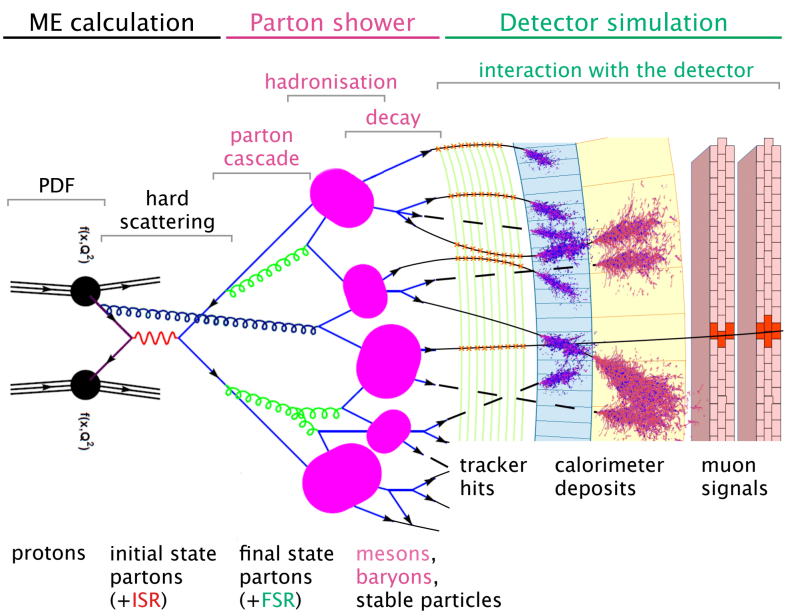

Figure 2.10: A schematic flow of how the MC sample for our analysis was generated. From the beginning of matrix element calculation is dominated by MadGraph5_aMC, the following Parton shower and hadronization are handled by the PYTHIA8. The last step, detection simulation is conducted by GEANT4.

The most original format of data is comprised of digital information, called RAW data. The RAW data then passes through the reconstruction step to convert the digital signal from the detector into usable analysis objects for physicists to analyze. In this stage, the data format contains multiple kinds, such as reconstructed data (RECO), analysis object data (AOD), miniAOD, etc. Besides, the data are categorized into specific datasets according to the trigger result. At last, depending on the different requirements of physicists, various data types can be used to study.

doi:10.6342/NTU202300054

doi:10.6342/NTU202300054

Chapter 3 Simulation of Magnetic Monopole

The chapter describes the simulation of monopole production and monopole interaction in the CMS detector. To begin with, the first section illustrates the monopole production model, which contains the property of the model and the production mechanism of monopoles. Secondly, the kinematics of monopole for different hypothesis mass points is presented. At the end of this chapter, the monopole signature from the simulation that interacts with the CMS detector is described in the last section.

3.1 Monopole production

At the LHC, several extension models to discover new physics have been developed and been able to search in the CMS detector. One of the most popular new types of particles in these models are Long-lived particles (LLP), which are caused by suppressed couplings, highly virtual processes, and so on [24]. The lifetime of LLPs is supposed to be long enough, such that they can arrive or pass through the detector before they decay. In this search, the monopole, viewed as a kind of LLP, is considered to be stopped in the ECAL.

The monopole can be produced by photon fusion and Drell-Yan (DY) process [25]. In this thesis, the monopole production is based on the DY process which is very common in the hadron-hadron collider. The typical DY process is that a quark and an antiquark annihilate into a virtual photon as the propagator, producing lepton and anti-lepton pair in the final state. DY process can produce monopole-antimonopole pair in the framework of an effective U(1) gauge field theory with the conventional assumption of spin-0, spin-1/2, or spin-1 for the pure magnetic monopole. The Feynman diagram of monopole-antimonopole pair production via the DY process is plotted in figure 3.1.

The monopole production model utilized in the thesis is regulated by specific properties and generates events by MadGraph5_aMC@NLO (MG5). It is set to produce 100,000 events

doi:10.6342/NTU202300054

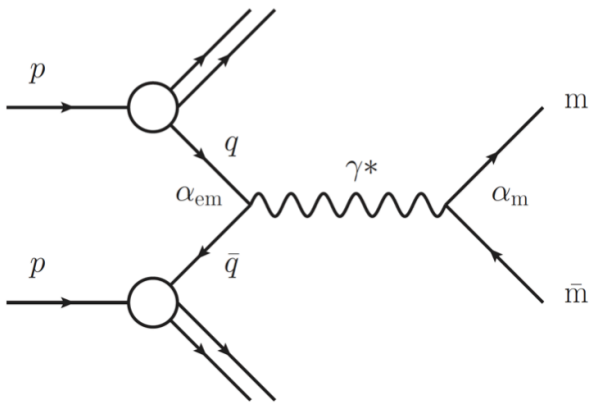

Figure 3.1: Feynman diagram of monopole-antimonopole pair production from Drell-Yan process [1].

property	parameter
production	Drell-Yan process
spin	1/2
charge	$1g_D$ (Dirac monopole)
center of mass energy $\sqrt{s}$	13 TeV
generated event	100,000
mass point (TeV)	1, 1.5, 2, 2.5, 3, 3.5, 4, 4.5
particle ID (PID)	± 4110000
PDF model	NNLOPDF
p_T limit	> 10 GeV

Table 3.1: List of all property of monopole production model in the search.

of monopole-antimonopole pair production with spin-1/2 via the DY process in 13 TeV of the center of mass energy. Notice that the model is β[1]-independent, which means that the cross-section of monopole production does not vary with the β (velocity) [2] Furthermore, the threshold of transverse momentum is limited to be larger than 10 GeV, in order to ensure that the monopole carries sufficient momentum to reach the ECAL in the CMS detector. The hypothesis monopole mass points are set to be 1, 1.5, 2, 2.5, 3, 3.5, 4, 4.5 TeV in this search. All physical parameters and the PDF model used in this model are listed in the table 3.1.

3.2 Generator Level Kinematics

Kinematics of generated monopole from proton-proton collision in the center of mass $\sqrt{s}$ = 13 TeV are plotted in figure 3.6.

[1] $\beta = \sqrt{1 - \frac{4M^2}{s}}$, where M is particle mass and s is the center of mass energy

[2] Some theorists have developed the β-dependent model for monopole production in ref.[22].

doi:10.6342/NTU202300054

Firstly, Figure 3.6 (a) and 3.6 (b) and shows that the distribution of position when monopoles are produced. The distribution of η implies that monopoles produced almost within the coverage of ECAL ($\eta < 3$), and most of them occur in the ECAL barrel ($\eta < 1.48$). In ϕ direction, monopoles distributed in uniform. Secondly, the distribution of transverse momentum of monopoles increases along with the heavier mass, though heavier monopoles go more slowly, as the comparison of the velocity (γ vs β) of mass 1000 GeV and mass 4000 GeV in figure 3.6 (e) and figure 3.6 (f). The distribution of the velocity (γ vs β) also proved that monopoles travel at non-relativistic speed. In addition, the distribution of total momentum in figure 3.6 (d) is toward to higher magnitude because the momentum in the z-component is sufficiently great.

3.3 Monopole's signature in CMS detector and Event display

After producing the monopole-antimonopole pair production events, the monopole's signature interacting in the detector can be simulated by GEANT4, which provides a complete CMS detector model to simulate particles from proton-proton collision interacting with the detector. The event simulation can be visualized in software called Fireworks (or called cmsShow), which is a framework to visualize the events (including event production and energy deposition, etc.) in 3D or 2D view.

A selected monopole production event (mass 1000 GeV) is displayed using a reconstructed root format file which stores the information of generated monopole from the SIM step and of the reconstruction event from the RECO step. The analysis benefits from the Fireworks to confirm the validity of the simulation by means of matching the position between generated monopole and reconstructed monopole. The following description will go with the event display to illustrate the monopole signature in the CMS detector.

As mentioned, the transverse momentum of the monopole is set to be larger than 10 GeV, to ensure that monopoles can transverse the beryllium beam pipe, travel through the Tracker system, and be stopped in the ECAL finally, though the monopole travels at non-relativistic speeds due to its heavy mass.

After passing through the beam pipe, the monopole then travels through the silicon Tracker system which records the trajectories of particles by energy loss of particles. Monopoles have two salient features in the Tracker system. Firstly, the trajectories of monopoles are different from the electrically charged particles. The strong magnetic field in the CMS detector forces monopoles to curve along with the magnetic field or opposite and become parabolic. However, the reconstructed event shows that the bending may not

doi:10.6342/NTU202300054

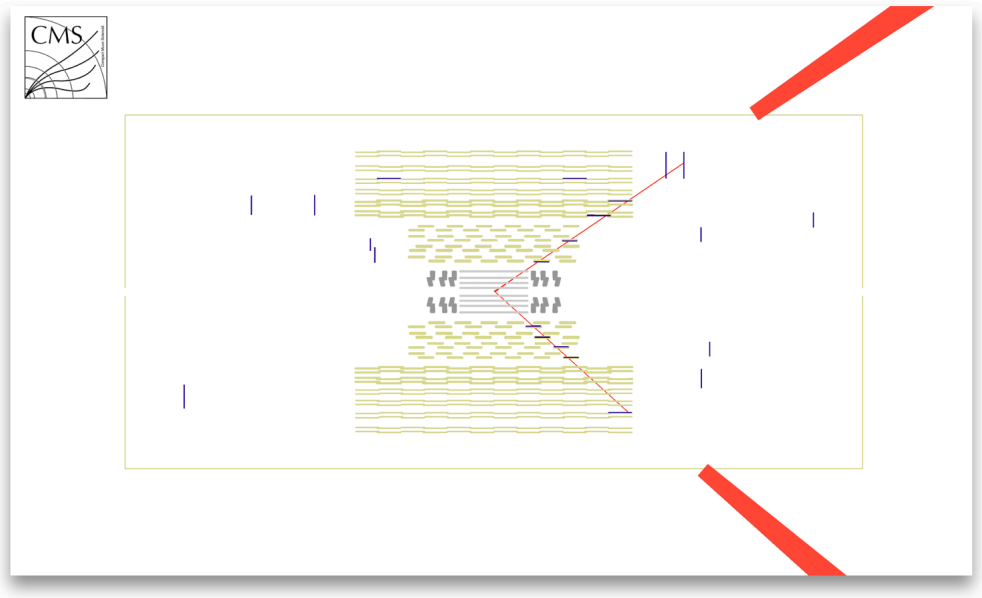

Figure 3.2: Event display of reconstructed monopole and antimonopole, plotting in the r-z plane. The rectangle edge distinct the inner Tracker system and the outer ECAL. The red cone below shows the monopole energy deposition (on a specific scale) in the ECAL. The green lines within the ECAL are the tracks of monopole pairs. The saturated strips are presented in deep blue where some saturation is caused by noise, while some saturation along the green tracks is caused by monopole pairs.

significant enough, such that the track is a straight line approximately, as the green tracks shown in figure 3.2. On the other hand, the monopole as a high ionized particle (HIP) is expected to release energy in the tracker at least multiple orders of magnitude than the electrically charged particle in SM, leading to saturate the silicon strips. Figure 3.2 depicts that the saturated strips in yellow occur along the tracks of the monopole pair (green line).

Finally, the monopoles are stopped in the ECAL, depositing most energy in the ECAL crystals. Because the amount of charge a monopole carries is 68.5 times as an electron, it is expected to radiate all its kinetic energy rapidly in the ECAL crystals and leading to the monopole almost leaving negligible or zero energy in the HCAL. Nevertheless, the rapid radiation in the crystals causes the monopole signal looks like a "spike", in other words, energy is deposited almost in one crystal of ECAL. Figure 3.3 displays detailed views of a spike-like monopole and a monopole depositing energy in multiple crystals, where a small pink point represents a crystal and a big grid clustered in 5x5 crystals is an ECAL cluster. The latter monopole is just like an electron or a photon, depositing energy dispersively in several crystals, forming a so-called electromagnetic (EM) shower. This characteristic leads to the failure to trigger signal events in the L1 trigger potentially.

doi:10.6342/NTU202300054

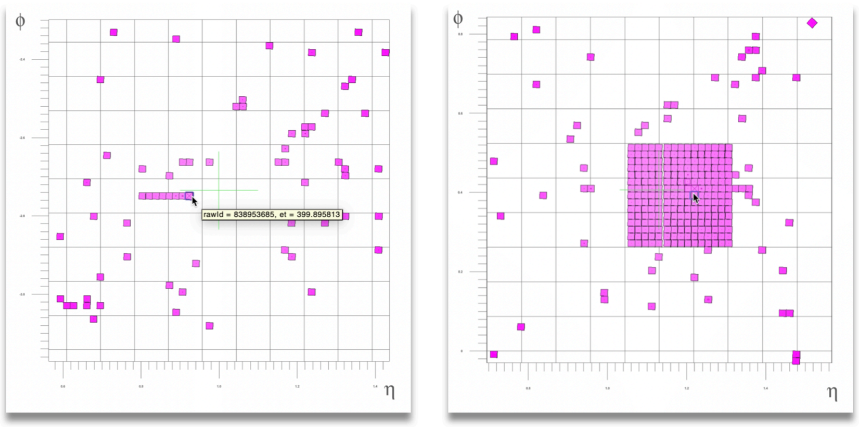

Figure 3.3: The plot of two ECAL cluster detail, where a small pink point represents a crystal and a big grid clustered in 5x5 crystals is an ECAL cluster. The left plot shows a spike-like monopole with its energy concentrated in one crystal (where the cursor points). The right plot is a monopole depositing energy in several crystals disperively, just like a photon or electron.

3.3.1 Level-1 Spike Killer Algorithm

Despite the remarkable signature of monopole in the ECAL, the spike-like characteristic poses the thorniest problem in the search. Anomalous signals – ECAL spikes – are a common phenomenon that the particles strike the APDs and interact to produce secondary particles accidentally, then ionize the silicon, leading to the anomalous signal with high energy (exceeding 100 GeV) in isolated crystal [26]. Thus, a spike killer algorithm or called strip Fine-Grained Veto Bit (sFGVB) algorithm has been developed and built into the L1 trigger to prevent the spikes from making large missing transverse energy (MET) in the reconstruction. That is to say, monopole signals in the ECAL might be identified as an ECAL spike by the algorithm.

Figure 3.4 illustrates how sFGVB algorithm works. To begin with, it scans a "strip" (5x1 crystal) to compare each channel with a specific threshold. If only one channel in the strip is above the threshold, the strip is configured to 0 and identifies the channel as a spike. Whereas, if there is more than one channel above the threshold, the strip returns 1 as the channels being an EM shower. Following this, zero results for sFGVB were then compared to the threshold of the ECAL trigger tower (5x5 crystals as a readout in ECAL). Once the trigger tower transverse momentum is greater than 12 GeV, the energy deposition for this channel is considered as an ECAL spike and then removed it. It has rejected > 95 % of spikes since the sFGVB has been operated.

Furthermore, the offline rejection of spike is built in HLT-level. The topological variable "Swiss-Cross" (see figure 3.5 (a) and timing method (spike usually happens earlier than

doi:10.6342/NTU202300054

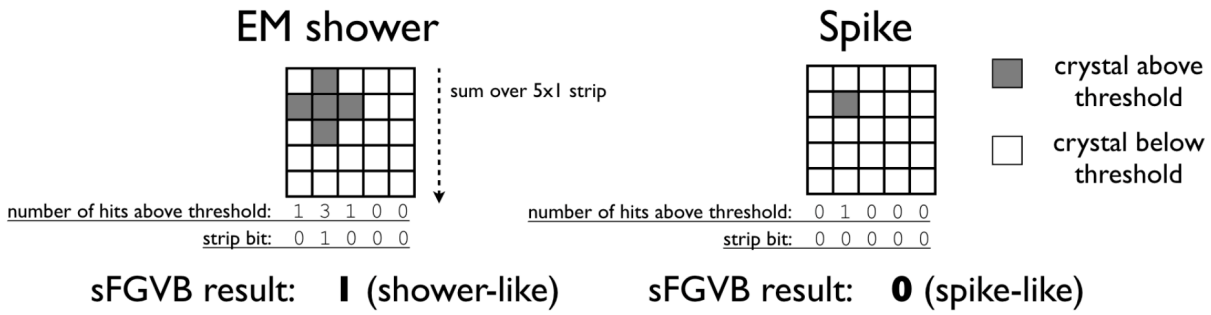

Figure 3.4: Illustration of mechanism of sFGVB algorithm.

the collision events) have been developed to clean more spikes that miss in the L1 trigger. The study shows that the efficiency of rejection achieved to about 99% and makes good consistency of MET between the simulation and spike-cleaned data, as shown in figure 3.5 (b).

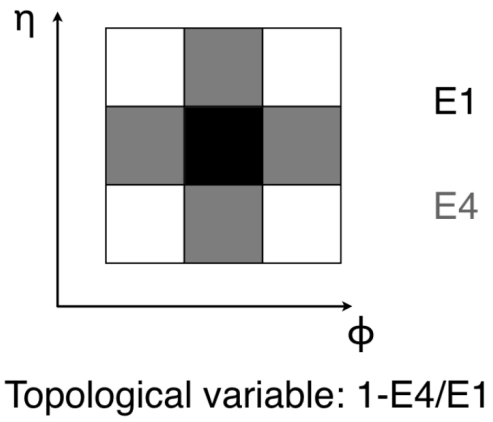

(a) Topological variable to reject the ECAL spike.

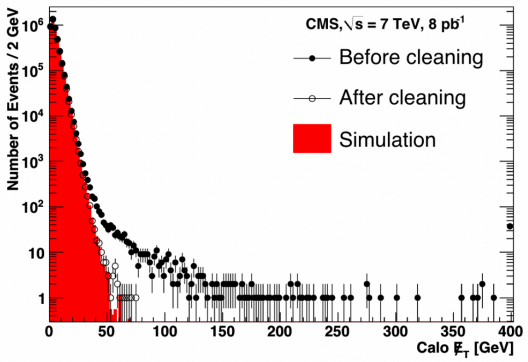

(b) The large MET caused by spikes has been improved after removing the spikes.

Figure 3.5

Overall, monopole signals suffer from both online and offline spike killers which are unavoidable because the data must pass through the L1 trigger and HLT trigger. This impact remarkably the signal efficiency in the analysis because monopoles could be treated as an ECAL spike by the trigger. The following chapter will discuss and investigate how the analysis deal with this challenge.

doi:10.6342/NTU202300054

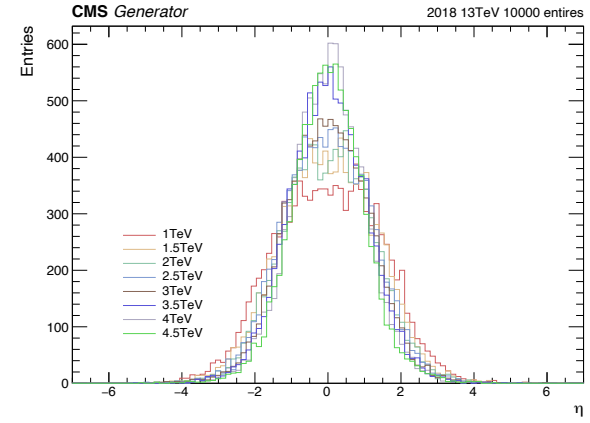

(a) distribution in η

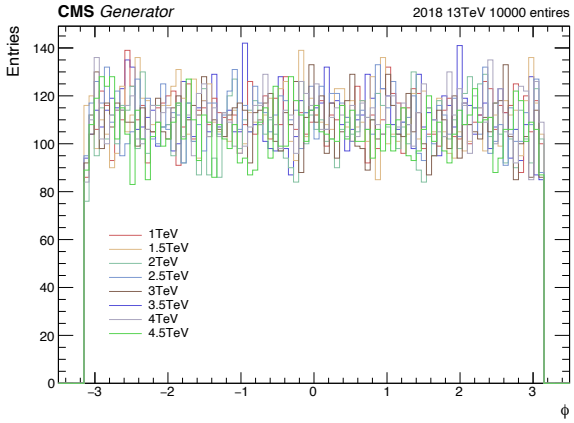

(b) distribution in ϕ

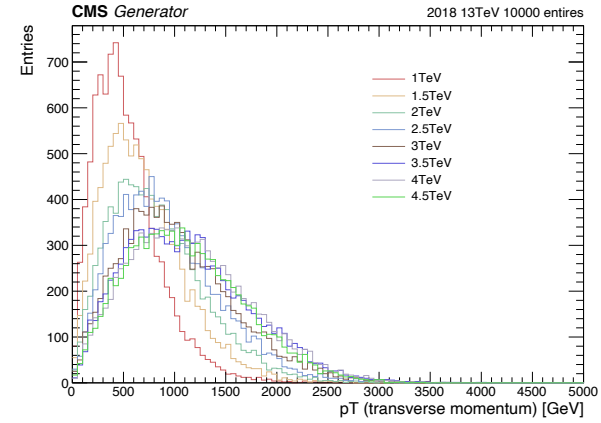

(c) transverse momentum (GeV)

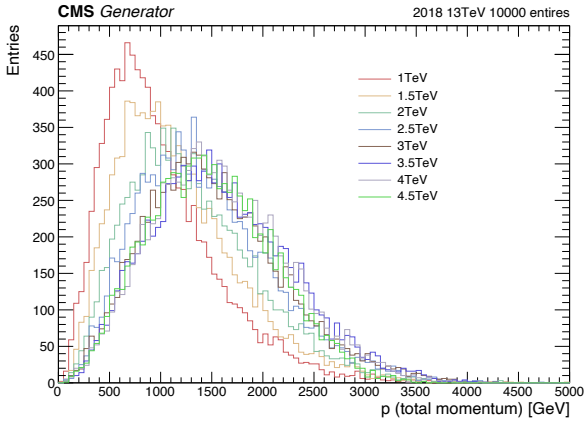

(d) total momentum (GeV)

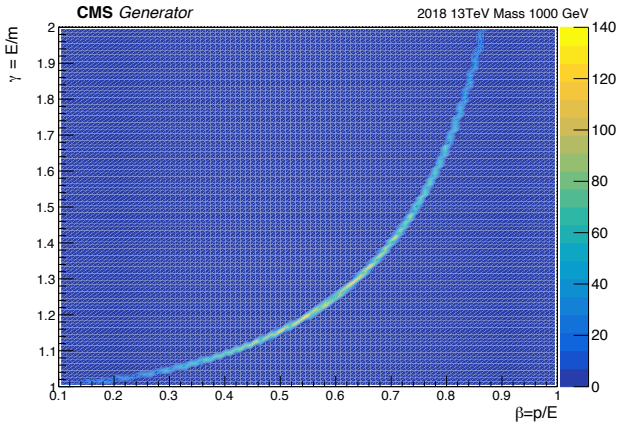

(e) Monopole 1000 GeV: γ vs β

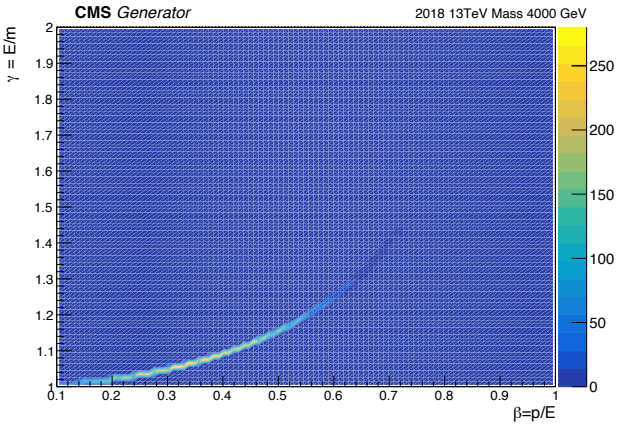

(f) Monopole 4000 GeV: γ vs β

Figure 3.6: Kinematics of generated monopole with 10000 events plotted for each mass point from 2018 MC sample.

doi:10.6342/NTU202300054

doi:10.6342/NTU202300054

Chapter 4 Analysis strategy

In this analysis, the first thing is to reconstruct the magnetic monopole based on the signature of the monopole in the CMS detector by using the simulation Monte Carlo (MC) described in the last chapter. Since the magnetic monopoles involve in the electromagnetic interaction, we expect most monopoles are stopped in the ECAL, remaining less energy in the HCAL, thus the topic will cover the event reconstruction in the Tracker, electromagnetic calorimeter (ECAL), and Hadronic calorimeter (HCAL).

4.1 Tracking Reconstruction

Monopole carries a magnetic charge such that it is expected to curve along the direction or the opposite direction of the strong magnetic field produced by the solenoid magnet in the CMS detector. Unlike other electric charge particles, which circulate on the $x-y$ plane in the magnetic field, the monopole has curvature in the z-direction. As a result, the trajectory of the monopole is different from the electric charge particle. However, the standard tracking reconstruction in the CMSSW is not adoptive in the tracking reconstruction of the monopole. The algorithm for monopole search has been built, the detail of the tracking algorithm is described in 4.1.1.

Apart from the different trajectories, the energy loss in the tracker left by monopoles has several orders of magnitude higher than the normal track because monopole is the high ionized particle that tends to saturate the strips, leading to high energy loss in the tracker, as discussed in the previous chapter. Therefore, the tracking ionization would be a significant part of the reconstruction as described in 4.1.2.

doi:10.6342/NTU202300054

4.1.1 Track Combination Algorithm

We have two fits to satisfy the trajectory of monopole. The first fit is to fit a parabola in the $r-z$ plane.

$$z = d + f\rho + g\rho^2 \tag{4.1}$$

where $d\ cm$ corresponds to the distance of the monopole move along the z direction, which is the direction of the strong magnetic field. f is the gradient in $r-z$ plane, and g is denoted by the $r-z$ curvature.

The second fit is a circle in the x-y plane, which is the projection of the helical track, since the monopole could be electrically charged and curve in the x-y plane.

$$y = a + sign(c)\sqrt{c^2 - (x-b)^2} - c \tag{4.2}$$

where x and y correspond to the x-y plane of the coordination. Parameter $a\ cm$ is the impact parameter, c is the azimuthal angle (ϕ_0). $b\ cm$ represents the radius of the circle. For the sake of not missing electrically charged monopole, the circle fit is necessary. Besides, when monopole have enough high momentum, the trajectories of monopoles would be a straight line. This could correspond to large parameter b, which means the curvature radius is very large such that the track of particle looks like a straight line.

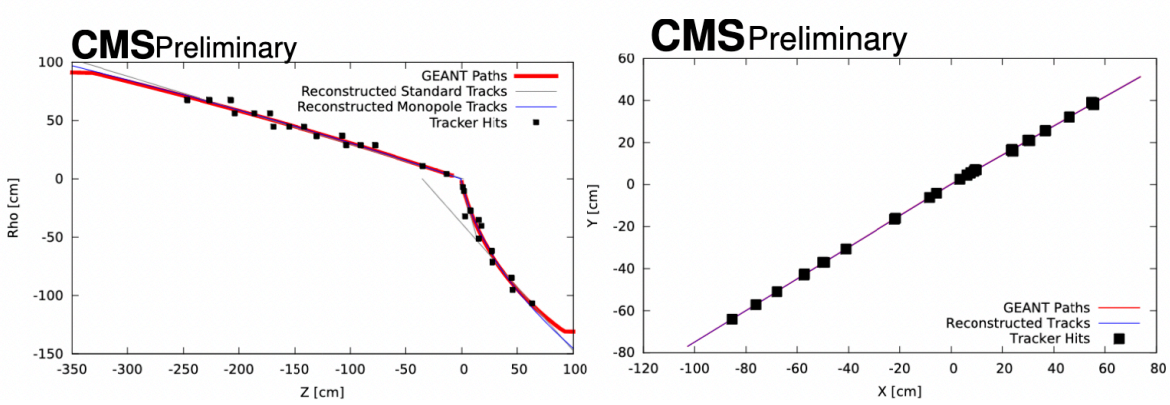

Figure 4.1: Actual and fitted trajectories of monopoles [6].

4.1.2 Track ionization

Owing to the property of high ionized particles, monopole could be measured by the energy loss dE/dx in the tracker. When a high particle with high energy traverses the silicon tracker, the energy loss from the particle excites charge current in the silicon. That is, the energy loss is proportional to the charge collection, so the standard measurement of energy loss is to count the ADC number of collection charges in a hit cluster [27].

doi:10.6342/NTU202300054

However, the monopole is expected to have high sensitivity to the tracker system, causing the fluctuation from lower energy hits (approaching the boundary) that might be added into the tracking reconstruction of the monopole by accident. Instead of measuring the dE/dx, this analysis define a discriminated variable $dE/dx_{Significance}$, which is a combination of total number of strips and the fraction of saturation strips, to distinguish between high ionized monopoles and background (most of them are minimum ionizing). Both saturated strips and unsaturated strips are considered because of detector noise that has a probability to saturate strips, despite the effect being small. The situation of saturation in monopoles is distinct from it, monopole would have saturated strips in reality with some unsaturated strips appearing to be nearby. Thus, the advantage of combining saturated strips and unsaturated strips is to distinguish the signal and background better. Figure 4.2 shows the fraction of strips versus the total number of strips for monopole 2018 MC mass 1000GeV with 2018 blinded data. The fraction of saturation of data is lower than the monopole signal obviously. Besides, the average fraction of saturation for monopole is nearly 0.7, while the saturation probability for the background is about 0.07 by fitting the saturated fraction. Thus, a significant variable $dE/dx_{Significance}$ is developed by using the binomial statistics to estimate the probability of saturated strips occurring randomly, as equation 4.3.

$$dE/dx_{Significance} = \sqrt{-log(BinomialI(0.07, TotalStrips, SaturatedStrips))} \tag{4.3}$$

where BinomialI(p,n,k) represents the binomial probability function that at least k trials out of n independent trials has a probability p to be successful.

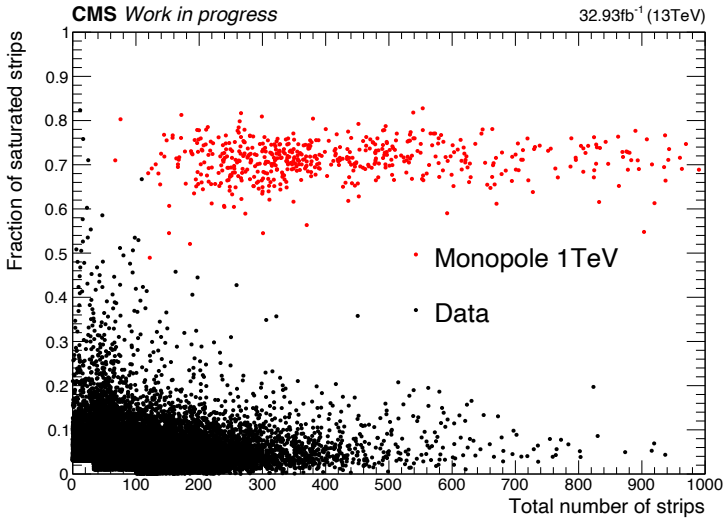

Figure 4.2: The fraction of strips versus total number of strips for monopole 2018 MC mass 1000GeV with 2018 blinded data.

doi:10.6342/NTU202300054

Figure 4.3 compare the distribution of $dE/dx_{Significance}$ for different mass point from 1000 GeV to 4000 GeV with 2018 blinded data. It reflects the significant difference between signal and background, especially the distribution where $dE/dx_{Significance}$ larger than 7. Hence, $dE/dx_{Significance}$ will be used for the tracking discriminated variable for monopole identification.

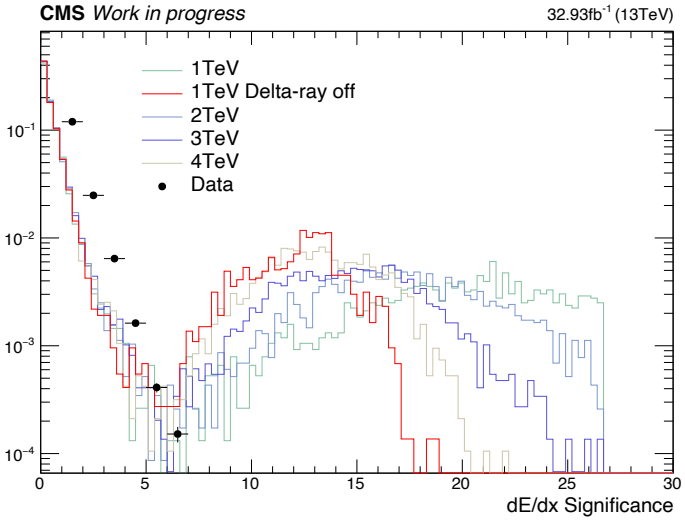

Figure 4.3: The normalized distribution of $dE/dx_{Significance}$ for 2018 signal MC for mass point 1-4 TeV without any selection. The dark blue dot is blinded 2018 data for the comparison.

4.1.3 δ-ray production

The interaction between monopole and matter is one of the most significant uncertainties because monopole is a high ionized particle. When an energetic high ionized particle carrying with high energy travels through the matter, exciting a secondary electron with enough energy to flee away from the main trajectory of the particle for a significant distance. This phenomenon of the secondary electron is called δ-ray production. Therefore, it is worth understanding the effect of δ-ray production from monopole on the $dE/dx_{Significance}$.

The δ-ray production simulation is built in the GEANT4 with only energetic electrons produced. A customize flag for monopole analysis can be switched off to reproduce the MC that without δ-ray production. Despite the that this action might be incompatible with the principle of physics, the δ-ray production would impact the criteria of event selection. Figure 4.3 shows the value of distribution of $dE/dx_{Significance}$ without δ-ray production is lower from the normal distribution, which means that the δ-ray production would affect the signal efficiency. The further discussion and detail information about the systematic uncertainty of signal efficiency of δ-ray production will be introduced in the section 5.6.

doi:10.6342/NTU202300054

4.2 Electromagnetic Calorimeter Cluster Reconstruction

Following the method of finding electrons and photons in the ECAL, we looks into the shower shape of energy deposition and formulate the criteria to reconstruct monopole. However, monopole's charge is equivalent to the charge of about 5000 electrons, it radiates all its kinetic energy over a small distance when encounters the dense crystals in the ECAL. In other words, monopole tends to deposit most energy in one crystal, rather than disperse energy in several crystals as photons and electrons do. This phenomenon makes the shower shape of energy deposition of monopole looks like a high energy "spike" in the ECAL. The current standard algorithm to reconstruct EM particle in SM (e.g. photon and electron) might not be available to reconstruct the monopole. Therefore, we start with the cluster constructed by the "Island algorithm" and the "Hybrid algorithm" to identify the monopole.

The basic idea of Island algorithm [7] is to group the energy deposition into the clusters from a single crystal (seed) that is above a certain threshold and with local maximum energy, as illustrated in figure 4.4. Nevertheless, it is not enough to use the island algorithm alone to reconstruct the transverse energy accurately, especially for the electron, which radiation may spread widely from the main cluster. To recollect the radiation (caused by the particle) falls in other clusters nearby the main cluster, the "super-cluster" is formed by grouping these clusters together by some criteria, such that the transverse energy can be reconstructed accurately, as the illustration in figure 4.5.

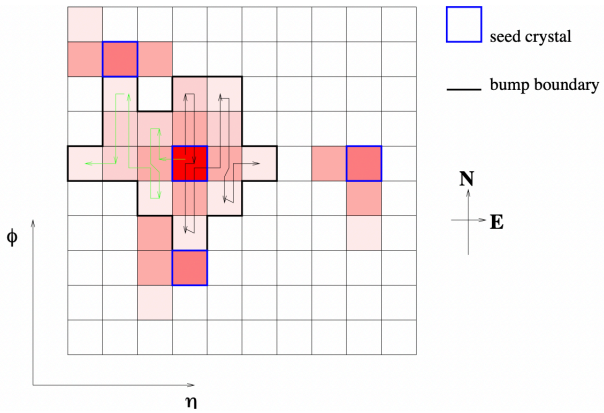

Figure 4.4: A simple illustration (left) of the island algorithm that group the crystals into cluster from "seeds" [7].

The Hybrid algorithm means to reconstruct relatively high energy electrons in the barrel. It targets the clusters ($E_T > 1GeV$) aligned in η with seed crystal "dominoes" of 1×3 crystals or 1×5 (if $E_T^{1\times3} > 1GeV$) in $\phi - \eta$, and scans N steps in ϕ direction to construct the clusters of clusters, analoge to the super-clusters. The dominoes with energy less than 0.1 GeV are eliminated.

doi:10.6342/NTU202300054

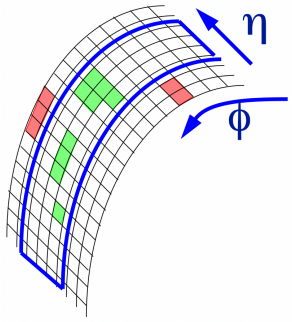

Figure 4.5: The green clusters of radiation from a single electron lie in a very narrow η slice, but spread in ϕ. By combing these clusters altogether (form the super-cluster), it is possible to reconstruct most of the radiated energy [7].

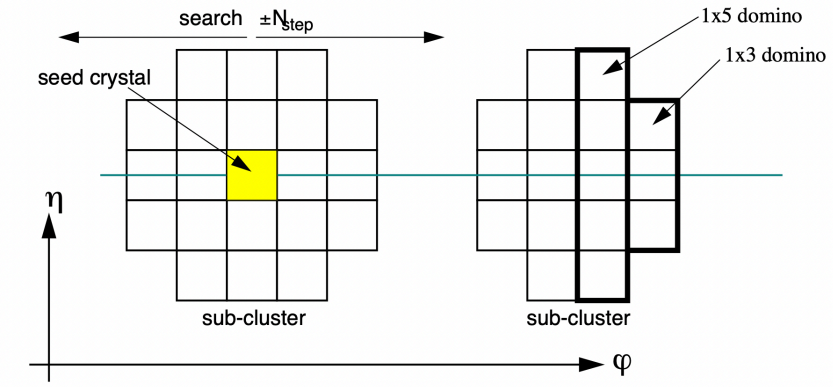

Figure 4.6: The construction step of dominoes by the Hybrid algorithm.[7].

Based on the Island algorithm and Hybrid algorithm, this analysis constructs the clusters of 5×5 ($E_{5\times5}$) with the maximum energy in the crystals to search for the energy deposited by the monopole. Since monopole radiates all energy in a very short distance, it tends to deposit energy almost in one crystal. This makes the ratio of seed crystal energy to the energy in 5×5 crystals approximately equal to 1. Therefore, a topological cluster shape variable f_{51} was employed to identify the monopole. f_{51} is defined as the ratio of the energy deposits aligned in 5×1 ($\eta-\phi$) crystals to the energy deposits in 5×5 crystals, as illustrated in figure 4.7. The comparison of MC and data of f_{51} distribution are shown in figure 4.8.

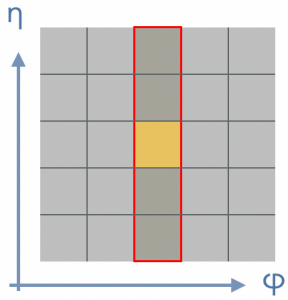

Figure 4.7: The illustration of $f_{51}=\frac{E_{5\times1}}{E_{5\times5}}$. Note that the $E_{5\times1}$ (red frame) constructed from the seed crystal (yellow) is central to the $E_{5\times5}$.

doi:10.6342/NTU202300054

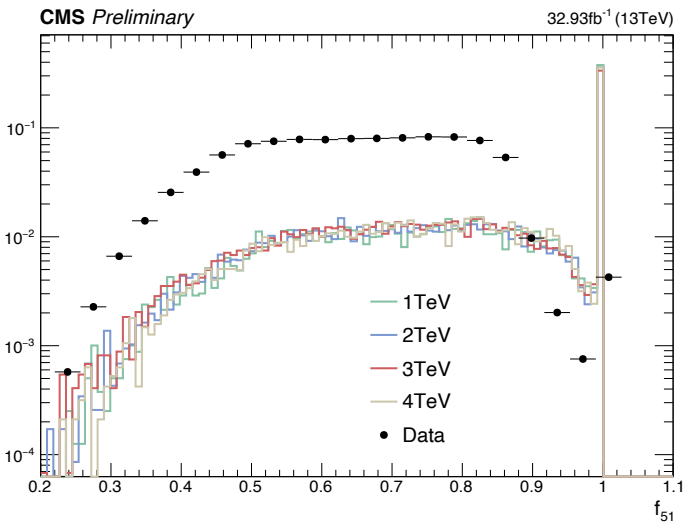

Figure 4.8: The distribution of f_{51} for mass point 1, 2, 3, 4 TeV and the blinded data.

4.3 Hadron calorimeter Isolation

Monopole is expected to deposit most of its energy in the ECAL, with little radiation in the HCAL. The sum of deposited energy in the HCAL near the ECAL cluster center in a radius of an annual 0.1 < R < 0.4 was computed. Figure 4.9 shows the energy deposition in the HCAL of the candidate. There is almost no activity of the candidate cluster is found in the HCAL . Thus, we require the HCAL isolation lesser than 10 GeV.

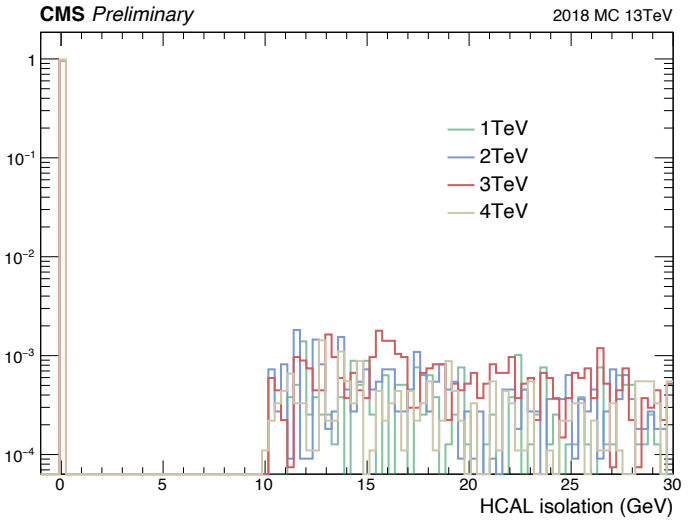

Figure 4.9: The distribution of energy deposition in the HCAL around ECAL cluster of monopole.

doi:10.6342/NTU202300054

doi:10.6342/NTU202300054

Chapter 5 Event Selection

5.1 Trigger Selection

In monopole search, an unprescaled HLT trigger path, "HLT_Photon200_v," for 2017 and 2018, and "HLT_Photon175_v" for 2016 are chosen. This HLT trigger requires at least a photon with transverse momentum larger than 200GeV (175GeV for 2016) to pass with a loose H/E cut (energy in the HCAL over energy in the ECAL).

The reason we choose Photon trigger is that there is no monopole trigger in CMS (unlike ATLAS, they have a suitable trigger for the monopole search [1]). We choose photon trigger since photons have a little similar behavior with the monopoles on the detector, both they have electromagnetism interaction in the detector and stopped by the Ecal. In other words, a monopole looks like a fake photon could fire the photon trigger. The table 5.1 shows the trigger efficiency for each year and mass point. The average of trigger efficiency for HLT_Photon200_v* is around 5% for Run 2.

Mass	2018	2017	2016	2016 APV
m=1000 GeV	4.58	5.01	5.44	5.44
m=1500 GeV	5.10	5.76	6.49	6.26
m=2000 GeV	5.83	5.77	6.59	6.54
m=2500 GeV	6.05	6.28	6.68	6.82
m=3000 GeV	6.59	6.32	6.81	6.89
m=3500 GeV	6.12	6.47	6.48	6.72
m=4000 GeV	5.08	5.19	5.46	5.49
m=4500 GeV	3.52	3.48	3.67	3.41

Table 5.1: Trigger efficiency(%) equals to the event pass trigger selection over total generated events.

The main source for the inefficiency of our signal is the trigger (see table of relative cut) due to the following reasons. First, in physics, the behavior of photon is very different from the monopole. Photons do not leave traces in the detector, while the monopoles

doi:10.6342/NTU202300054

leave significant traces in the Tracker and shifted to the z-component a little by the strong magnetic field. In the photon reconstruction algorithm, photon does not link to the GSF track. Compare to the electron reconstruction algorithm, electron is linked to the accurate track algorithm GSF (called Gaussian-sum filter). Therefore, lack of judgement on the track makes monopole have probability identified as photon.

Second, as explained earlier, the shower shape of deposited clusters in the Ecal for the photons is very different from the monopoles. Photons tend to deposit more than one crystals in the Ecal due to the electromagnetic shower. On the contrary, monopoles tend to deposit on only one crystal, which make it looks like a high energy spike in the ECAL Barrel. Fortunately, even though the shower shape of monopoles is different from the photons, monopole have probability to deposit energy on more than one crystal.

Third, the spike-like signature for monopole lead to monopole killed by the spike killer, which had mentioned in the chapter 3. The spike killer in L1 trigger is unavoidable. It is possible that monopoles are killed before passing through the HLT. Consequently, we can only expect that monopole not only identified as photon in the trigger path "HLT Photon 200", but also not killed by the spike killer in L1 trigger. In this case, we can get the signal events.

To improve the trigger efficiency, trigger study has been done. Some feasible HLT paths have been examined, including double photon trigger and MET trigger. However, the efficiency of the double photon trigger is too low to be considered. The MET trigger presents higher efficiency than the single photon trigger, which will be discussed in the following chapter.

5.2 Monte Carlo and Data sample

The choice of datasets depends on the trigger selection "HLT_Photon200_v*", which is included in the Single Photon or EGamma datesets. Nine datasets with total integrated luminosity of $137 fb^{-1}$ for 2016, 2017 and 2018 have been produced specially for monopole study, as lists in table 5.2 and 5.3.

doi:10.6342/NTU202300054

Table 5.2: 2016 and 2016 APV DataSets - SinglePhoton

DataSets 2016
/SinglePhoton/Run2016F-EXOMONOPOLE-21Feb2020_UL2016-v1/USER
/SinglePhoton/Run2016G-EXOMONOPOLE-21Feb2020_UL2016-v1/USER
/SinglePhoton/Run2016H-EXOMONOPOLE-21Feb2020_UL2016-v1/USER
DataSets 2016 APV
/SinglePhoton/Run2016B-EXOMONOPOLE-21Feb2020_ver1_UL2016_HIPM-v1/USER
/SinglePhoton/Run2016B-EXOMONOPOLE-21Feb2020_ver2_UL2016_HIPM-v1/USER
/SinglePhoton/Run2016C-EXOMONOPOLE-21Feb2020_UL2016_HIPM-v1/USER
/SinglePhoton/Run2016D-EXOMONOPOLE-21Feb2020_UL2016_HIPM-v1/USER
/SinglePhoton/Run2016E-EXOMONOPOLE-21Feb2020_UL2016_HIPM-v1/USER
/SinglePhoton/Run2016F-EXOMONOPOLE-21Feb2020_UL2016_HIPM-v1/USER

Table 5.3: 2017 SinglePhoton and 2018 EGamma DataSets

DataSets 2017 SinglePhoton
/SinglePhoton/Run2017B-EXOMONOPOLE-09Aug2019_UL2017-v1/USER
/SinglePhoton/Run2017C-EXOMONOPOLE-09Aug2019_UL2017-v1/USER
/SinglePhoton/Run2017D-EXOMONOPOLE-09Aug2019_UL2017-v1/USER
/SinglePhoton/Run2017E-EXOMONOPOLE-09Aug2019_UL2017-v1/USER
/SinglePhoton/Run2017F-EXOMONOPOLE-09Aug2019_UL2017-v1/USER
DataSets 2018 EGAMMA
/EGamma/Run2018A-EXOMONOPOLE-12Nov2019_UL2018-v2/USER
/EGamma/Run2018B-EXOMONOPOLE-12Nov2019_UL2018-v2/USER
/EGamma/Run2018C-EXOMONOPOLE-12Nov2019_UL2018-v2/USER
/EGamma/Run2018D-EXOMONOPOLE-12Nov2019_UL2018-v4/USER

doi:10.6342/NTU202300054

5.3 Monpole Identification

As introduced in the previous sections, the monopole reconstructions depends on the track fit parameter, track inozation, and ECAL cluster finding. Furthermore, since monopole candidates are reconstructed from a track to extrapolated the face of ECAL, which is matched to the nearest ECAL cluster, we require that the distance between the monopole track and the extrapolated ECAL cluster to be less than $\Delta R = \sqrt{\phi^2 + \eta^2} < 0.5$. All these characteristic are combined altogether to be our event selection criteria, as shown in table 5.4 for preselection and table 5.5 for discriminating monopole candidates. The full selection cuts criteria are:

Preselection	variable	value
Circular fit parameters	$\|XYpar0\| = sign(c)\sqrt{c^2 - (x-b)^2} - c$	$< 0.6(cm)$
	$\|XYPar2\| = \phi_0 - \arctan\frac{b}{c-a}$	$> 1000(cm)$
Parabola fit parameters	$\|RZpar0\| = z$	$< 10(cm)$
	$\|RZpar1\| = f$	< 999
	$\|RZpar2\| = g$	< 10
Matching variable	$\Delta R = \sqrt{\phi^2 + \eta^2}$	< 0.5
Energy variable	HCAL isolation	$< 10\ GeV$

Table 5.4: Preselection table

Identification selection	variable	value
Trigger selection	HLT_Photon200_v* (2017,2018)	
	HLT_Photon175_v* (2016)	
Energy variable	E_{5x5} (2017,2018)	$> 200\ GeV$
	E_{5x5} (2016)	$> 175\ GeV$
Significant variable	$dE/dx_{significance}$	> 9
	f_{51}	> 0.85

Table 5.5: Discriminated variables cuts table

Note that XYpar0 is the impact parameter when fitting the helical track, and XYpar2 is the radius of the circle from the projection of the helical track. Because the trajectory of energetic monopoles is nearly straight, the radius (XYpar2) of the circular fit of the monopole is expected to be large, especially after the energy $> 200GeV$ cut, most energetic monopoles with a large radius are preserved, while the small radius of candidates that might be not monopole signal are .

doi:10.6342/NTU202300054

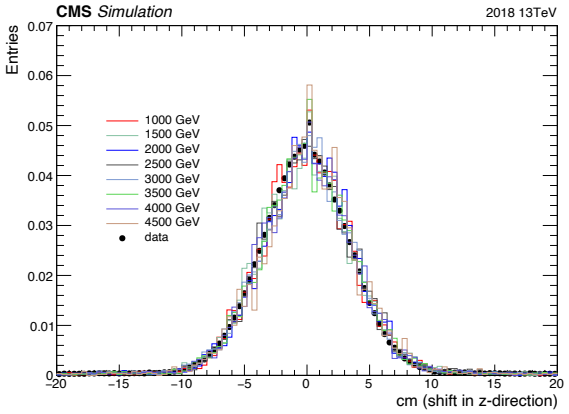

(a) $RZpar0$ displacement in z-direction

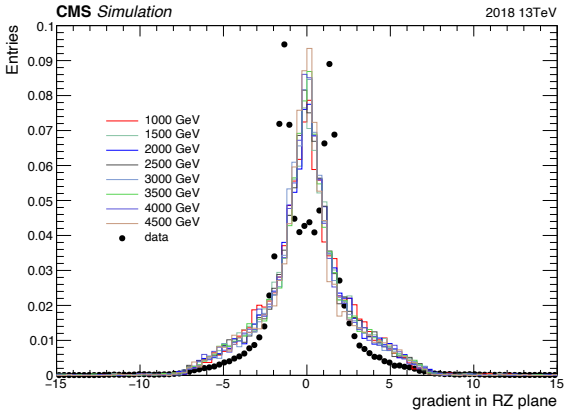

(b) $RZpar1$

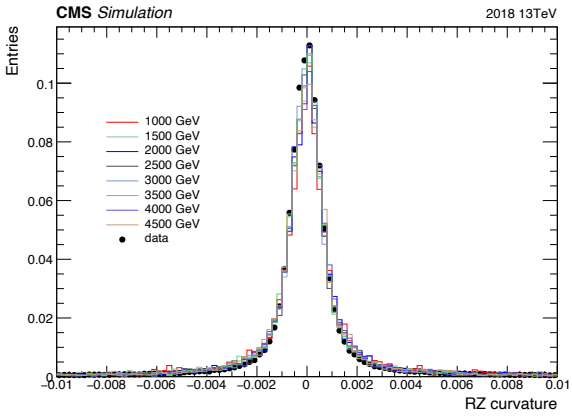

(c) $RZpar2$ (RZ curvature)

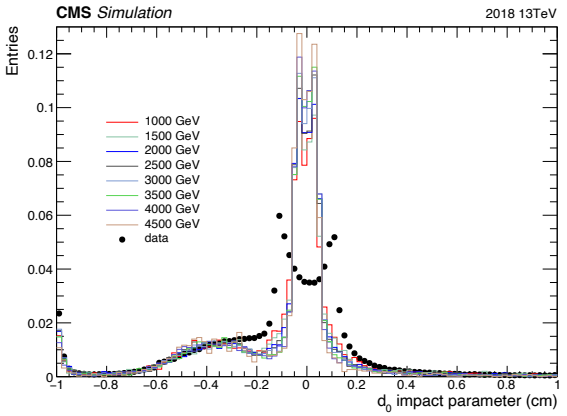

(d) $XYpar0$ (impact parameter)

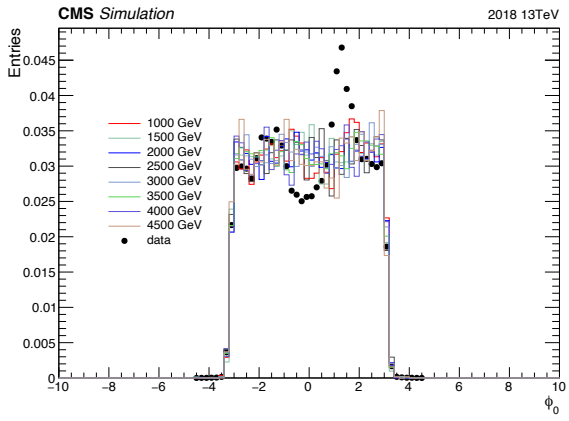

(e) $XYpar1$ (ϕ_0)

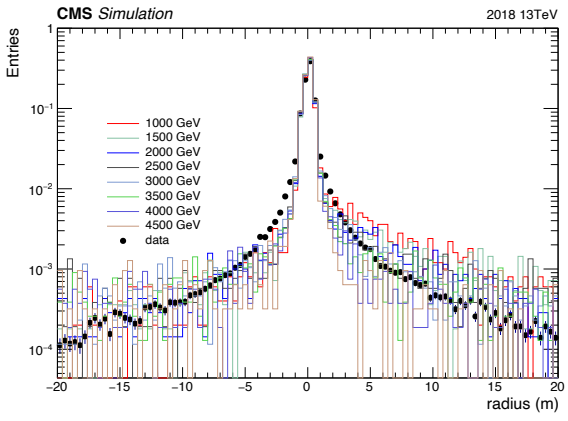

(f) $XYpar2$ (radius of circular fit)

Figure 5.1: The normalized distribution of the parameters of parabola fit in figures 5.1 (a), 5.1 (b), 5.1 (c), and circular fit in figures 5.1 (d), 5.1 (e), 5.1 (f). The color lines correspond to the 2018 MC for each mass points of monopole, while the black points shows the blinded 2018 data $L = xfb^{-1}$ in order to compare the distribution between signal and background.

doi:10.6342/NTU202300054

5.3.1 Pile up sensitivity

The higher pile up (PU) phenomenon that happened in the LHC, which pursues high instantaneous luminosity, could make particle identification that we're interested more difficult, that is, the significant identification variables could be caused by other particles that came from PU rather than monopoles. Thus, it is important to check whether our significant variables (dE/dx_{sig} and f_{51}) are sensitive to PU. The figures 5.2 illustrate the correlations between number of PU vertex and significant variables (dE/dx_{sig} and f_{51}), proving that significant variables are not sensitive to PU.

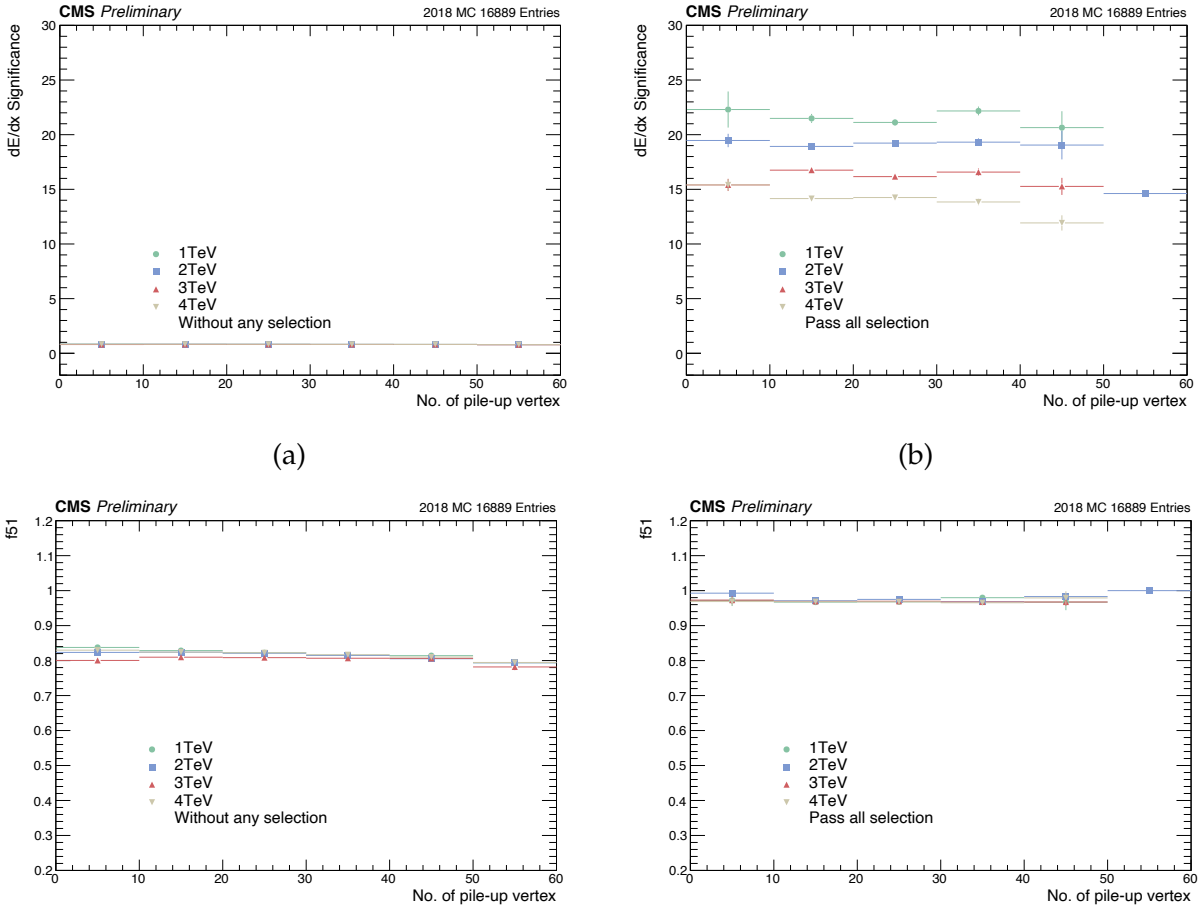

(a) (b)

(c) (d)

Figure 5.2: Profile figures of the comparison of number of PU vertex to dE/dx_{sig} and f_{51} for 2018 mass point 1, 2, 3,and 4TeV. Figure 5.2 (a) and 5.2 (c) are shown without any selection, 5.2 (b) and 5.2 (d) pass all selections mentioned in previous sections. It is obvious to see that dE/dx_{sig} and f_{51} are not sensitive to the PU vertex.

doi:10.6342/NTU202300054

5.4 Signal Efficiency

The signal Monte Carlo sample for full RUN2 for mass point from 1 TeV to 4.5 TeV were generated to study the selection efficiency. In this analysis, the loose preselections, trigger selection and energy cut (which the criteria must be equal or larger than the energy criteria of trigger selection) were applied first. After these cuts, we sort the candidates that pass the cuts in each event with the highest value of dE/dx_{sig}. At last, the tighter selection of dE/dx_{sig} and f_{51} were applied to identify monopole candidates.

The signal efficiency (ϵ_{sig}) is defined as 5.1:

$$\epsilon_{sig} = \frac{number\ of\ events\ after\ the\ selections\ applied}{number\ of\ generated\ events} \tag{5.1}$$

Tables 5.6, A.2, A.3, and A.4 summurized the yield after the successive selection cuts and signal efficiency for each mass point for full RUN2. The overall signal efficiency is about 1% to 2%. The dominant inefficiency of signal efficiency is the trigger (about 4% to 5%) due to the spike-killer as mentioned in the section 5.1.

Notice that we sort the candidates when cutting on f_{51} and dE/dx_{sig} in order to make the treatment consistent with background estimation. Thus, the yields after f_{51} dropped about 50% to 60%. This can be shown in relative efficiency which is defined as

$$\epsilon_{rel} = \frac{number\ of\ events\ after\ selections}{number\ of\ events\ of\ the\ previous\ selection} \tag{5.2}$$

for each selections. The overall relative efficiency for each years are provided in Tables 5.7, A.5, A.6, and A.7).

Mass point (GeV)	1000	1500	2000	2500	3000	3500	4000	4500
generated event	16889	16500	17629	12000	19249	19500	19500	18503
trigger	773	841	1028	720	1269	1193	991	652
preselections	759	828	1009	708	1235	1159	948	617
energy (E_{5x5})	684	772	930	628	1054	1004	833	560
f_{51}	368	413	537	329	556	551	467	344
$dE/dx_{significance}$	366	410	531	327	548	535	446	316
signal efficiency (ϵ_{sig})	2.17%	2.48%	3.01%	2.73%	2.85%	2.74%	2.29%	1.71%

Table 5.6: The cut-flow table for 2018 MC simulation for each mass points.

It is worth noting that the signal efficiencies in this study have been improved by about 10%, compared to the previous thesis study in 2016 [6]. The improvement is a result of the modification of the order of the selection cuts in the analysis code. A cut-flow table

doi:10.6342/NTU202300054

Mass point (GeV)	1000	1500	2000	2500	3000	3500	4000	4500
trigger	4.58	5.10	5.83	6.00	6.59	6.12	5.08	3.52
preselections	98.19	98.45	98.15	98.33	97.32	97.15	95.66	94.63
energy (E_{5x5})	90.12	93.24	92.17	88.70	85.34	86.63	87.87	90.76
f_{51}	53.80	53.50	57.74	52.39	52.75	54.88	56.06	61.43
$dE/dx_{significance}$	99.46	99.27	98.88	99.39	98.56	97.10	95.50	91.86

Table 5.7: The relative efficiency(%) table for 2018 MC simulation for each mass points.

in the previous thesis study is given in table 5.8. One can observe that the number of events dropped sharply after the energy cut except for the trigger. This is the result that the candidates were sorted with the highest value of dE/dx_{sig} first, then the selection cuts were executed afterward. However, this method led to a large number of monopole events lose before the selection cuts. Because the events in signal MC contain a pair of monopoles, that is, we can reconstruct two monopoles (one monopole and one anti-monopole) at most in each event. If the sorting happens prior to the selection cuts, the object of selection cuts has only a candidate which carries the highest dE/dx_{sig}. Nevertheless, this one candidate with the highest dE/dx_{sig} could have other variables that cannot pass the selection cuts. On the contrary, the other monopole without the highest dE/dx_{sig} (but still > 9) may pass all selection cuts.

Mass point (GeV)	1000	1500	2000	2500	3000
generated event	100000	41200	98000	92200	98000
trigger	8728	3897	9666	8975	8801
preselections	4501	2003	5016	4751	4709
energy (E_{5x5})	576	279	713	731	675
f_{51}	378	170	470	466	436
$dE/dx_{significance}$	378	170	469	466	436
signal efficiency (ϵ_{sig})	0.38%	0.41%	0.48%	0.50%	0.44%

Table 5.8: The cut-flow table for previous thesis study in 2016 for each mass points [6].

To be explicit, consider the diagram in figure 5.3. The top table shows three candidates in an event that passes the preselections. The lower left table shows the method of event selection before the modification. Due to the sorting prior to the selection cuts, the candidate with the highest dE/dx_{sig} does not pass the selection cut of f_{51}, and thus the event cannot be included as a signal event although it has the monopole in this event. This is the reason why this method has lower signal efficiency. Whereas, the candidates in the lower right table are preserved, and consequently the event is included as a signal event and increases the signal efficiency. Simply to say, the sorting and the cut do not commute to each other.

doi:10.6342/NTU202300054

	$f_{51} > 0.85$	$dE/dx_{sig} > 9$
cand1	0.4	30
cand2	1	21
cand3	0.9	8

1. cut $f_{51} > 0.85$

	$f_{51} > 0.85$	$dE/dx_{sig} > 9$
~~cand1~~	~~0.4~~	~~30~~
cand2 monopole	1	21
cand3	0.9	8

1. cut $f_{51} > 0.85$

	$f_{51} > 0.85$	$dE/dx_{sig} > 9$
~~cand1~~	~~0.4~~	~~30~~
cand2	1	21
cand3	0.9	8

2. cut $dE/dx_{sig} > 9$

	$f_{51} > 0.85$	$dE/dx_{sig} > 9$
~~cand1~~	~~0.4~~	~~30~~
cand2 monopole	1	21
~~cand3~~	~~0.9~~	~~8~~

Figure 5.3: The example tables illustrate the difference between the 2016 method and the current method for event selection.

5.4.1 Truth-matching

To ensure the signal candidates in the reconstructed events are the real monopoles, it is necessary to do truth-matching, that is, the reconstructed events must be matched to the generated monopole from the GEN steps. The truth-matching is carried out employing calculating the distance $\Delta R = \sqrt{\Delta\phi^2 + \Delta\eta^2}$ between the generated monopoles and reconstructed monopoles, as 5.4, we require ΔR to be smaller than 0.15.

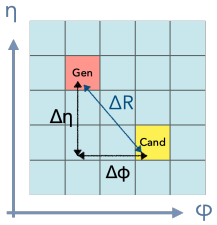

Figure 5.4: The illustration of truth-matching between the reconstructed candidates (Cand) and the generated particles (Gen)

It is helpful to understand the distribution of significant variables of the real monopoles in the reconstruction. The joint distribution of dE/dx_{sig} and f_{51} that pass trigger, preselections, energy selection cut and conditions of truth matching are given in Figures A.18. The figures show that most monopoles do have higher dE/dx_{sig} than the discriminated value 9, Furthermore, the spectrum of f_{51} might be wide, while most monopoles concentrate in the region where f_{51} larger than 0.85 as the yellow dots point out.

doi:10.6342/NTU202300054

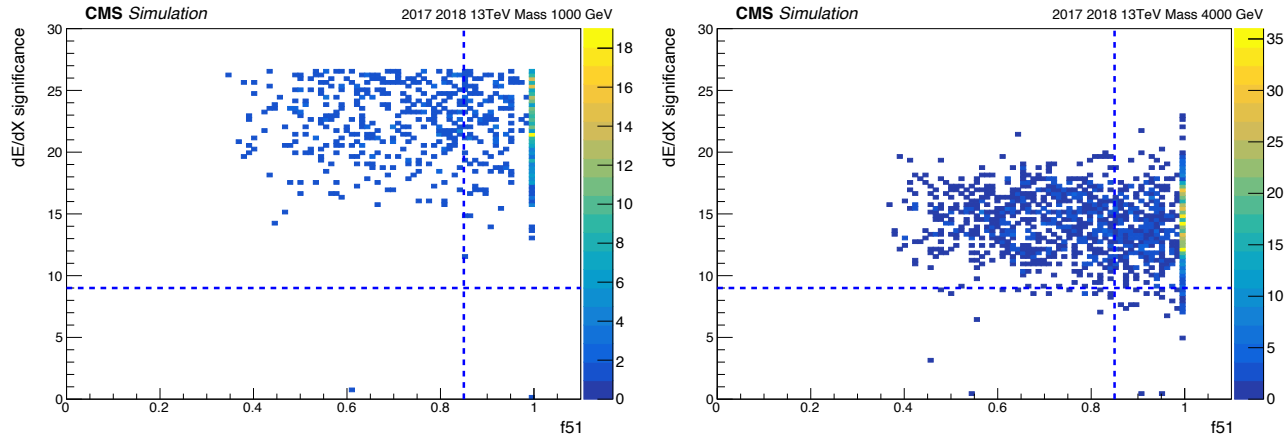

Figure 5.5: The joint distribution of dE/dx_{sig} and f_{51} for 1000 GeV and 4000 GeV after HLT and energy $> 200GeV$ cut for 2018 and 2017 MC. The events are filled once lest the repeat count. The signal region ($dE/dx_{sig} > 9$ and $f_{51} > 0.85$) is distinct from the deep blue dotted lines. The full joint distribution for each mass and each years are attached in Appendix 9.6.

5.5 Background Estimation

In this analysis, the data-driven two-dimensional sideband method, known as ABCD method is used to estimate background. This method requires two independent variables to define one signal region and three control regions. Additionally, the strength of the signal is often small enough to ignore the contribution in the control region. Figure 5.6 illustrates the basic concept of the ABCD method. The region D is the signal region that is distinguished by two independent variables. Region A, B, C are the control region to estimate the background number in region D.

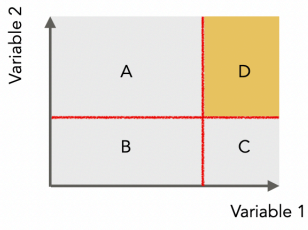

Figure 5.6: ABCD Method

The number of events in the signal region D is estimated by the scaling factor number of events in region A times the number in region C divided by the number in region B, i.e,

$$N_D = \frac{N_A \times N_C}{N_D} \tag{5.3}$$

doi:10.6342/NTU202300054

In this analysis, dEdxSig and f51 which proved to be independent as the profile histogram is shown in 5.7 are used to define the signal region.

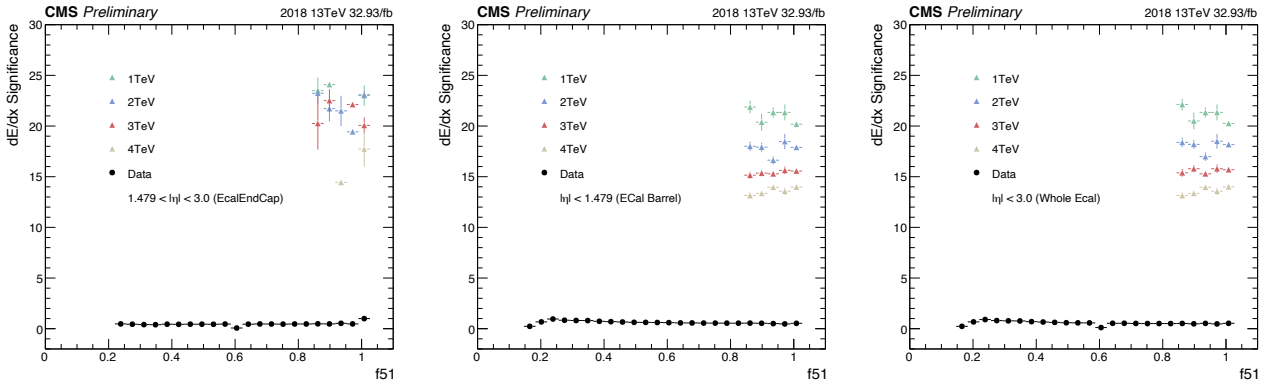

Figure 5.7: Profile histogram of the comparison of dE/dx_{sig} and f_{51} for the ECAL EndCap in the left hand side, Barrel in the center, and full ECAL in the right hand side. The 2018 collision data and MC for mass point 1000 GeV to 4000 GeV are presented in different form and color.

In order to increase the confidence of estimation, we use double ABCD which is divided into 9 regions as illustrated in figure 5.8. Regions 5, 6, and 8 are the cross-check regions distinct by the loose values of independent variables. Region 9 is the signal region discriminated by the tight value which is the final value of the selection cut in the analysis.

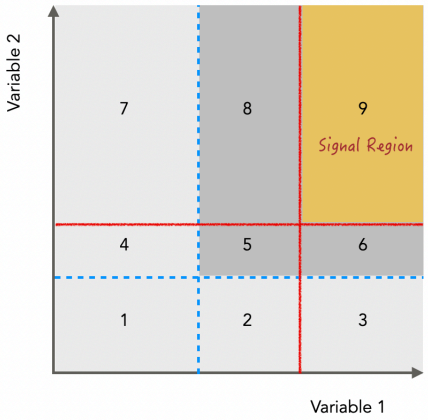

Figure 5.8: double ABCD method

Firstly, regions 5, 6, and 8 are left blind. Using region 1, 2, 3 and 4 to calculate the expected backgrounds in the regions 5, 6 and 8, the calculation are as equation 5.4. Once the expected event number of cross-check regions have good agreement with the actual number in the data, the expected background in the signal region can be calculated as equation 5.5. The loose cut for cross-check were optimized for 2016, and 2017 together with 2018 separately. Consequently, the double ABCD is dominated by the values below:

doi:10.6342/NTU202300054

$$N_5 = \frac{N_2 \times N_4}{N_1}, \quad N_6 = \frac{N_3 \times N_4}{N_1}, \quad N_8 = \frac{N_2 \times N_7}{N_1} \tag{5.4}$$

$$N_9 = \frac{(N_3 + N_6)(N_7 + N_8)}{(N_1 + N_2 + N_4 + N_5)} \tag{5.5}$$

for 2016 and 2016 APV:

$$0 \leq f_{51} \leq 0.6, \quad 0.6 \leq f_{51} \leq 0.85, \quad 0.85 \leq f_{51} \leq 1$$
$$0 \leq dE/dx_{sig} \leq 6.5, \quad 6.5 \leq dE/dx_{sig} \leq 9, \quad 9 \leq dE/dx_{sig} \leq \infty$$

for 2017 and 2018:

$$0 \leq f_{51} \leq 0.75, \quad 0.75 \leq f_{51} \leq 0.85, \quad 0.85 \leq f_{51} \leq 1$$
$$0 \leq dE/dx_{sig} \leq 7, \quad 7 \leq dE/dx_{sig} \leq 9, \quad 9 \leq dE/dx_{sig} \leq \infty$$

The blinded data of LHC collision data used to drive the expected background is shown in Figure 5.9, table 5.9 and table 5.10 lists the counting number in the control regions and cross-check regions, and the expected background number in the cross-check regions and signal regions.

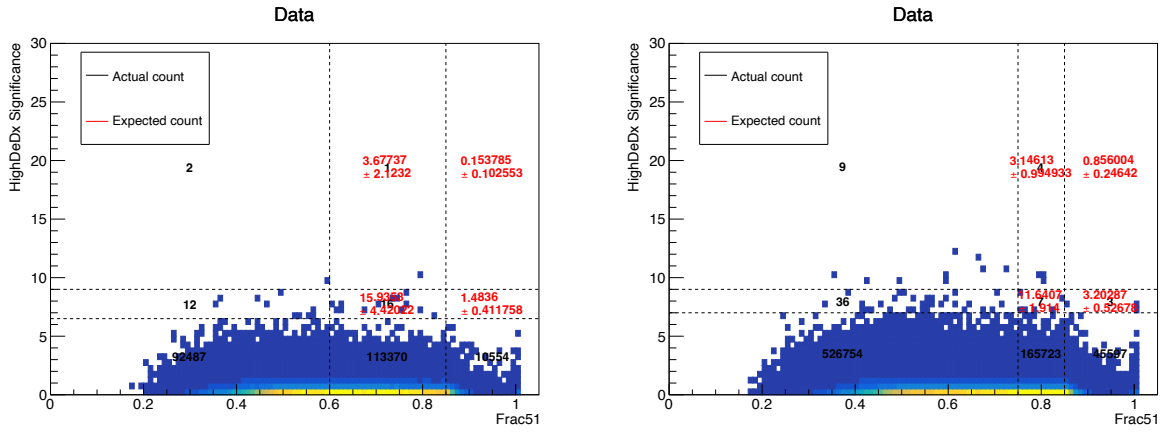

Figure 5.9: The collision data for 2016 with 2016 APV (left) , and 2017 with 2018 (right) in the to estimate the expected background in the signal region. The red number are the expected number and the black number are the actual number observed from the data

doi:10.6342/NTU202300054

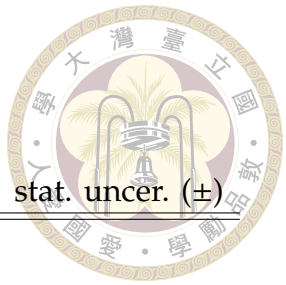

	region	actual	stat. uncer. (±)	expect	stat. uncer. (±)
control region	1	92 487	304.12		
	2	113 370	336.71		
	3	105 54	102.73		
	4	12	3.46		
	7	2	1.41		
cross-check	5	16	4	15.94	4.42
	6	0	0	1.48	0.41
	8	1	1	3.68	2.12
signal region	9			0.21	0.10

Table 5.9: The table shows the actual background counting and the statistical uncertainty (evaluated by the Poisson errors) in the control region (1, 2, 3, 4,7) full 2016 and 2016APV dataset. The expected number in the cross-check (5, 6, 8) are controlled by the loose cut ($f_{51} > 0.6$ and $dEdx_{Sig} > 6.5$), and the significant cut ($f_{51} < 0.85$ and $dEdx_{Sig} < 9$). As long as the expected number and actual number in the cross-check region are almost consistent, the expected background number in the signal region (9) were estimated, while the actual number were blinded temporarily.

	region	actual	stat. uncer. (±)	expect	stat. uncer. (±)
control region	1	526 754	725.78		
	2	165 723	407.10		
	3	45 597	213.54		
	4	36	6		
	7	9	3		
cross-check	5	7	2.65	11.64	1.91
	6	3	1.73	3.20	0.53
	8	4	2	3.15	0.99
signal region	9			0.92	0.25

Table 5.10: The table shows the actual background counting and the statistical uncertainty for full 2017 and 2018 dataset. The expected number in the cross-check (5, 6, 8) are controlled by the loose cut ($f_{51} > 0.75$ and $dEdx_{Sig} > 7$), and the significant cut ($f_{51} < 0.85$ and $dEdx_{Sig} < 9$). The expected background number in the signal region (9) were estimated as the previous table, while the actual number were blinded temporarily.

doi:10.6342/NTU202300054

5.6 Systematic Uncertainty

The cause of systematic uncertainty are related to nature of the measurement apparatus, assumptions made by the experimenter, or the model used to make inferences based on the observed data [28]. Systematic uncertainties could affect the accuracy of the simulation and leads to the simulation describing the data imperfectly. Several kinds of systematic uncertainty were considered, including δ-ray production, dE/dx cross-talk in the tracker subdetector, data-driven background estimation, and integrated luminosity. The MC sample for the study of systematic uncertainty for each mass point for full Run2 has been generated. The following section will discuss how the systematic uncertainties were studied and how the values were determined.

5.6.1 δ-ray production

The δ-ray production from monopole has discussed in section 4.1.3. The δ-ray production could affect our signal because monopoles are high ionized particles. The loss of energy from the δ-ray could add to the monopole' s energy loss so that affect the measurement of dE/dx Significance in the Tracker, the energy loss and shower shape in the ECAL.

Thus, the strategy to see the systematic effect on the δ-ray production is to switch off the δ-ray production parameter in the simulation step (The customize flag "Process.g4SimHits.Physics.MonopoleDeltaRay = cms.untracked.bool(False)") and reproduce the MC sample. For each mass for full Run 2 sample, the physical condition (except the δ-ray production) same as the default MC sample was fully simulated. The signal efficiency are then recomputed to evaluated the systematic uncertainties as tabel 5.11. The systematic uncertainties of δ-ray production is about 9% to 20% for each mass point. Such high uncertainty result from the property of high ionization of monopole will be quoted into the total systematcic uncertainty.

5.6.2 ECAL systematic uncertainty

The systematic uncertainty of ECAL is vital since monopoles stop in the ECAL while having different behavior from the particle in SM. One main systematic effect results from delta-ray production, and the other is the spike topologies algorithm. The calibration effect on systematic uncertainty is negligible. The reasons are as follows. The energy selection cut is above 175GeV, such high threshold of energy cut rejects Ecal Noise. Furthermore, the simulation shows that the energy spectrum of monopole observed in 5x5 ECAL clusters is

doi:10.6342/NTU202300054

	2018	2017	2016	2016APV
1000	14.71	20.21	1.56	-2.46
1500	14.24	11.43	10.71	6.00
2000	11.16	11.47	10.48	-1.08
2500	6.86	0.18	7.79	-4.20
3000	6.25	4.70	9.03	0.48
3500	5.99	9.81	5.53	1.12
4000	-11.26	0.48	7.12	-12.93
4500	-9.10	-6.07	7.29	-18.13

Table 5.11: The systematic uncertainty (%) calculated as (normal efficiency - efficiency without δ-ray production)/ normal efficiency after disabling the delta-ray production in the simulation.

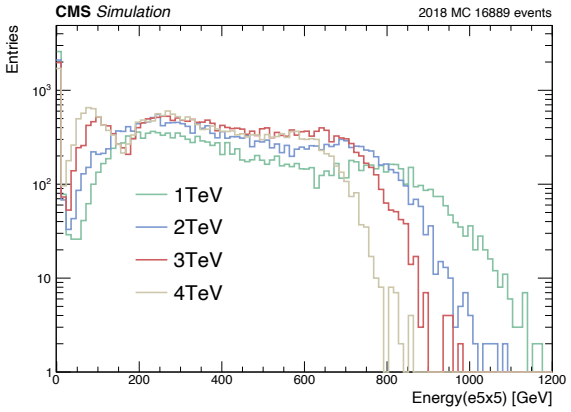

Figure 5.10: The distribution of energy measured in 5x5 clusters before any selection and matched to the generated monopole. The different mass points are represented by different color.

broad as Figure 5.10. The distribution of the energy spectrum of the monopole is broad from low energy up to 1200GeV. These suggest that the systematic effect for calibration is negligible.

5.6.3 dE/dx cross-talk in the Tracker subdetector

The measurement of dE/dx can be affected by the electronic crosstalk, especially monopole is expected to saturate the strips in the Tracker. Hence, we slightly overestimate the crosstalk by 10% to see the systematic uncertainties of the dE/dx cross-talk. The systematic uncertainty of dE/dx cross-talk is found to be very small with the amount of 0.10%. The details are described below.

The cross-talk is a kind of electronic noise that couples between neighboring strips. Through parametrization to model the dE/dx cross-talk effect. The figure 5.11 illustrates a

doi:10.6342/NTU202300054

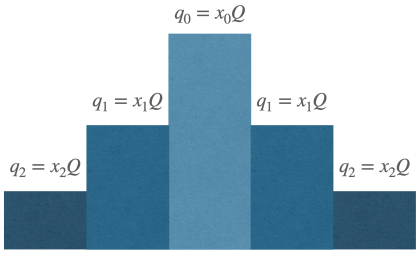

Figure 5.11: Diagram of parametrization of dE/dx cross-talk. For the charge conservation, the crosstalk must satisfy $x_0 + x_1 \times 2 + x_2 \times 2 = Q$.

central strip that a particle travels through is coupled to two neighboring strips as well as the outer two strips. The total induced charge in these strips is modeled as parameter Q. The main strip has a contribution of $x_0 \times Q$, the neighboring strips account for $x_1 \times Q$ and the outer strips is $x_2 \times Q$. For the charge conservation, the crosstalk must satisfy $x_0 + x_1 \times 2 + x_2 \times 2 = Q$. The crosstalk parameters x_0, x_1 and x_2 for four Barrel silicon strips have been measured for both Run I and Run II. To make the simulation have well performance, new measurement parameters have been introduced to the simulation [29].

In order to perform the systematic uncertainty, we remained x_2 unchanged, while change x_0 with up or down 10% of the default values from the configuration file (SimGeneral/MixingModule/python/SiStripSimParameters_cfi.py). In this configuration file, there are 14 command lines for tracker system TIB, TOB, TID, and TEC needed to be changed, such as:

$$CouplingConstantRunIIDecIB2 = cms.vdouble(x_0, x_1, x_2)$$

After compiling with the changed configuration file, the simulation MC was reproduced and the efficiency of the quality selection cut can be recomputed.

5.6.4 Systematic Uncertainty in Data-driven Background Estimation

The uncertainty from background estimation is determined by the statistical uncertainty divided by the expected number in the signal region (see table 5.9 and table 5.10) . That is, the uncertainty is $0.10/0.21 = 0.48$ for 2016, and $0.25/0.92 = 0.27$ for 2017 and 2018. Therefore, the total uncertainty for background estimation is 0.55.

5.6.5 Systematic Uncertainty on the Integrated Luminosity

The integrated luminosity is 2.5%, 2.3% and 2.5% for 2016, 2017 and 2018 respectively which were determined by CMS Luminosity Measurements [30]-[31].

doi:10.6342/NTU202300054

Chapter 6 Trigger Study

The analysis attempts to improve the trigger efficiency by seeking another trigger. The main target that is suitable for searching for monopoles is the MET trigger since it is conjectured that the failure to reconstruct the monopole candidate could lead to large missing transverse momentum. Table 6.1 lists unprescaled triggers that had been tested and their trigger efficiency.

Despite the fact that the second and the fifth MET trigger have higher trigger efficiency, they are not suitable for this analysis because they relate to HCAL, while the monopoles only stop in ECAL. Thus, the result shows that HLT_PFMET200_HBHE_BeamHaloCleaned_v might be the best selection. It is worthy to understand the behavior between MET and monopole, in order to demonstrate the conjecture before applying the MET trigger.

6.1 MET trigger

In the CMS experiment, MET (Missing transverse energy) is defined as the negative sum of the momentum of particles in every direction (missing $\overrightarrow{E}_T = -\Sigma\overrightarrow{p_T}$). The cause of MET results from some undetectable matters violating the conservation of momentum in the detector. MET can be divided into CaloMET and PFMET, where the previous one is the sum of transverse momentum from energies contained in calorimeter towers, and the latter one is reconstructed by using Particle-Flow (PF) algorithm [32] to calculate the sum of transverse momentum of PF [33].

unprescaled trigger	trigger efficiency
HLT_Photon200_v	4.58
HLT_PFMET140_PFMHT140_IDTight_v	20.86
HLT_PFMET250_HBHECleaned_v	12.68
HLT_PFMET200_HBHE_BeamHaloCleaned_v	17.06
HLT_PFMETTypeOne200_HBHE_BeamHaloCleaned_v	18.99
HLT_CaloMET300_HBHECleaned_v	8.49

Table 6.1: Table of MET trigger efficiency (%) for mass point 1000 GeV for 2018 MC sample.

doi:10.6342/NTU202300054

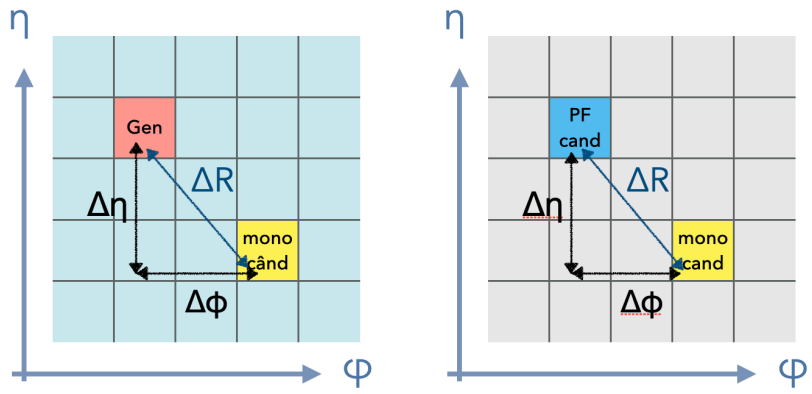

Figure 6.1

Although CaloMET may coincide with the original conjecture that the failure of the trigger to see one of the two monopoles produced leads to a large MET, the efficiency of the CaloMET trigger is very low (maybe due to the spike killer still there), and thus we ignored CaloMET trigger temporarily and focused on the PFMET trigger.

The definition of PFMET makes clear that monopoles must be identified as PF candidates so that they could be counted in the PF algorithm. If one of the monopoles is not identified as any PF candidate, it would not be counted into PFMET, and cause a large MET. In other words, if one of the monopoles is a fake PF candidate (they all are SM particles), while the other flees from the PF algorithm, then the large MET is produced and events are fired by a PFMET trigger with a specific threshold.

6.2 Monopole as PF candidates

Generally, a reconstructed monopole is defined as a particle candidate that passes the selection cuts. However, the selection cut to identify reconstructed monopole is different from the selection cut that was used in the Photon trigger (see chapter 5). Loose selection cuts in Table 6.2 are applied to identify the monopole in the trigger study.

To know the efficiency of the monopole that is identified as a PF candidate, the reconstructed monopole is matched to generated monopole first to ensure the reconstructed monopole is a real monopole. Secondly, the reconstructed monopole is matched to the PF candidates to see whether monopoles correspond to any PF candidate. Figure 6.1 visualized the matching method of PF candidate to reconstructed monopole and generated monopole to reconstructed monopole. The matching condition requires that the distance between two particles is smaller than 0.15. Note that the energy of PF candidates that are used to match

doi:10.6342/NTU202300054

reconstructed monopole is above 50 GeV for convenience.

selection cut	values
preselection	same as Table 5.4
Energy cut (E_{5x5})	$> 50\ GeV$
dE/dx_{sig}	> 9

Table 6.2: Table of reconstructed monopole selection cut

6.2.1 Category

As mentioned, if one of the monopoles is not identified as a PF candidate, it could not be counted into the total transverse momentum of PF, and cause the large MET. For convenience, a reconstructed monopole, which is confirmed to be a real monopole, is identified as any kind of PF candidate called a PF-like monopole. In contrast, a monopole that is not identified as a PF candidate but is a real monopole, we call a reconstructed monopole.

Besides, events may reconstruct one or two monopoles (i.e. monopole and anti-monopole), that is, it is possible that only one or two monopoles are identified as PF candidates (PF-like monopoles). Therefore, we can categorize different cases with the expected magnitude of MET as table 6.3.

Based on the combination and the expected magnitude of MET, PF-like monopoles correspond to which type of particle versus the mean value of MET for different cases are plotted in figure 6.2 by using 2018 MC sample for mass point 1000 GeV. The average MET value in the y-axis is calculated by the PF algorithm for each event. The x-axis represents the particle identification (PID) of the PF candidate, where PID is listed in Table 6.3. Notice that the larger error bar or zero error bar shows that fewer or only one PF-like monopole identified as that type of PF candidate is. For instance, the error bar for the muon case (PID=3) in figure 6.2 (a) is zero, which means that only one PF-like monopole is identified as muon by the PF algorithm. Likewise, the error bar for the muon case (PID=3) in figure 6.2 (c) is large, meaning that few PF-like monopoles are identified as the muon. On the contrary, if the error bar is smaller, more PF-like monopoles are identified as that kind of PF candidate.

no. of monopole	combination	expected MET
2	1 PF-like monopole + 1 reconstructed monopole	large
2	1 PF-like monopole + 1 PF-like monopole	small
1	1 PF-like monopole	large

Table 6.3: Combination of PF-like monopole and reconstructed monopole. The event contains one to two monopoles that can be reconstructed due to the monopole-antimonopole pair production.

doi:10.6342/NTU202300054

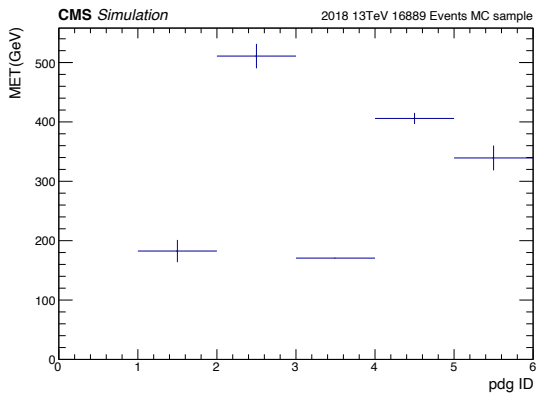

(a) Case 1: 1 PF-like mono. + 1 reco. mono.

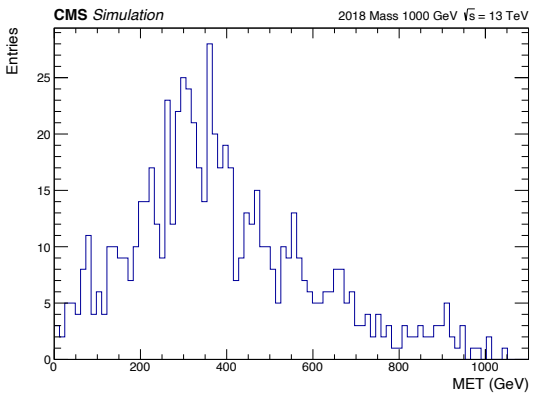

(b) Distribution of MET for case 1

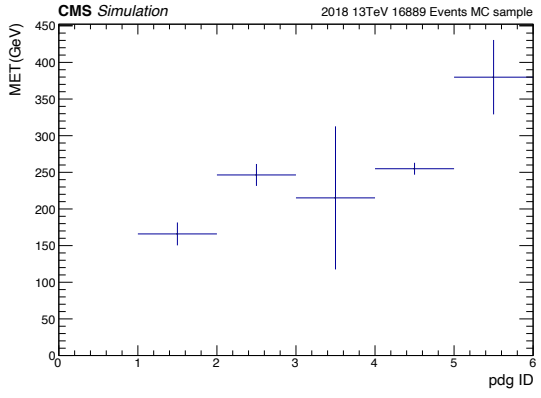

(c) Case 2: 1 PF-like monopole

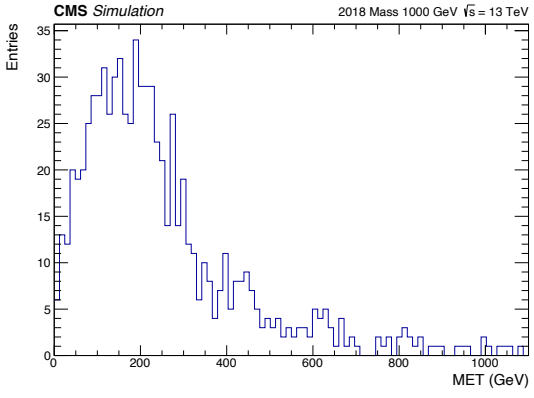

(d) Distribution of MET for case 2

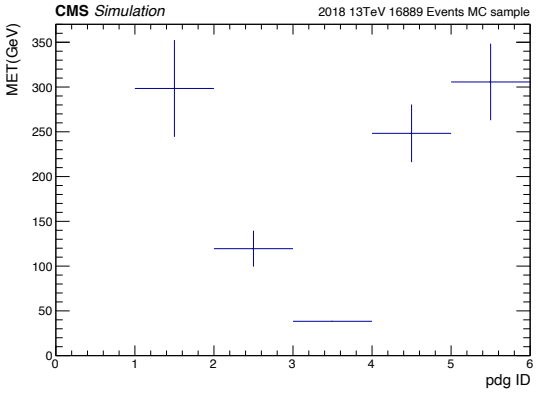

(e) Case 3: 1 PF-like mono. + 1 PF-like mono.

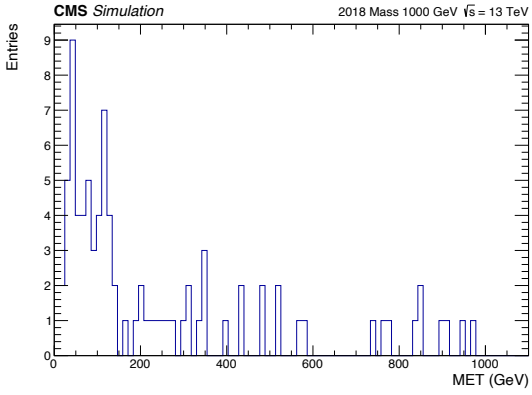

(f) Distribution of MET for case 3

Figure 6.2: Profile diagrams (left column) of PFMET versus the type of PF candidate that a monopole is identified as and distribution of MET for each case (right column). Where the x-axis represents the PID of the PF candidate (PID is listed in Table 6.3), and the y-axis is the average value of the MET. The larger error bar shows that more PF-like monopole identified as that type of PF candidate is.

It is observed that the possibility of identifying monopoles as electron and photon are higher than in other kinds of particles. Because monopole is an electromagnetic particle, same as the electron and photon, which are stopped in the ECAL. Whatever, a monopole could be identified as any kind of PF candidate and be counted into the total momentum

doi:10.6342/NTU202300054

PID	type
0	dummy, unknown
1	charged hadron
2	electron
3	muon
4	photon
5	neutral hadron

Table 6.4: Particle identification (PID) of PF candidates. All of candidates are SM particles

of PF. Furthermore, the calculation of the average for each case based on the distribution of MET in the right column of 6.2 are 390 GeV, 249 GeV, and 244 GeV respectively. For case 1 and case 3, the magnitude of MET is consistent with the expectation, while case 2 is not as large as expected significantly. The possible reasons are the uncertainty from the PF algorithm and the selection cut for the trigger study is not strong enough to identify monopole candidates.

6.3 Conclusion and Future Implementation

At the beginning of this chapter, it is claimed that one of the reconstructed monopoles is not identified as a PF candidate and thus the transverse momentum of the monopole is not calculated into the total transverse momentum of PF, leading to the large PFMET and being fired by the PFMET trigger. The claim was confirmed by studying the behavior between monopole and PFMET by using the 2018 MC sample for mass point 1000 GeV though some uncertainty occurs.

One disadvantage associated with this approach is that it relies on the failure of the trigger to see one of the two monopoles that are produced. On the other hand, we had been shown that the trigger mechanism is different from the Single Photon Trigger, so it is hard to calibrate the correctness of the simulation. Under this circumstance, the overall strategy of the current analysis should be revised according to the mechanism of MET Trigger. However, considering that the MET trigger has higher trigger efficiency than the Photon trigger, future analysis can apply the MET trigger to improve signal efficiency.

In conclusion, the behavior between the reconstructed monopole and MET trigger (mainly PFMET) is understood from this study. The analysis strategy and event selection will not be wholly influenced by applying the MET trigger. Therefore, the datasets that are fired by the MET trigger will be included in this analysis to improve the drawback of the current analysis.

doi:10.6342/NTU202300054

doi:10.6342/NTU202300054

Chapter 7 Physical Result

With the consideration of signal yield, background estimation, and systematic uncertainties presented in chapter 5, the experiment sensitivity can be determined in terms of the upper limit over the cross-section. This chapter will discuss the statistical method used for calculating the experimental sentivity, and present the result in the end.

7.1 Cross-section Limit

Because the data keeps blinded, the expected limit of the cross-section is set in order to investigate the mass range where monopole could occur. The cross section limits are obtained using the frequentist method.

Consider a null hypothesis (H_0) that contains only background b and an alternative hypothesis (H_{s+b}) which includes both background b and signal s. A test statistic for H_0 and H_{s+b} characterized by the likelihood ratio is

$$q = -2\frac{\ln L_{s+b}}{\ln L_b} \tag{7.1}$$

With the greater value of q, the observed data is more like a null hypothesis, and vice versa. The corresponding possibility p_{s+b} and p_b for each hypothesis are denoted by:

$$P(q \geq q_{obs}|s+b) = \int_{q_{obs}}^{\infty} f(q|s+b)dq \tag{7.2}$$

$$P(q \geq q_{obs}|b) = \int_{q_{obs}}^{\infty} f(q|b)dq \tag{7.3}$$

where $f(q|s+b)$ and $f(q|b)$ are the probability density function for H_{s+b} and H_0 respectively. If $1 - p_b < 2.8 \times 10^{-7}$, it indicates that the observation fluctuate to a discovery with 5σ significance in statistics, whereas if $p_{s+b} < 0.05$, it means the exclusion of H_{s+b} at the 95% confidence level.

doi:10.6342/NTU202300054

Mass(GeV)	1000	1500	2000	2500	3000
cross-section(fb)	2.39E-01	1.62E-02	1.46E-03	1.42E-04	1.44E-05

Table 7.1: The theoretical cross-section calculated by MadGraph5 for Drell-Yan spin-1/2 monopole.

Nevertheless, if the experiment is low sensitivity to the signal, it may be influenced by the fluctuation in the expected background. The CL_s method is particularly useful to determine the upper limit in such circumstances. Here we use CL_{s+b} to represent P_{s+b} for the signal + background hypothesis, probability P_b is expressed to be CL_b for null hypothesis, and CL_s is defined as:

$$CL_s = \frac{CL_{s+b}}{CL_b} \tag{7.4}$$

for a 95 % confidence level ($\alpha = 95\%$), the CLs is given by:

$$CL_s = 1 - \alpha = 0.05 \tag{7.5}$$

where CL_s can be intepreted as that the number of signal event is observed at the 95% confidence. However, in the absence of observed event, the expected limit is set by replacing the observed test statistic with the median of the the sampled test statistic from null hypothesis.

7.2 Cross section limits for DY spin-1/2 monopoles

With the help of the Combine Tool provided in the Higgs Group, the preliminary result for the cross-section limit with an integrated luminosity scaled to 137 fb^{-1} at the center of mass of 13 TeV pp-collision data is shown in figure. 7.1.

The theoretical cross-section calculated by Madgraph5 for each mass is listed in table 7.1 and represented as solid line in 7.1. Thus, the corresponding (expected) mass limit is 2320 GeV at 95% confidence level, which can be seen in the vertex of the solid line and the dashed line.

7.3 Sensitivity difference between LHC experiments

The upper limit under the same production model at the center of mass of 13 TeV with an integrated luminosity of 33 fb^{-1} of pp-collision data was set in the CMS experiment in the previous thesis study [6], as shown in figure 7.2. As mentioned, the order of the event

doi:10.6342/NTU202300054

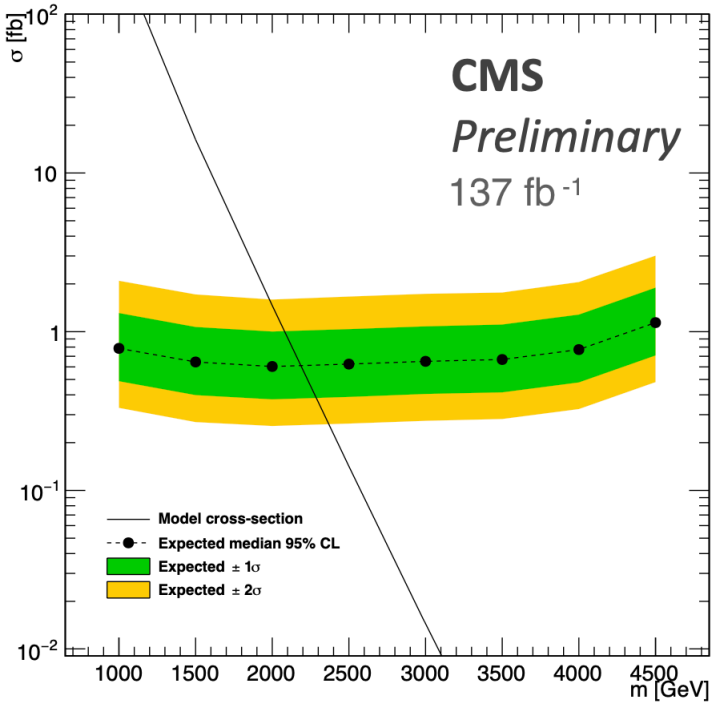

Figure 7.1: The preliminary expected 95% CL upper limits with an integrated luminosity scaled to 137 fb^{-1} on the cross-section for the Drell-Yan spin-1/2 monopole without including the systematic uncertainty.

selection not only leads to low efficiency but also contributes to low sensitivity, especially when the result is compared to the other experiment in LHC – ATLAS experiment.

The ATLAS experiment set an upper limit on the cross-section under the same production model as the CMS experiment by using pp-collision data at the center of mass 13 TeV with an integrated luminosity of 34.4fb^{-1}, which also provided in figure 7.2 [8]. Because the ATLAS experiment had a dedicated trigger for monopole that was based on the high threshold hit capability of the tracker. It was observed that the ATLAS experiment had higher sensitivity in 1 order than that of the previous thesis study.

In this thesis, despite the limitation of the trigger, the improvement of signal efficiency contributes actively to sensitivity. Thus, the sensitivity not only improves an order than that of the previous thesis study but also approaches the result from the ATLAS experiment.

doi:10.6342/NTU202300054

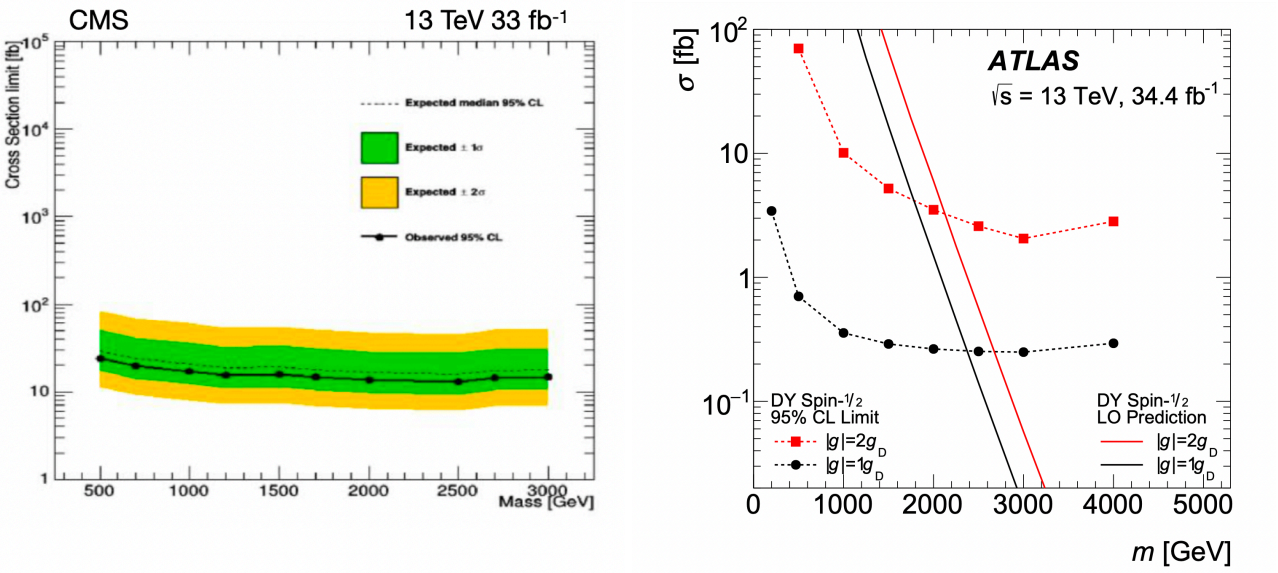

Figure 7.2: Previous thesis study in CMS experiment in the left hand side [6]. ATLAS experiment – the model with black lines corresponds to the same model with the CMS experiment in the right hand side [8].

doi:10.6342/NTU202300054

Chapter 8 Conclusion

This thesis introduced the importance of searching for a magnetic monopole, that is, to explain the quantization of charge and symmetry of electromagnetism. Several theories have opened windows to different properties of a magnetic monopole. In this thesis, we focus on the Dirac monopole with magnetic charge g_D=1 and the accessible mass scale of TeV, which is capable of the LHC.

The signal MC samples are prepared according to the spin-1/2 monopole from the DY process in chapter 3. The simulation shows that the monopole highly ionized the silicon strips in the Tracker, and release most energy in the ECAL, creating an EM shower rapidly and leading to a spike-like topology. The monopole's signature in the CMS detector is visualized by cmsShow which provides a demonstration of the validity of the reconstruction.

Based on the monopole's signature in the CMS detector, the analysis strategy is discussed in chapter 4. This analysis developed two significant variables to identify the reconstructed monopoles, dE/dx_{sig} and f_{51}, which are associated with the Tracker and ECAL respectively. The selection cuts to identify the monopole signal, systematic uncertainty that could affect the signal, and the background estimation in the signal region are discussed in chapter 5. Finally, with these parameters, the upper limits on the production cross section for each mass of spin-1/2 monopoles in the signal region are set. The data in the signal region is left blinded so far.

One of the vital contributions to this study is the improvement of signal efficiency, which benefits the experimental sensitivity. The other is that having acknowledged the limitations of the Photon trigger that drops the wholly signal efficiency, the trigger study in chapter 6 gives a better choice to improve the trigger efficiency – MET trigger. It would be a worthwhile choice to implement the MET trigger in future studies. It is hoped that the more extensive model, such as studying the spin-0 monopole, and $|g| = 2g_D$ monopole for a different spin, can be carried out to deepen the understanding of monopole upon the different model.

doi:10.6342/NTU202300054

doi:10.6342/NTU202300054

Chapter 9 Sensing the earthquake from anomalous radon emissions

9.1 Introduction

Earthquakes' unpredictability and accident are unavoidable natural disasters, especially for Taiwan, which lies between Yangtze Plate to the west and north, the Okinawa Plate to the northeast, and the Philippine Mobile Belt to the east and south, earthquake could be a nightmare for people. Many local seismologists struggle to provide accurate warnings for earthquakes to minimize damage. However, the warning time which measures by the vibration and acceleration of the source of the earthquake is only prior about seconds to the coming earthquake, so it still could not provide people sufficient time to prepare for the coming catastrophe, so earthquake prediction becomes the main issue in seismology.

Several methods for earthquake prediction had been speculated, including the anomalous radioactive radon (^{222}Rn) emissions from the distorted and crack rocks. Radon is a noble gas decaying from radium (^{226}Ra), with a half-life of approximately 3.5 days, thus it can be detected when it is produced from the decay chain. The monitoring of associated anomalous radon emissions near the faults and volcano activities had been surveyed in Taiwan and foreign. Nevertheless, the correlation between anomalous radon emissions and ground motion is unclear in these studies, because the potential background or the fluctuation of the noise from the detector was not noticed.

Therefore, the NTUHEP group developed a detector to collect γ-ray radiated from the radon, placing it in the Hualien weather station, in order to see the correlation between anomalous radon emissions and earthquakes. The crystal detector will be introduced in section 9.2.

Since the detector was deployed in Hualien in April 2021, data collection takes place for more than 500 days. The amount of data is sufficient to study the correlation. This analysis can be divided into two parts: radon data analysis and ground motion study. For

doi:10.6342/NTU202300054

the first part in section 9.3, γ-ray spectrum collected from Hualien for a long period is used to identify the anomalous radon emissions. The second part in section 9.4 is the ground motion study. The earthquake events and seismographic waveform data collected from CWBSN [10] are prepared to study the correlation. Finally, in section 9.5, the statistic method will be discussed, and then present the result of this correlation study.

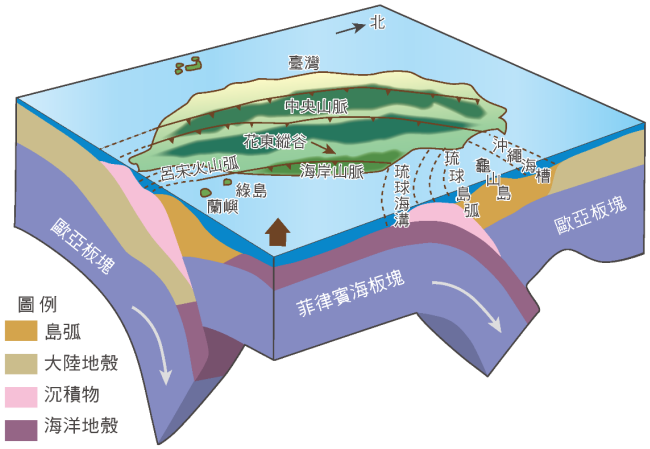

Figure 9.1: The plate junctions in Taiwan.

9.2 Detector

To monitor the anomalous radon emissions, a crystal detector is developed to detect the radiation ($\gamma - ray$) that emits from the radon. The crystal detector that mainly consists of the most widely used scintillation - sodium iodide (NaI), which emits photons when it is subjected to the ionizing radiation, so that the photomultiplier tube coupled with it amplifies the signals, then transmits to the DAQ system, which converts to digital data and read by the controller. Notice that with considering the background noise, a threshold of 0.25 MeV is set to cut off the background during the data acquisition. More detail about the detector is described in [9].

The detector is placed in the basement of Hualien Weather Station, which is subject to a governmental weather report and research facility (CWB) in Taiwan. Earthquakes happen in Hualien frequently because it is in eastern Taiwan, which is above the boundary of the Eurasia Plate and the Philippine Sea Plate. That is the reason why Hualien is one of the best choices for deploying the detector, so it is able to study the correlation between anomalous radon emissions and earthquakes. A system of power supply is also provided so that the developer and manager can monitor the conditions of the detector, and acquire data from the remote terminal.

doi:10.6342/NTU202300054

9.3 Radon data analysis

This section will introduce the content of spectrum collected from Hualien first, then decribe the method to identify the anomalous radon emissions. One of challenging part for this analysis is the energy calibration, which will also be discussed in the end of the section.

9.3.1 γ-ray energy spectrum

A spectrum with around 6.3×10^6 entries collected from Hualien in April 2021 is displayed in figure 9.2. Most entries contained in the spectrum are thermal noises. There are four obvious peaks at 0.30, 0.49, 0.60, 1.45 MeV, and other small bumps distribute in the whole spectrum. According to the decay chain of radon decay chain [34], the peak at 0.30 and 0.60 MeV corresponds to the excited state of ^{214}Pb of 0.295 MeV and ^{214}Bi of 0.609 MeV, and the peak at 0.49 MeV is the Compton scattering from the γ-ray at peak 0.60 MeV. Besides, some bumps decaying from radon is hard to evaluate because they are sensitive to the background fluctuation, so this analysis concentrates on the significant peak radiates from ^{222}Rn.

The peak at 1.45 MeV comes from the decay of ^{40}K because the detector contains some potassium [35]. 10.72% of ^{40}K decays to the excited state of ^{40}Ar, then ^{40}Ar releases γ-ray of 1.460 MeV to go back to ground state. Other 82.28% of ^{40}K decays to calcium-40 (^{40}Ca) with releasing a β particle. The peak 1.45 MeV benefits this analysis to calibrate in-situ the normalization variation caused by thermal effect or system fluctuation, which will be described in the following sections.

In this analysis, the spectrum is counted with 2 hours time binning, and each spectrum contains 50,000 entries.

9.3.2 Data-driven Method

To count the anomalous radon emission, a proper signal and background model are needed. The signal model was simulated by GENAT4. The background model is driven by data collected from the laboratory at NTU. The total probability function is presented in figure 9.3. However, both the signal and background model were not simulated the data perfectly due to some problem with the development [9]. Therefore, the strategy is modified to use a data-driven method to replace the model from the simulation.

Without a proper model, the data-driven method is employed in this analysis. Because

doi:10.6342/NTU202300054

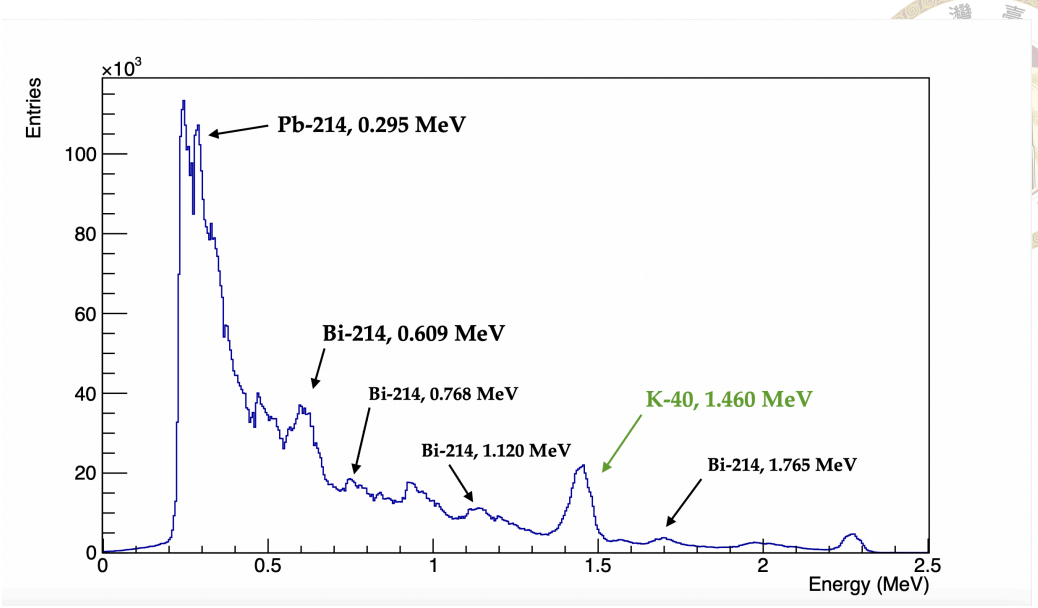

Figure 9.2: Example of energy spectrum (data) collected from Hualien for 10 days in April 2021. The black text arrows represent the radon decay chain.

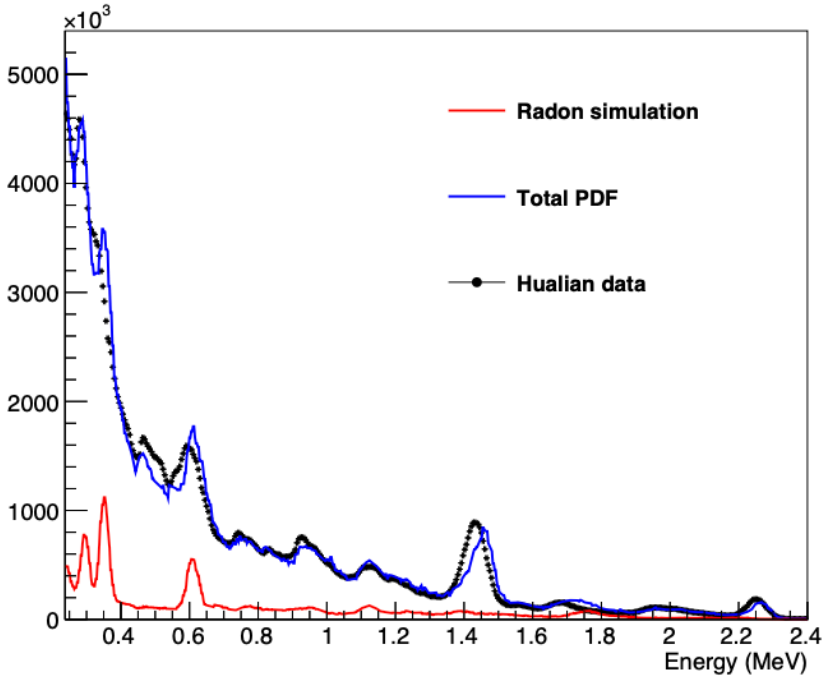

Figure 9.3: Result of template fitting [9]. Data collected from Hualien for 50 days in 2021.

our goal is to identify the anomalous radon emissions, the absolute radon is not important but the radon fluctuation over the average. Firstly, the energy spectrums for a certain period are merged together to form a smooth shape as an Asimov template or reference, as illustrated in figure 9.4. Then use the entries around ^{40}K region (1.2 MeV to 1.5 MeV) to normalize the Asimov shape to data and control the background in the radon region (0.25 MeV to 0.8 MeV).

Secondly, the number of radon for every 2 hours (N_{radon}) subtract the number of radon

doi:10.6342/NTU202300054

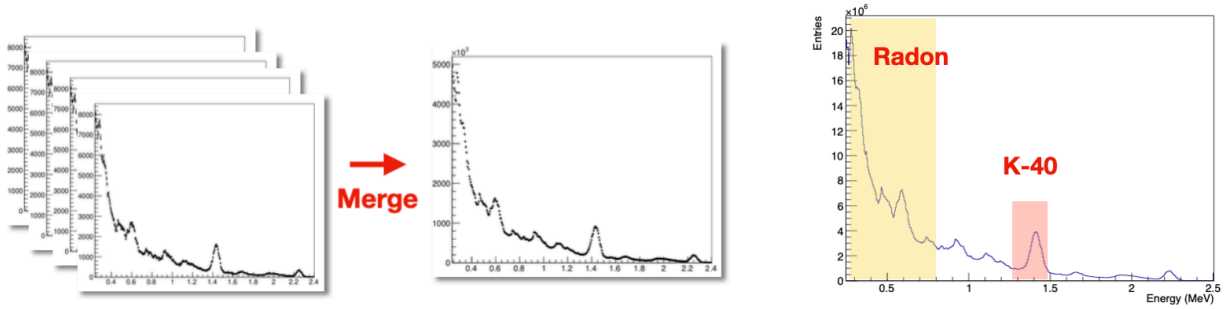

Figure 9.4: Illustration of data-driven like method.

from the normalized template ($\langle N_{radon} \rangle$) to estimate the fluctuated number of radon. The distribution of relative radon decay from September to December 2021 is presented in figure 9.5, where the standard deviation is given by the Gaussian fitting. Notice that the number of radon for every 2 hours larger than that of the template is valuable, we remove the events with $N_{radon} < \langle N_{radon} \rangle$, then it is able to obtain radon fluctuation.

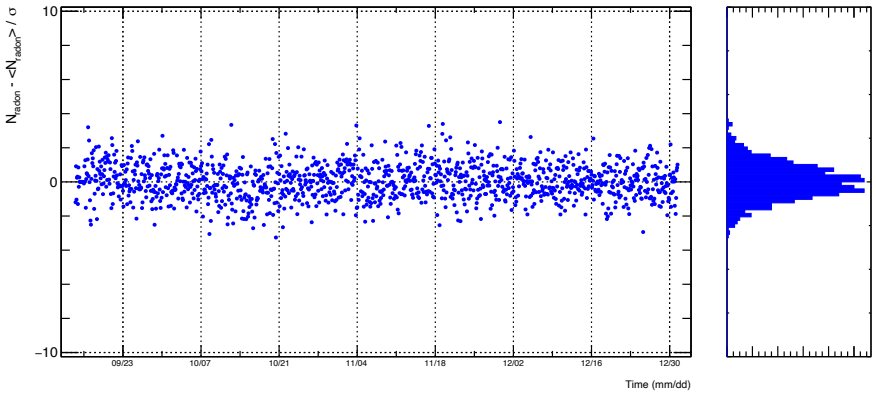

Figure 9.5: Diagram of distribution of relative radon decay ($(N - \langle N \rangle)/\sigma$) from September to December in 2021.

Finally, this analysis adopts p-value to measure the observed incompatibility with the "null hypothesis". The calculation of p-value is shown in equation 9.1, it quantifies the level of consistency between observed data and the null hypothesis. It can be also converted to the number of standard deviations corresponding to a Gaussian distribution, i.e. nσ significance, as equation 9.2 and illustration given in figure 9.6. If the number of significance is at least 4σ, which corresponds to a probability of background fluctuation (p-value) of 1.35×10^{-3}, it can be claimed that anomalous radon emissions are observed.

Moreover, blinded analysis is adopted in this analysis, which temporarily and judiciously removing data labels and altering data values to fight bias and error [36]. After the radon

doi:10.6342/NTU202300054

data is done properly, we can investigate the correlation between anomalous radon emissions and ground motion. The p-value of radon fluctuation from September to December 2021 is presented in figure 9.7.

$$p = \int_z^{\infty} \frac{1}{\sqrt{2\pi}} \exp\left(\frac{x^2}{2}\right) dx = \frac{1}{2}\left[1 - erf\left(\frac{Z}{\sqrt{2}}\right)\right] \tag{9.1}$$

$$Z = \Phi^{-1}(1-p) \tag{9.2}$$

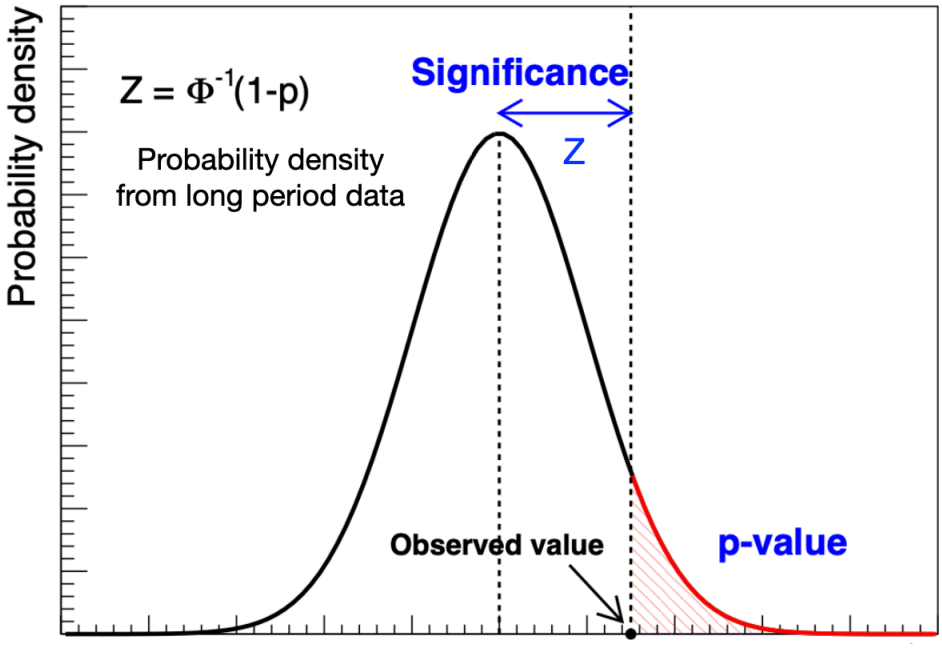

Figure 9.6: The relation between significance and p-value.

9.3.3 Energy Calibration

The data collected from September to December 2021 had been observed that some peak (0.59 MeV, 1.4 MeV, and 2.2 MeV) in the spectrum for each 2 hours is slightly different from the template which made by this period. To calibrate the energy fluctuation, the energy ratio is applied to the spectrum based on an unknown peak at about 2.2 MeV, as equation 9.3. The distribution of C_{factor} is presented in figure **??**. To verify the validation of calibration, the comparison of peak 1.4 MeV (^{40}K) before and after the calibration is given in figure **??**, which can be shown the stability of peak 1.4 MeV (^{40}K). The calibration result of peak 0.59 MeV and peak 2.2 MeV are also given in **??** and **??**.

doi:10.6342/NTU202300054

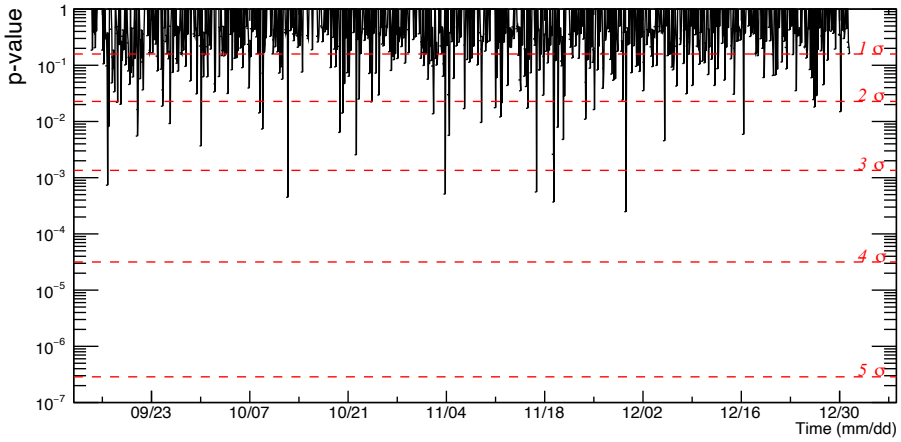

Figure 9.7: Diagram of p-value and its corresponding to # of σ of radon fluctuation from September to December 2021

$$C_{factor} = \frac{peak_{template}}{peak_{2hr}}, \qquad E_{cali} = C_{factor} E_{raw} \tag{9.3}$$

Nevertheless, the data collected from April 2021 to October 2022 is observed to have a tendency for serious shifts and distortion. The comparison of energy spectrums for 2021 and 2022 are displayed in figure 9.9. One can observe that remarkable peaks, such as 1.4 MeV for ^{40}K, 0.59 MeV for radon, and 2.2 MeV, have significant shifts to left. The comparison of peak 1.4 MeV, 0.59 MeV, and 2.2 MeV is displayed in figure 9.10.

It is found that the shift is non-linear, and the degree of shift in high energy is much larger than that of low energy. For example, from May to October 2022, peak ^{222}Rn at 0.62 MeV declined from 0.61 MeV to 0.53 MeV, with a slope of about 0.01. The peak ^{40}K at 1.46 MeV decreased from 1.45 MeV to 1.3 MeV, with a slope of about 0.03. Then for peak 2.26 MeV, dropping with the slope of about 0.4. Therefore, the simple calibration mentioned above becomes invalid.

The shift may attribute to the temperature because the temperature may affect the thermal excitation of the photocathode, leading to low data quality. Figure 9.10 also gives the correlation between specific peak shift and temperature change [37]. It clearly shows that the data quality is much more stable when the temperature decreases, while the full spectrum keeps shifting when the temperature increases. Therefore, the temperature would be key to calibrating the energy spectrum in future studies. In this thesis, the study will rather focus on the stable data from September to December 2021.

doi:10.6342/NTU202300054

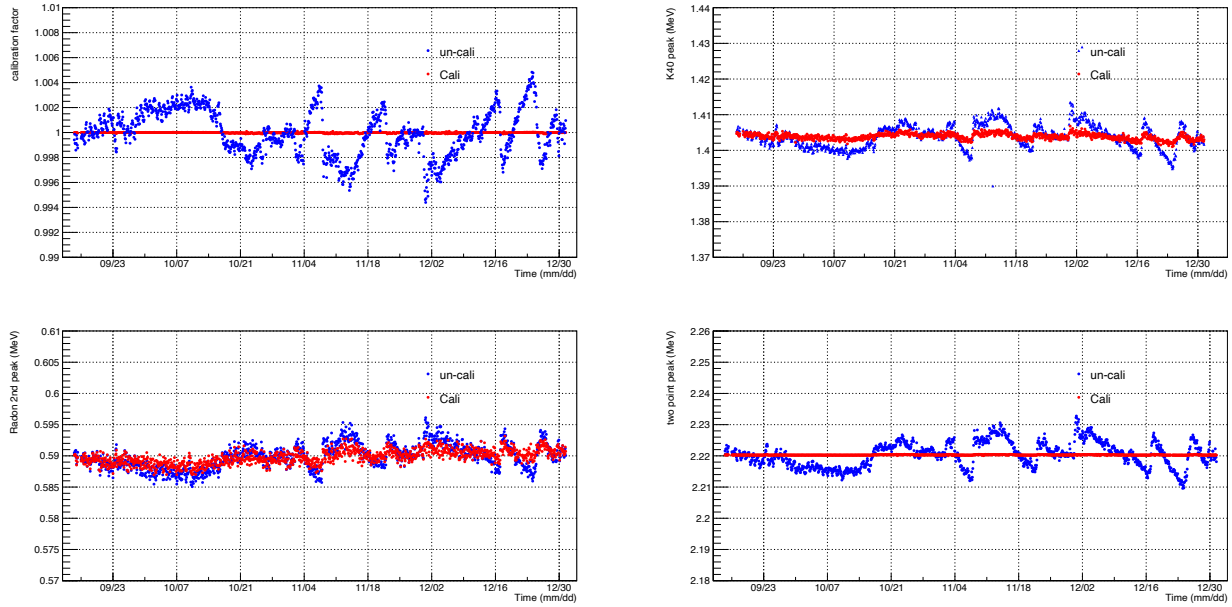

Figure 9.8: Diagram of distribution of calibration factor C_{factor}, peak 1.4 MeV ^{40}K, peak 0.59 MeV (one of radon decay peak), peak 2.2 MeV.

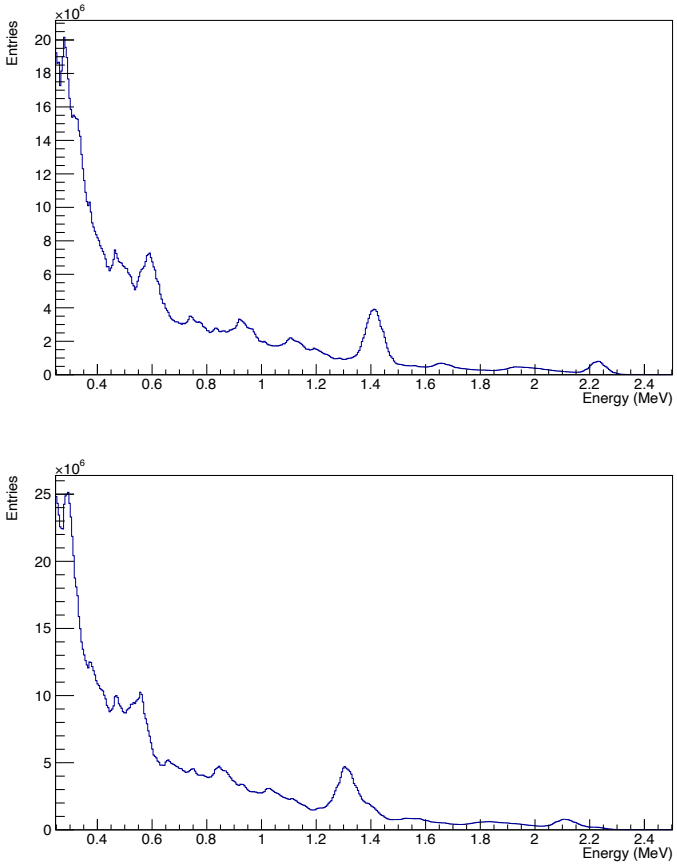

Figure 9.9: Energy spectrum from data collected from April to December 2021 in the upper side, and January to Octorber 2022 in the lower side.

doi:10.6342/NTU202300054

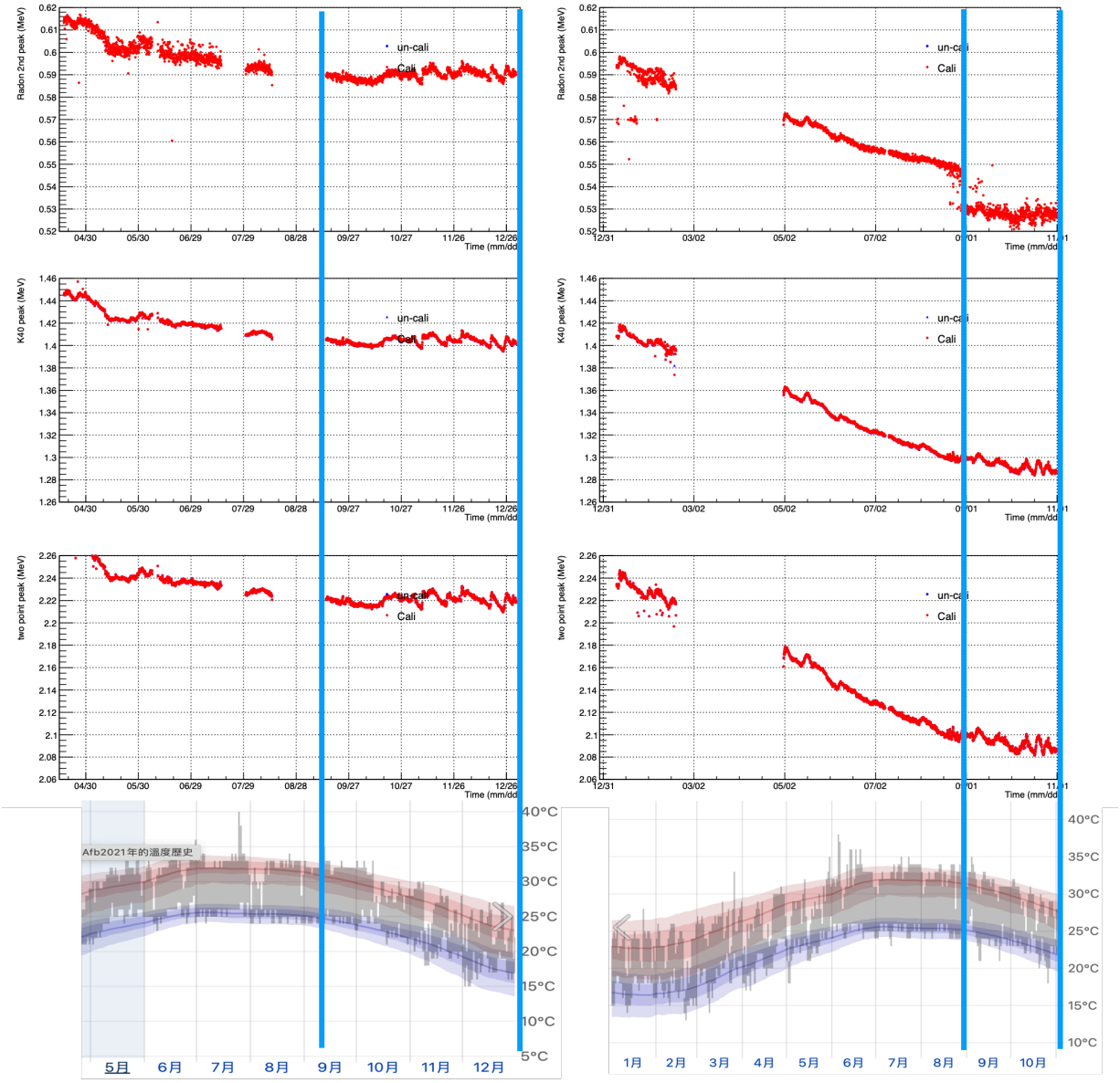

Figure 9.10: Comparison of the whole data collected from May 2021 to October 2022 for peak 0.59 MeV, 1.4 MeV, and 2.2 MeV. Note that the empty bins means we loss connection with the detector or shut-down.

doi:10.6342/NTU202300054

9.4 Seismic data analysis

This analysis collects seismic data from Geophysical Data Management System (GDMS) of CWBSN [10], in order to investigate the correlation between anomalous radon events and earthquakes. This section describes how the earthquake events are collected and how the seismographic data is dealt with to correspond to the radon data.

9.4.1 Earthquakes event catalog

The earthquake events catalog in Taiwan is public and available for download from the GDMS website, which interfaces for download is displayed in figure 9.1. One can select a certain period (Taiwan's timezone: UTC+8) and a certain area, and the Richter magnitude scale M_L and the depth of the earthquake events are acquired. Notice that events that happened only within 35 km from Hualien are selected for this analysis. Since the detector was deployed in the Hualien weather station, it is speculated that the anomalous radon events would not correlate to the earthquake events which happened far away from the Hualien station. Despite this, the conjecture for 35 km is not without problems, it can be discussed further.

9.4.2 Waveform data

Apart from the earthquake events, waveform data from various seismometers were collected, including short-period sensor (EH), broadband sensor (HH), and accelerometer (HN). The waveform data represents the level of ground shaking, and it can retrieve the properties of the hypocenter such as the structure of the earth, while seismographic data itself is not

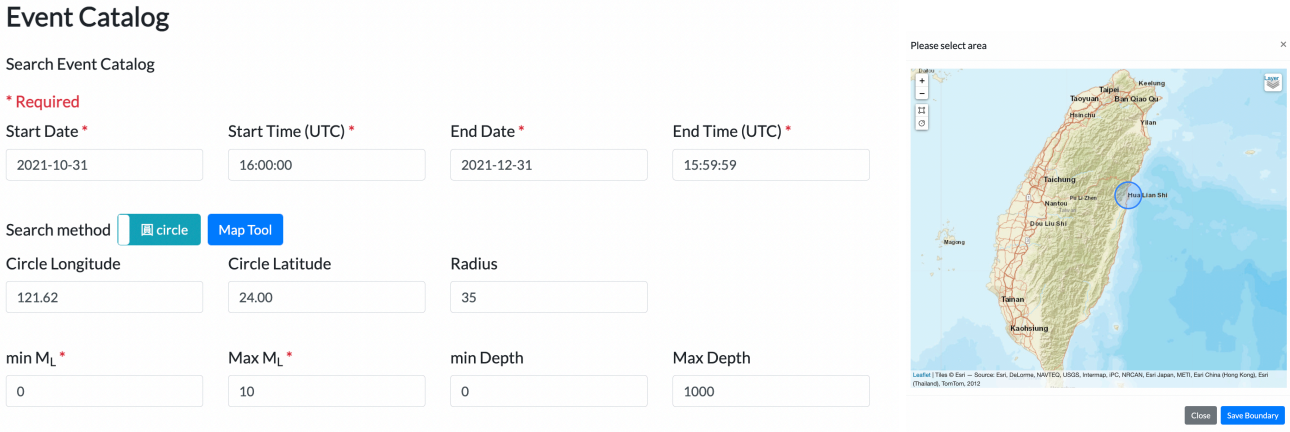

Table 9.1: Screenshots of earthquake event catalog from GDMS.

doi:10.6342/NTU202300054

related to the source hypocenter. Each seismograph provides high sensitivity to different frequencies of earthquakes in different directions (north-south, east-west, vertical). Consequently, this analysis intends to understand the relationship between radon emissions and different kinds of earthquakes. The summary of different seismographs is in the following, and the instruments information is listed in figure 9.11.

- **Short period sensor**

  The short period sensor, a velocity-type seismometer, is highly sensitive to nature frequency (> 1 Hz), so any ground fracture which leads to low-scale earthquakes and microseisms is recorded by the short period sensor. In addition, the high frequency of an earthquake event that is far away from the station decay quickly, on the contrary, the low frequency of an earthquake event which usually causes by larger-scale shaking propagates over a long distance. Thus, a short period sensor reflects the ground motions in a short distance with low high-frequency distortion, while it may be saturated by large earthquakes. The short period sensor is better to study the adjacent ground motion correlation to radon emissions because the detectable range covered by the crystal detector is limited.

- **Broadband sensor**

  The broadband sensor, being a velocity-type seismometer, is sensitive to a broad range of frequency (0.0083Hz 30Hz). It can not only record the weak ground motion, but also records signals for a long period, and thus it can detect an earthquake far from 1000 km from the epicenter.

- **Accelerometer**

  The accelerometer is an acceleration-type seismometer, which records the signal of a large earthquake. It could avoid the saturation of distortion of the vibration.

The waveform data format from GDMS is in miniseed [38], while the most common format in high energy physics is ROOT. To be convenient, the waveform data were converted to ROOT by obspy, which is an open-source project dedicated to providing a Python framework for processing seismological data [39]. Furthermore, the structure of waveform data is different from that of γ-ray data. In radon data analysis, the spectrum is binned for each 2 hours, while the seismographs record event per 0.01 seconds. Since we only need to identify the earthquake event that matching to the anomalous radon event, the high resolution of seismograph data is trifling. Hence, the seismograph data are processed to match the structure to the radon data, i.e., binning waveform data per 2 hours.

doi:10.6342/NTU202300054

Instrument Info

Channel	Location	Latitude	Longitude	Elevation	Depth(m)	Azimuth	Start Time	End Time	Sensor	Constant (m/s/cnt. or m/s^2/cnt.)
EHE	00	23.975100	121.613500	16.00	119.00	90.0	2008-10-15	-	KS-54100	1.100E-10
EHN	00	23.975100	121.613500	16.00	119.00	0.0	2008-10-15	-	KS-54100	1.100E-10
EHZ	00	23.975100	121.613500	16.00	119.00	0.0	2008-10-15	-	KS-54100	1.100E-10
HH1	00	23.975100	121.613500	16.00	294.00	0.0	2008-10-19	-	KS-2000BH	1.430E-9
HH2	00	23.975100	121.613500	16.00	294.00	90.0	2008-10-19	-	KS-2000BH	1.580E-9
HHZ	00	23.975100	121.613500	16.00	294.00	0.0	2008-10-19	-	KS-2000BH	1.450E-9
HN1	00	23.975100	121.613500	16.00	289.00	144.0	2008-10-19	-	PA-23BH	6.440E-6
HN2	00	23.975100	121.613500	16.00	289.00	234.0	2008-10-19	-	PA-23BH	6.460E-6
HNZ	00	23.975100	121.613500	16.00	289.00	0.0	2008-10-19	-	PA-23BH	6.440E-6

Figure 9.11: Table of instruments information from GDMS [10]. The ending letter N (or 1) , E (or 2), and Z represents north-south, east-west, and vertical direction separately. EH: Short period sesnor; HH: Broadband sensor; HN: Accelerometer.

The binning strategy is to select the largest amplitude in waveform data per 2 hours as a bin. Before binning, the waveform data are multiplied to a constant which is provided in the last column of table 9.11, in order to deconvolute the true ground motion and the real physical quantity. Moreover, the baseline shift problem occurs in multiple seismographs. The simplest method is to remove the mean and shift the baseline to zero. The waveform data for each seismograph and direction that have been processed are displayed in figure B.19. There are other challenging problems for the raw waveform data from other periods, including removing instrument responses and severe baseline incline, which should be understood and processed further in future studies.

The procedure of binning is in the following and figure 9.13. The largest (absolute) amplitude in waveform data per 2 hours as a bin and get the cumulative distribution, which would be Gaussian distribution normally. To distinct the large ground motion, the waveform data is expressed in number of standard deviation (σ) with respect to the Gaussian distribution. Such that

doi:10.6342/NTU202300054

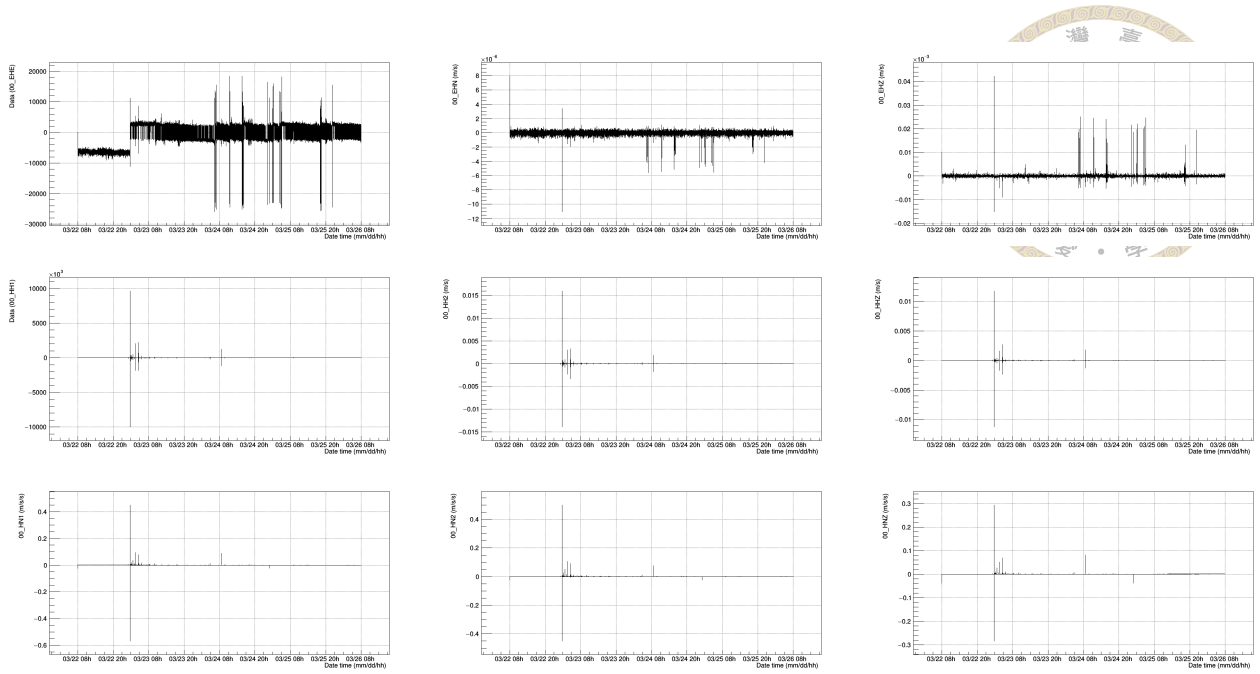

Figure 9.12: Demo of waveform data from the short period sensor (EH*), broadband sensor (HH*), and accelerometer (HN*) from March 23 to 25 in 2022. Note that only the largest amplitude in each 1 second is plotted. A large earthquake with M_L of 6.7 and a depth of 25.7 km happened on March 23 at 1:41 from 65.6 km South of Hualien County.

9.5 Result

The seismological data collection is incomplete due to data loss and which needed to check with the developer in GDMS. Additionally, the radon data exists drawback due to the low DAQ. Only a small amount of data both sides is reliable and feasible for this analysis. Therefore, this thesis select a certain period, i.e. November to December 2021, to study the correlation with anomalous radon emissions. The raw waveform data for this period are displayed in Appendix 9.6.

The preliminary result for the correlation between anomalous radon events and earthquake event is presented in figure 9.14. However, no determined evidence shows that anomalous radon emissions relate to earthquake events. The potential cause is that neither significant anomalous radon events during this period, nor earthquakes that are M_L ≥5. Moreover, an advanced method for quantitative studying correlation is needed.

The relation between anomalous radon events and waveform data from short period sensors and broadband sensors are given in figure 9.15 and 9.16. Since the short period sensor is sensitive to the ground motion nearby the Hualien weather station, the relation should be more accurate than that of the broadband sensor and the earthquake events. It is observed that there is a point around 30th November in EHE (the east-west direction of

doi:10.6342/NTU202300054

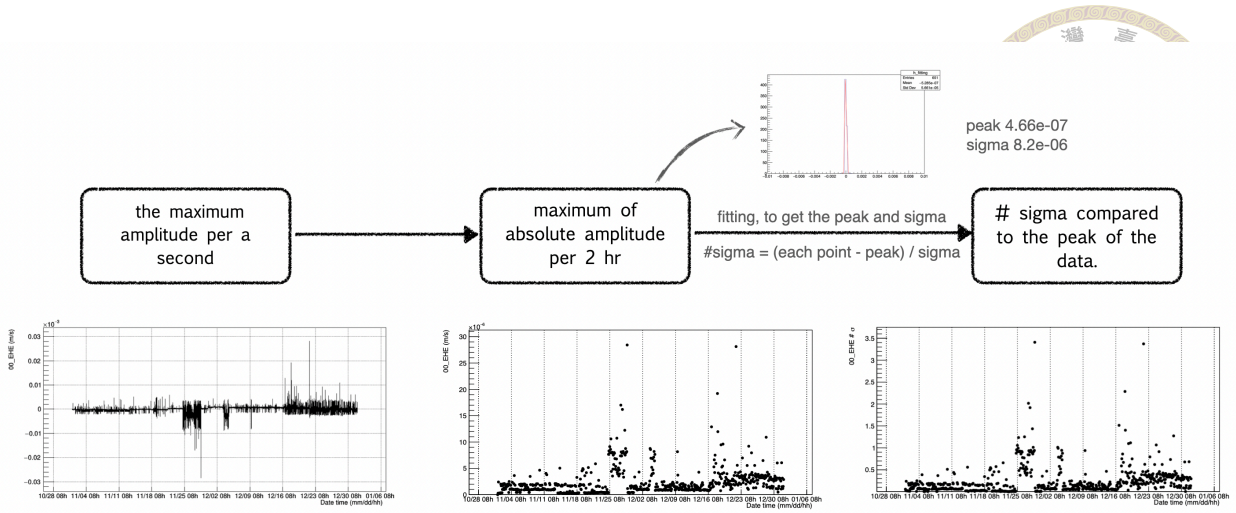

Figure 9.13: Illustration of procedure of waveform data binning by using waveform data from the short period sensor in east-west from November to December 2021.

short period sensor) which is very close to the spike of the radon fluctuation, but it appeared before the radon fluctuation which deviates from the original expectation. Furthermore, the larger ground motion in other directions does not correspond to significant radon fluctuation. Thus, the causal relationship is ambiguous.

For the broadband sensors, no manifest correlation between waveform data from the broadband sensors and anomalous radon events. The possible reason is that they are able to record remote earthquakes, that is, the larger ground motion is not necessarily happened nearby the Hualien weather station. Therefore, it is possible the anomalous radon fluctuation near the Hualien weather station could not relate to the remote earthquakes.

9.6 Conclusion

People have desired to predict disastrous earthquakes for a long time. One well-unknown theory that needs to be verified is that anomalous radon emissions from the crust happen prior to large earthquakes. Based on this idea, a crystal detector to collect the γ-ray emitted from radon was deployed in the Hualien weather station, where its location earthquakes happen frequently.

This chapter describes the data-driven method to identify anomalous radon emissions and the method to calibrate the energy fluctuation. However, the calibration faces a challenging problem, that is, a non-linear decreasing trend of the energy spectrum. It is speculated that such low data quality relates to the fluctuation of the temperature, so a sophisticated calibration and an understanding of the performance of the detector needed to be done in future studies.

doi:10.6342/NTU202300054

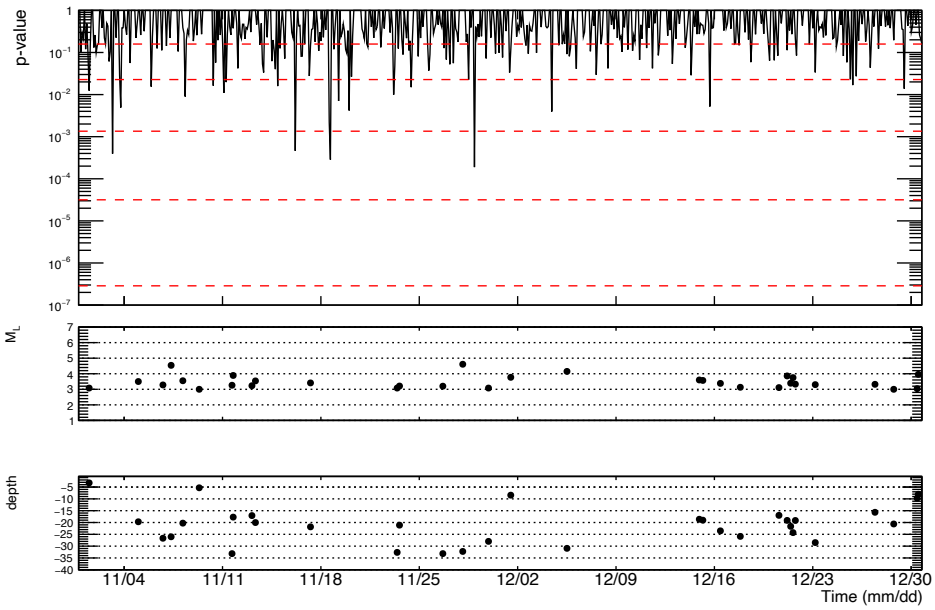

Figure 9.14: Preliminary result of correlation between anomalous radon events and earthquake event within 35 km from Hualien weather station from November to December 2021.

The seismic data, including the earthquake event catalog and waveform data from seismometers, were collected from GDMS in this analysis. A simple method is employed to match the bin of radon data and seismic data, such that the relationship between anomalous radon events and ground motion can be studied.

Although both radon data and seismic data have DAQ-related problems, the preliminary results of the correlation study for a certain period (November to December 2021) are given in section 9.5. No determining evidence for the correlation between anomalous radon events and ground motions for this period. Nevertheless, we have more data that can be studied as long as the calibration is dealt with properly. The improvement of the calibration for both data will benefit future researchers to explore the relationship between anomalous radon emissions and ground motion.ion for both data will benefit the future researchers to explore the relationship of anomalous radon emissions and ground motion.

doi:10.6342/NTU202300054

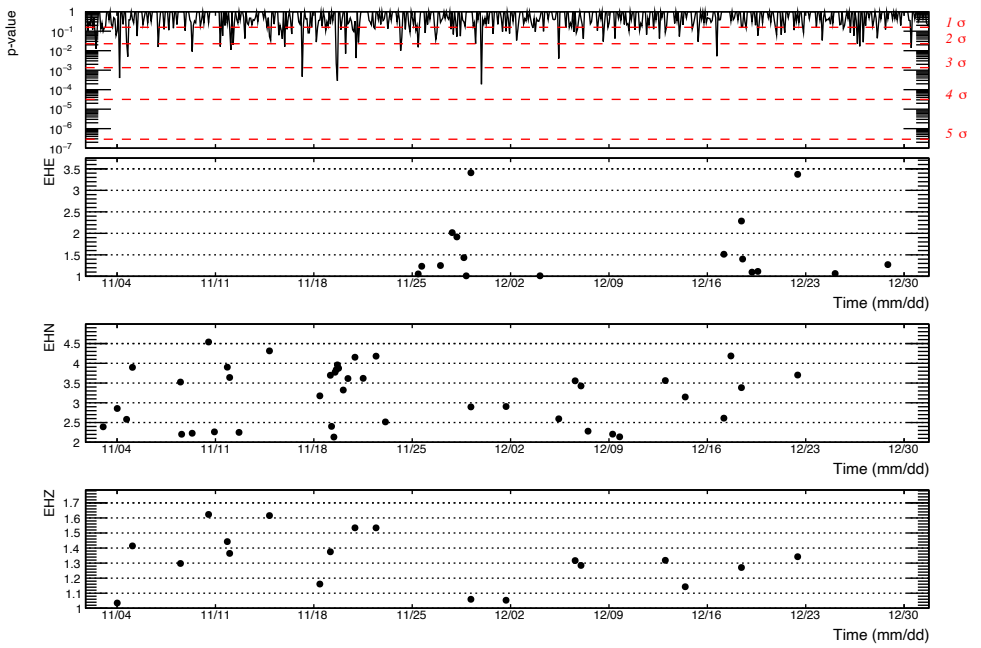

Figure 9.15: Preliminary result of relationship between p-value and waveform data from short period sensor in Haulien weather station.

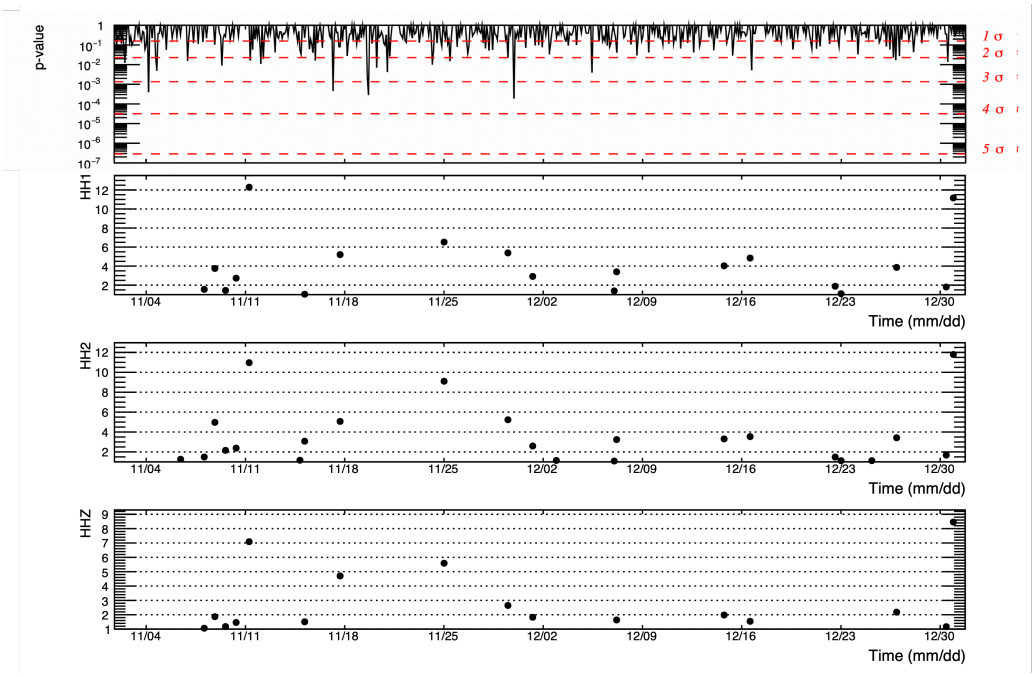

Figure 9.16: Preliminary result of relationship between p-value and waveform data from broadband sensor in Haulien weather station.

doi:10.6342/NTU202300054

References

[1] Gabriel David Palacino Caviedes. Search for magnetic monopoles in 8 TeV centre-of-mass energy proton-proton collisions with the ATLAS detector at the LHC. PhD thesis, York U., Canada, York U., Canada, 12 2015.

[2] You-ying Li. Measurements of the associated VH production cross section in the $H \to \gamma\gamma$ channel at $\sqrt{s} = 13$ TeV in the CMS experiment, 2021.

[3] L. Viliani. Cms tracker performance and readiness for lhc run ii. Nuclear Instruments and Methods in Physics Research Section A: Accelerators, Spectrometers, Detectors and Associated Equipment, 824:67–69, 7 2016.

[4] CMS Collaboration. The CMS ECAL performance with examples. JINST, 9:C02008, 2014.

[5] CMS Collaboration. Calibration of the CMS hadron calorimeters using proton-proton collision data at $\sqrt{s} = 13$ TeV. JINST, 15(05):P05002, 2020.

[6] Mai Muhammed Hassan El Sawy. Search for Magnetic Monopoles in the CMS experiment at the Large Hadron Collider (LHC)., 2020.

[7] Emilio Meschi, T. Monteiro, Christopher Seez, and Pratibha Vikas. Electron Reconstruction in the CMS Electromagnetic Calorimeter. 6 2001.

[8] ATLAS Collaboration. Search for magnetic monopoles and stable high-electric-charge objects in 13 tev proton-proton collisions with the atlas detector. Physical Review Letters, 124, 2020.

[9] 吳致平. 氡氣即時偵測器的發展與在臺灣地震站的部署. Master's thesis, Jan 2021.

[10] Central Weather Bureau (CWB, Taiwan). Central weather bureau seismographic network, 2012.

[11] Jorg Wenninger. Operation and Configuration of the LHC in Run 2. Mar 2019.

doi:10.6342/NTU202300054

[12] Mark Thomson. Modern particle physics. Modern Particle Physics, 9 2013.

[13] P. A.M. Dirac. Quantised singularities in the electromagnetic field,. Proceedings of the Royal Society of London. Series A, Containing Papers of a Mathematical and Physical Character, 133:60–72, 9 1931.

[14] P. A.M. Dirac. The theory of magnetic poles. Physical Review, 74:817, 10 1948.

[15] J. J. Sakurai and Jim Napolitano. Modern quantum mechanics. Modern Quantum Mechanics, 9 2017.

[16] John Preskilf. Magnetic monopoles. 34:461–530, 11 2003.

[17] Y. M. Cho, Kyoungtae Kimm, and J. H. Yoon. Mass of the electroweak monopole. Modern Physics Letters A, 31, 12 2012.

[18] A. De Roeck, A. Katre, P. Mermod, D. Milstead, and T. Sloan. Sensitivity of LHC experiments to exotic highly ionising particles. The European Physical Journal C, 72(4), apr 2012.

[19] Lyndon Evans and Philip Bryant. LHC Machine. JINST, 3:S08001, 2008.

[20] CMS Collaboration. The CMS Experiment at the CERN LHC. JINST, 3:S08004, 2008.

[21] CMS Collaboration. The CMS trigger system. JINST, 12(01):P01020, 2017.

[22] Johan Alwall, Michel Herquet, Fabio Maltoni, Olivier Mattelaer, and Tim Stelzer. Madgraph 5 : Going beyond. Journal of High Energy Physics, 2011, 6 2011.

[23] Torbjörn Sjöstrand, Stefan Ask, Jesper R. Christiansen, Richard Corke, Nishita Desai, Philip Ilten, Stephen Mrenna, Stefan Prestel, Christine O. Rasmussen, and Peter Z. Skands. An introduction to pythia 8.2. Computer Physics Communications, 191:159–177, 10 2014.

[24] Teresa Lenz. Searches for long-lived heavy particles, HSCP, monopoles (ATLAS+CMS). Searches for long-lived heavy particles, HSCP, monopoles (ATLAS+CMS). Technical report, CERN, Geneva, Jul 2016. 10 pages, 11 figures, published in the proceedings of the 4th Conference on Large Hadron Collider Physics 2016 (LHCP 2016), Lund, Sweden; PoS(LHCP2016)104.

[25] S. Baines, N. E. Mavromatos, V. A. Mitsou, J. L. Pinfold, and A. Santra. Monopole production via photon fusion and drell-yan processes: Madgraph implementation and perturbativity via velocity-dependent coupling and magnetic moment as novel features. 8 2018.

doi:10.6342/NTU202300054

[26] D. A. Petyt. Mitigation of anomalous apd signals in the cms electromagnetic calorimeter. volume 404. Institute of Physics Publishing, 2012.

[27] CMS Collaboration. Cms tracking performance results from early lhc operation. European Physical Journal C, 70:1165–1192, 7 2010.

[28] Pekka K Sinervo. Definition and treatment of systematic uncertainties in high energy physics and astrophysics. 2004.

[29] CMS Collaboration. Silicon Strip Tracker Performance results 2018. Sep 2018.

[30] CMS Collaboration. CMS Luminosity Measurements for the 2016 Data Taking Period. Technical report, CERN, Geneva, 2017.

[31] CMS Collaboration. CMS luminosity measurement for the 2018 data-taking period at $\sqrt{s}$ = 13 TeV. Technical report, CERN, Geneva, 2019.

[32] CMS Collaboration. Particle-flow reconstruction and global event description with the cms detector. 6 2017.

[33] CMS Collaboration. Performance of missing transverse momentum reconstruction at the CMS detector in 13 TeV data. Technical report, CERN, Geneva, 2019.

[34] V. Chisté, M. M. Bé, and C. Dulieu. Evaluation of decay data of radium-226 and its daughters. 2007.

[35] M. A. Vasiliev, P. Blum, G. Chubarian, R. Olsen, C. Bennight, T. Cobine, D. Fackler, M. Hastedt, D. Houpt, Z. Mateo, and Y. B. Vasilieva. A new natural gamma radiation measurement system for marine sediment and rock analysis. Journal of Applied Geophysics, 75:455–463, 11 2011.

[36] Robert MacCoun and Saul Perlmutter. Blind analysis: Hide results to seek the truth. Nature 2015 526:7572, 526:187–189, 10 2015.

[37] Weatherspark.

[38] Tim Ahern and Bernard Dost. Seed reference manual standard for the exchange of earthquake data seed format version 2.4. 2012.

[39] Moritz Beyreuther, Robert Barsch, Lion Krischer, Tobias Megies, Yannik Behr, and Joachim Wassermann. Obspy: A python toolbox for seismology. Seismological Research Letters, 81:530–533, 5 2010.

doi:10.6342/NTU202300054

doi:10.6342/NTU202300054

Appendix A — Event selection tables and graphs

doi:10.6342/NTU202300054

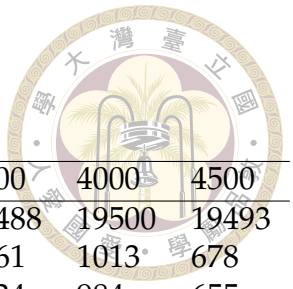

Mass point (GeV)	1000	1500	2000	2500	3000	3500	4000	4500
generated event	16000	16000	17500	18884	19000	19488	19500	19493
trigger	801	921	1010	1186	1200	1261	1013	678
preselections	784	901	984	1159	1167	1234	984	655
energy (E_{5x5})	688	815	892	1016	1011	1065	864	580
f_{51}	375	447	529	571	509	549	470	354
$dE/dx_{significance}$	372	446	526	561	495	532	450	327
signal efficiency (ϵ_{sig})	2.33%	2.79%	3.01%	2.97%	2.61%	2.73%	2.31%	1.68%

Table A.2: The cut-flow table for 2017 MC simulation for each mass points.

Mass point (GeV)	1000	1500	2000	2500	3000	3500	4000	4500
generated event	19500	19500	19500	19066	19500	19476	19500	19500
trigger	1061	1265	1286	1273	1327	1263	1065	716
preselections	1013	1226	1241	1221	1278	1213	1017	676
energy (E_{5x5})	902	1121	1137	1091	1122	1035	940	623
f_{51}	487	613	655	622	628	551	528	386
$dE/dx_{significance}$	485	610	649	616	615	536	514	367
signal efficiency (ϵ_{sig})	2.49%	3.13%	3.33%	3.23%	3.15%	2.75%	2.64%	1.88%

Table A.3: The cut-flow table for 2016 MC simulation for each mass points.

Mass point (GeV)	1000	1500	2000	2500	3000	3500	4000	4500
generated event	19500	18995	19500	19454	19500	19500	19500	19500
trigger	1060	1190	1275	1326	1344	1311	1070	665
preselections	1018	1149	1236	1280	1298	1264	1010	631
energy (E_{5x5})	903	1069	1123	1163	1139	1096	926	578
f_{51}	467	612	633	627	629	614	494	367
$dE/dx_{significance}$	462	609	624	607	600	578	468	329
signal efficiency (ϵ_{sig})	2.37%	3.21%	3.20%	3.12%	3.08%	2.96%	2.40%	1.69%

Table A.4: The cut-flow table for 2016APV MC simulation for each mass points.

doi:10.6342/NTU202300054

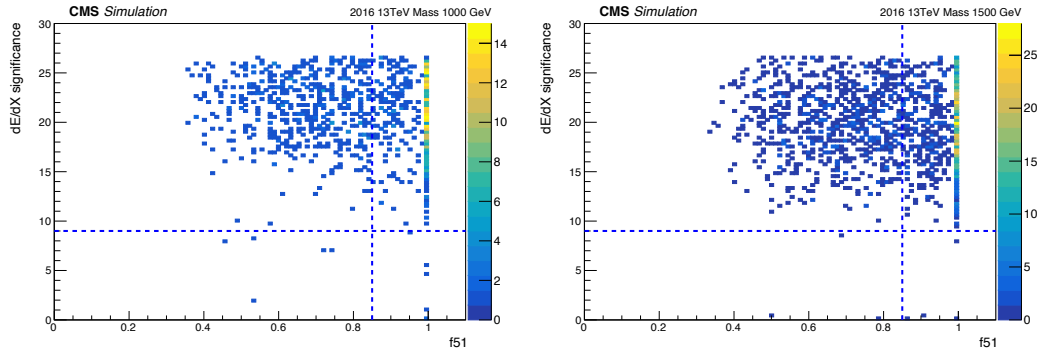

(a) 1000 GeV

(b) 1500 GeV

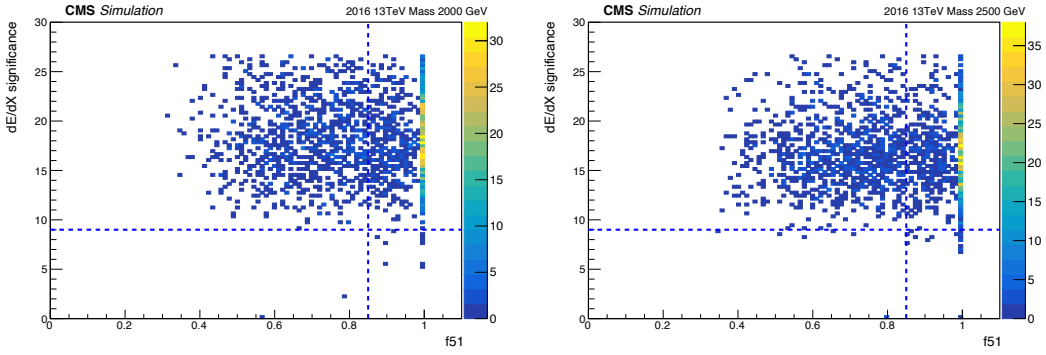

(c) 2000 GeV

(d) 2500 GeV

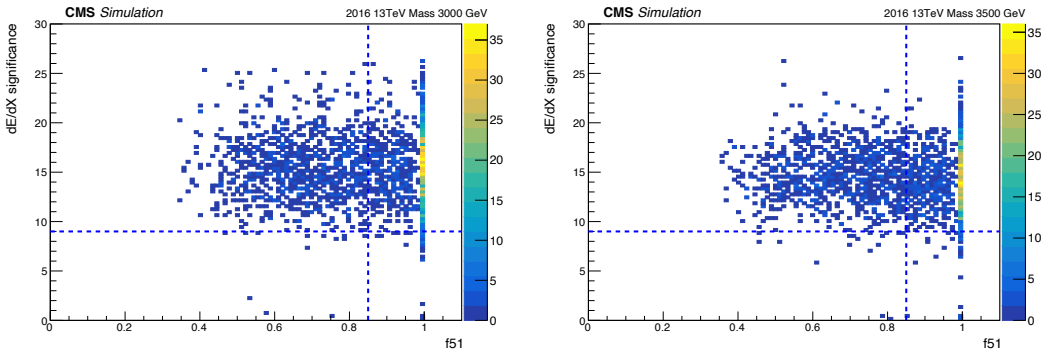

(e) 3000 GeV

(f) 3500 GeV

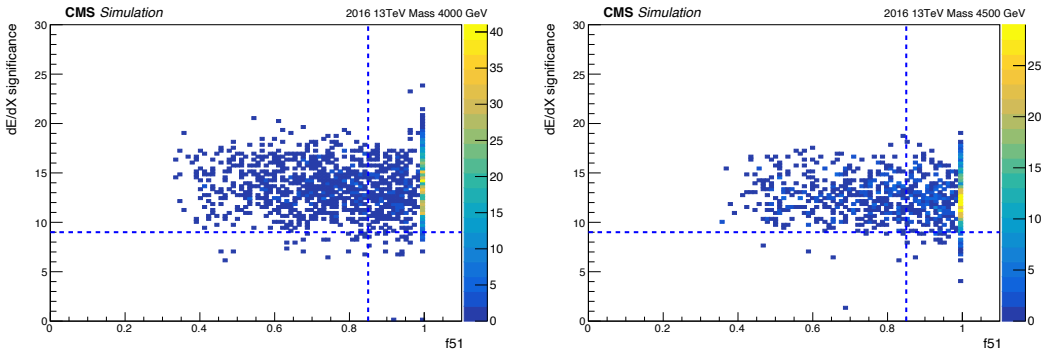

(g) 4000 GeV

(h) 4500 GeV

Figure A.17: The joint distribution of dE/dx_{sig} and f_{51} for each mass point after HLT and energy > $175GeV$ cut for 2016 MC. The events are filled once lest the repeat count. The signal region ($dE/dx_{sig} > 9$ and $f_{51} > 0.85$) is distinct from the deep blue dotted lines.

doi:10.6342/NTU202300054

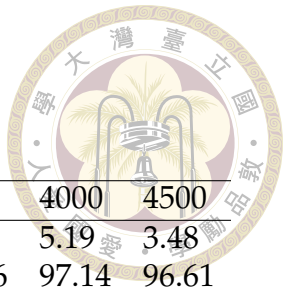

Mass point (GeV)	1000	1500	2000	2500	3000	3500	4000	4500
trigger	5.01	5.76	5.77	6.28	6.32	6.47	5.19	3.48
preselections	97.88	97.83	97.43	97.72	97.25	97.86	97.14	96.61
energy (E_{5x5})	87.76	90.46	90.65	87.66	86.63	86.30	87.80	88.55
f_{51}	54.51	54.85	59.30	56.20	50.35	51.55	54.40	61.03
$dE/dx_{significance}$	99.20	99.78	99.43	98.25	97.25	96.90	95.74	92.37

Table A.5: The relative efficiency(%) table for 2017 MC simulation for each mass points.

Mass point (GeV)	1000	1500	2000	2500	3000	3500	4000	4500
trigger	5.44	6.49	6.59	6.68	6.81	6.48	5.46	3.67
preselections	95.48	96.92	96.50	95.92	96.31	96.04	95.49	94.41
energy (E_{5x5})	89.04	91.44	91.62	89.35	87.79	85.33	92.43	92.16
f_{51}	53.99	54.68	57.61	57.01	55.97	53.24	56.17	61.96
$dE/dx_{significance}$	99.59	99.51	99.08	99.04	97.93	97.28	97.35	95.08

Table A.6: The relative efficiency(%) table for 2016 MC simulation for each mass points.

Mass point (GeV)	1000	1500	2000	2500	3000	3500	4000	4500
trigger	5.44	6.26	6.54	6.82	6.89	6.72	5.49	3.41
preselections	96.04	96.55	96.94	96.53	96.58	96.41	94.39	94.89
energy (E_{5x5})	88.70	93.04	90.86	90.86	87.75	86.71	91.68	91.60
f_{51}	51.72	57.25	56.37	53.91	55.22	56.02	53.35	63.49
$dE/dx_{significance}$	98.93	99.51	98.58	96.81	95.39	94.14	94.74	89.65

Table A.7: The relative efficiency(%) table for 2016APV MC simulation for each mass points.

doi:10.6342/NTU202300054

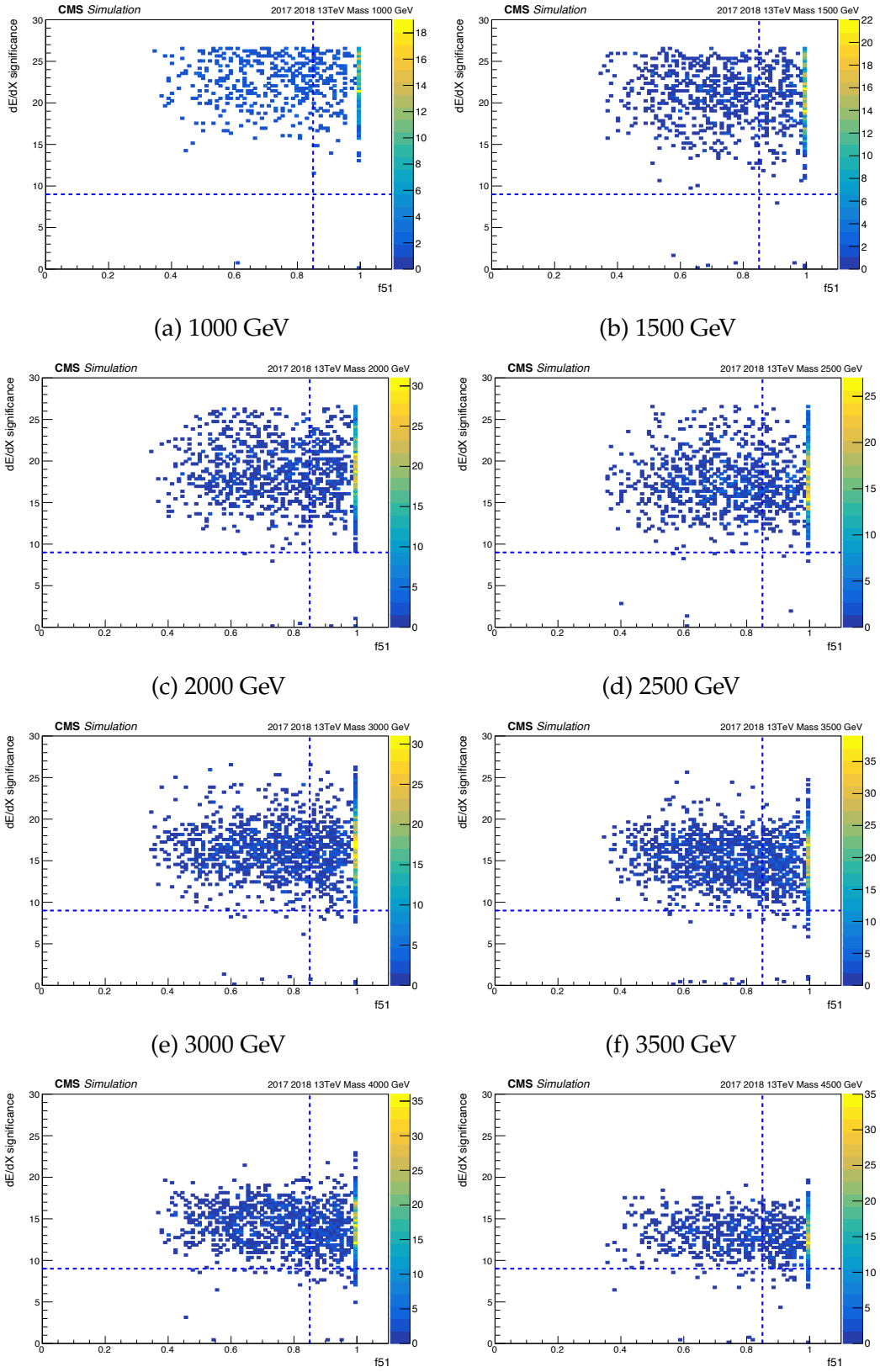

(a) 1000 GeV

(b) 1500 GeV

(c) 2000 GeV

(d) 2500 GeV

(e) 3000 GeV

(f) 3500 GeV

(g) 4000 GeV

(h) 4500 GeV

Figure A.18: The joint distribution of dE/dx_{sig} and f_{51} for each mass point after HLT and energy > $200GeV$ cut for 2017MC and 2018 MC. The events are filled once lest the repeat count. The signal region ($dE/dx_{sig} > 9$ and $f_{51} > 0.85$) is distincted by the deep blue dotted lines.

doi:10.6342/NTU202300054

doi:10.6342/NTU202300054

Appendix B — Seismograph waveform data

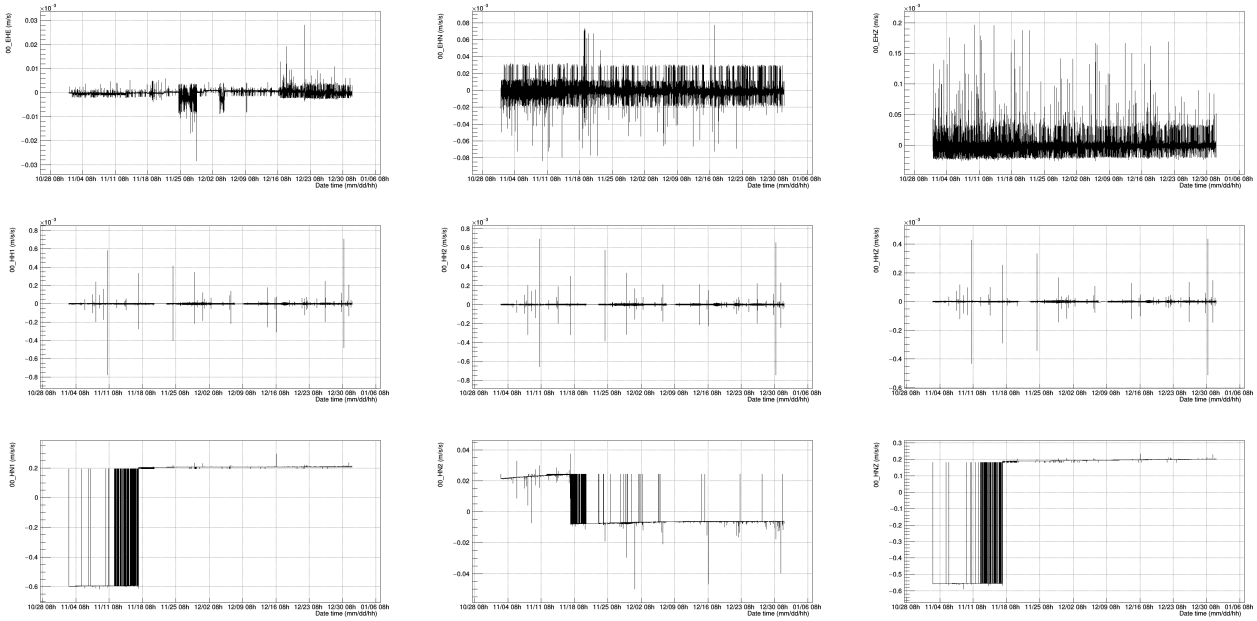

Figure B.19: Demo of waveform data from the short period sensor (EH*), broadband sensor (HH*), and accelerometer (HN*) from November 1st to December 31th in 2022. Note that only the largest amplitude in each 1 second is plotted. No significant earthquake (with $M_L >$ 5 and depth < 35 km) happened in this period. Moreover, raw data from accelerometer have serious deficiency, which need to discuss with the GDMS.

doi:10.6342/NTU202300054